Disentangling the Formation of PAHs in Extreme Environments by IR/UV Double Resonance Spectroscopy

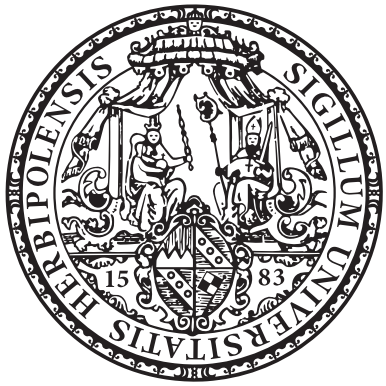

Dissertation zur Erlangung des naturwissenschaftlichen Doktorgrades

an der Fakultät für Chemie und Pharmazie

der Julius-Maximilians-Universität Würzburg

vorgelegt von

Tobias Preitschopf

aus Wolfratshausen

Würzburg, April 2023

Eingereicht bei der Fakultät für Chemie und Pharmazie am ..... .

Gutachter der schriftlichen Arbeit:

1. Gutachter: .....

2. Gutachter: .....

Prüfer des öffentlichen Promotionskolloquiums:

1. Prüfer: .....

2. Prüfer: .....

3. Prüfer: .....

Datum des öffentlichen Promotionskolloquiums: .....

Doktorurkunde ausgehändigt am: .....

TABLE OF CONTENTS

LIST OF PUBLICATIONS

This thesis is based on the following previously published articles. My co-authors/ publishers gave me permission to use the works listed below. A detailed explanation about the authors' contribution to the papers is given in *Erklärungen zu Autorenschaften* at the end of this thesis.

- ✦ T. Preitschopf, F. Sturm, I. Stroganova, A. K. Lemmens, A. M. Rijs, I. Fischer, *Chem. Eur. J.* **2023**, *29*, e202202943.
- ✦ X. Miao, T. Preitschopf, F. Sturm, I. Fischer, A. K. Lemmens, M. Limbacher, R. Mitric, *J. Phys. Chem. Lett.* **2022**, *13*, 8939-8944.
- ✦ T. Preitschopf, F. Hirsch, A. K. Lemmens, A. M. Rijs, I. Fischer, *Phys. Chem. Chem. Phys.* **2022**, *24*, 7682–7690.

Furthermore, I participated in the following publications that are not discussed in this thesis:

- ✧ M. Gerlach, B. P. Stoy, T. Preitschopf, E. Karaev, D. Mayer, H. M. Quitián-Lara, P. Hemberger, J. D. Bozek, G. Worth, I. Fischer, *J. Chem. Phys.* **2023**, *158*, 134303.
- ✧ J. Ramler, A. Stoy, T. Preitschopf, J. Kettner, I. Fischer, B. Roling, F. Fantuzzi, C. Lichtenberg, *Chem. Commun.* **2022**, *58*, 9826-9829.
- ✧ M. Gerlach, T. Preitschopf, E. Karaev, H. M. Quitián-Lara, D. Mayer, J. Bozek, I. Fischer, R. F. Fink, *Phys. Chem. Chem. Phys.* **2022**, *24*, 15217-15229.
- ✧ D. Schleier, E. Reusch, M. Gerlach, T. Preitschopf, D. P. Mukhopadhyay, N. Faßheber, G. Friedrichs, P. Hemberger, I. Fischer, *Phys. Chem. Chem. Phys.* **2021**, *23*, 1539-1549.

- ✧ D. P. Mukhopadhyay, D. Schleier, S. Wirsing, J. Ramler, D. Kaiser, E. Reusch, P. Hemberger, T. Preitschopf, I. Krummenacher, B. Engels, I. Fischer, C. Lichtenberg, *Chem. Sci.* **2020**, *11*, 7562-7568.

ABBREVIATIONS

1-MA	1-methylallyl radical
2-MA	2-methylallyl radical, C_4H_7
2-PA	2-phenylallyl radical, C_9H_9
AGB	asymptotic giant branch
amu	atomic mass unit
DFG	difference frequency generation
DFT	density functional theory
DOS	density of states
DPI	dissociative photoionization
EI	electron ionization
FC	Frank-Condon
FEL	free electron laser
FELIX	Free Electron Laser for Infrared eXperiments
FIR	far-infrared
FT-IR	Fourier-transform infrared
FWHM	full width at half maximum
HACA	hydrogen abstraction - acetylene addition
HAVA	hydrogen abstraction - vinylacetylene addition
HST	Hubble Space Telescope
IE	ionization energy
IR	infrared

IR-MPD	IR multiphoton dissociation
IR-MPE	IR multiphoton excitation
IR/UV-IDS	IR/UV ion dip spectroscopy
IRIG	infrared ion gain
ISM	interstellar medium
IVR	intramoleculer vibrational energy redistribution
JWST	James Webb Space Telescope
KDP	potassium dideuterium phosphate
KTA	potassium titanyl arsenate
KTP	potassium titanyl phosphate
LIF	laser-induced fluorescence
LINAC	linear accelerators
MACA	methylidyne addition - cyclization/aromatization
MALDI	matrix-assisted laser desorption ionization
MCP	microchannel plates
MD	molecular dynamics simulations
MIR	mid-infrared
MPI	multiphoton ionization
MS	mass spectrum
Nd:YAG	neodymium-doped yttrium aluminum garnet
NIR	near-infrared
NRMPI	nonresonant multiphoton ionization
OPA	optical parametric amplifier
OPO	optical parametric oscillator
PAC	phenyl addition - (dehydro-)cyclization
PAH	polycyclic aromatic hydrocarbon
PANH	nitrogenated polycyclic aromatic hydrocarbon
PCCP	Physical Chemistry Chemical Physics
PEPICO	photoelectron photoion coincidence

PES	potential energy surface
PI	photoionization
PIE	photoionization efficiency curve
PIMS	photoionization mass spectrometry
PPR	phenylpropargyl radicals
R2PI	resonant two-photon ionization
REMPI	resonance-enhanced multiphoton ionization
RMSD	root-mean-square deviation
RSR	resonance-stabilized radicals
SiC	silicon carbide
SLS	Swiss Light Source
SPI	single-photon ionization
TOF	time-of-flight
TPE	threshold photoelectron
TPES	threshold photoelectron spectroscopy
UIB	Unidentified Infrared Bands
UV	ultraviolet
VIS	visible
VUV	vacuum ultraviolet

CHAPTER 1

INTRODUCTION

1.1 The Next Generation Space Telescope

Hardly a week passes without new images recorded by NASA's James Webb Space Telescope (JWST)[1] that recently was launched on Dec. 25, 2021, in French Guiana, South America. Only days after coming online in late June 2022, the $10 billion heavy telescope produced the deepest and sharpest image of the distant universe to date within 12.5 hours (Figure 1.1).[2] Since then several ground-breaking discoveries have already been made, among them the detection of carbon dioxide (a building-block of life) in the atmosphere of an exoplanet,[3] or the exploration of very compact structures of star clusters inside galaxies, which offers a window into the early stages of star formation.[4] Within the next ten (planned) to twenty years (expected), the research conducted with the largest telescope in space (collecting area of 25 m^2, effective focal length of 131.4 m)[1] will help to realize fundamental breakthroughs in four key categories: the identification of the first luminous sources forming in the early universe; the evolution of galaxies and fainted structures over billions of years; the birth and evolution of stars and planetary systems; and the determination of the physical and chemical properties of planetary systems and the origins of life.[1]

Webb - an infrared telescope

As the formal successor of the Hubble Space Telescope (HST)[6] that was optimized for shorter ultraviolet (UV) and primarily visible (VIS) wavelengths of light, the JWST observes the universe at wavelengths longer than visible light - the infrared (IR) region. Observations in this wavelength region constitute a key technique to accomplish the four aforementioned science goals, because the formation of stars

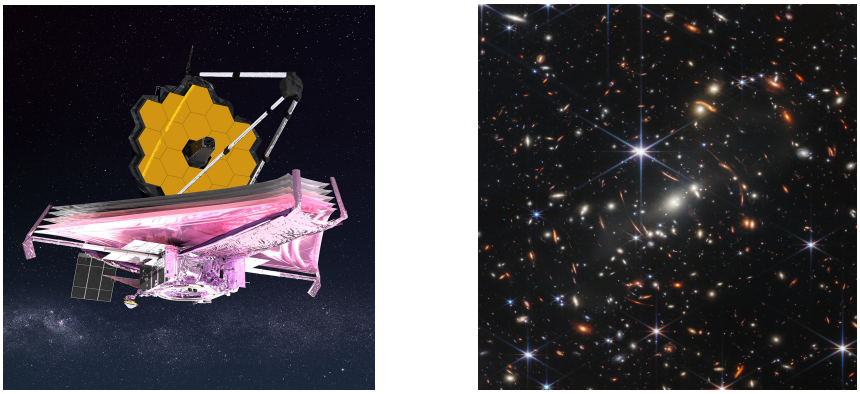

Figure 1.1. Left: Illustration of the James Webb Space Telescope (JWST). Right: Webb's First Deep Field image. Taken with permission from the NASA Image Gallery.[5]

and planets takes place in the centres of dense clouds of gas and dust which effectively scatter or absorb visible light and thus cannot be observed, for example, by the HST. In contrast, near-infrared (NIR) light is able to pass through cosmic dust more freely.[7] Furthermore, to observe sources such as the first galaxies and protostars in the early universe, the JWST has to look into the far distance. Light that is emitted in the UV or visible region billions of light-years away is stretched into longer wavelengths (called red-shifting) into the NIR and mid-infrared (MIR) region as it travels through the expanding universe.[8] In addition, the vast majority of the phenomena astronomers want to observe are far too cold to radiate at shorter wavelengths according to Planck's law: A black body, an object that absorbs all incident electromagnetic radiation, emits radiation depending on its temperature, whereby a cold body emits longer wavelengths than a hotter one.[9] Most of the cold objects such as clouds, planets or comets, with temperatures less than several thousand degrees, emit primarily in the IR wavelength region and thus are best observed using infrared telescopes.[10]

To this day seven space telescopes whose main mission was (or still is) detecting IR light have been operated before the JWST, starting with IRAS in 1983 and more recently the Spitzer and WISE space missions.[11] The JWST is by far the most advanced telescope to ever conduct infrared research in space, which is why it was initially called the *Next Generation Space Telescope* before renamed after NASA's second administrator in 2002.[12] It is equipped with four IR instruments (a NIR camera, NIR spectograph, MIR instrument, and a NIR tunable filter imager) covering a broad wavelength range of 0.6 to 28.5 μm at unprecedented sensitivity and spectral resolution.[12] Developed and headed by NASA with major contributions from the European and Canadian Space Agencies (ESA and CSA), the JWST will provide countless of images and spectroscopic data that have never been recorded by any other telescope.

1.2 The PAH Hypothesis

Due to significant improvements in the technology of IR detectors, infrared astronomy started to blossom in the 1960s and has substantially improved our understanding of the interstellar medium (ISM) ever since.[13] Shortly after the first spectroscopic explorations of the infrared radiation of the universe in the early 70s, Gillet *et al.* observed broad but resolved emission features at 8.6 and 11.2 μm (1163 and 893 cm^{-1}).[14] Carbonate grains were among the first proposed carriers of these emissions due to a good agreement with the profile and peak position of the 11.2 μm feature. However, this assignment was quickly discarded

as air-borne observatories did not detect their strong emission band at 6.85 μm (1460 cm^{-1}).[15] Instead, new broad and intense features were observed at 3.3, 6.2, and 7.7 μm (3030, 1613, and 1299 cm^{-1}) that appeared as a strong set together with the previously detected two emission bands, see Figure 1.2.[16] Interestingly, these bands were detected in a wide variety of astrophysical environments, such as planetary nebulae, HII regions, reflection nebulae, or extragalactic sources.[17] For almost a decade, the source of these bands remained unclear giving them their widely known name as the Unidentified Infrared Bands (UIB).[13] It was not before the early 80s, when Duley and Williams showed that the 3.3 μm emission feature can be assigned to aromatic CH stretching vibrations.[18] This resulted in several proposed aromatic carriers such as amorphous carbon,[19] quenched carbonaceous composites,[20] polycyclic aromatic hydrocarbons (PAHs),[21,22] or nanodiamonds.[23] However, the unidentified emission bands have been found to be associated with a number of stellar objects in which most of the proposed dust grains exhibit a radiative equilibrium temperature (∼10−75 K)[13] much too low to lead to thermal emission in the MIR region.[25] Shortly after, Sellgren explained the thermal emission due to very small grains with low heat capacities that temporarily reach high temperatures after absorption of UV photons from nearby stars.[25] This key step allowed Leger and Puget[22] as well as Allamandola *et al.*[21]

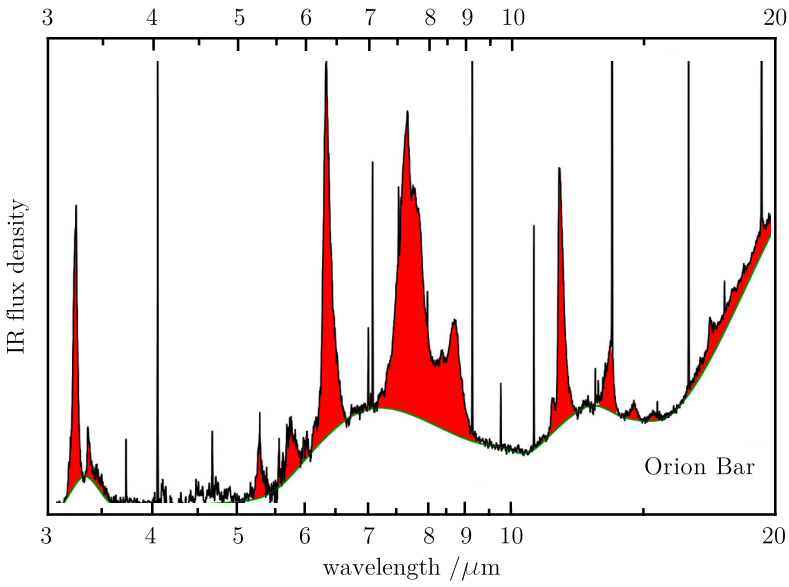

Figure 1.2. The MIR spectra of the Photodissociation Region in the Orion Bar show distinctive emission features called the UIB. Adapted with permission from Ref. [24].

to independently propose molecule-sized PAHs and PAH-like species as carriers of the UIB, which is considered as the birth of the so called *PAH Hypothesis*.[17]

PAHs as carriers of the UIB

PAHs are organic compounds that purely contain carbon and hydrogen atoms and are composed of several and often fused aromatic rings.[26] Upon absorption of a single UV photon, they are brought into an electronically excited state. Subsequently, the photon energy is converted into molecular vibrational energy *via* internal conversion and intersystem crossing processes, which primarily is lost by emission of IR photons on the timescale of seconds as collisional deexcitation is rare due to the low density in the ISM.[27] The corresponding IR emissions are then detected by IR telescopes, whereby the main features of the UIB have been assigned to CH stretching modes (3.3 μm), CC stretching vibrations (6.2 μm), coupled CH in-plane bending and CC stretching modes (7.7 μm), as well as CH out-of-plane bending vibrations (11.2 μm).[17] These emission features have been found to make up to 10−20 % of the total detected IR power in the MIR region,[28] showing that PAHs are among the most abundant complex organic molecules in space and contain a large fraction of the total cosmic carbon (10−15 %).[13]

Due to various structural similarities, spectral features of different PAHs commonly coincide, which hampers their unambiguous identification.[13] Differences in the detected IR spectra are small but apparent in the relative intensities and positions as well as the shapes of the IR bands.[29] Laboratory as well as quantum-chemical studies of PAHs have shown that various parameters such as size,[30] molecular (edge) structure,[31] temperature,[17] and charge,[32] significantly influence their spectral infrared pattern. The consequences of these alterations are still not fully understood leading to several proposed PAH-related species to contribute to similar specific spectral patterns.[17] Among the most promising candidates are PAHs with side groups (such as alkylated molecules or hetero-derivatives),[33] heterosubstituted PAHs (particularly N substituted PAHs called nitrogenated polycyclic aromatic hydrocarbons (PANHs)),[34] PAH clusters such as dimers and trimers,[35] as well as PAH ions.[17,32]

For example, the CC stretching vibrations of pure PAHs are observed near 6.3 μm and thus cannot account for the dominant astronomical band at 6.2 μm.[46] Instead, the introduction of nitrogen within a PAH results in a red-shift of the CC stretching mode, suggesting that this band could be directly linked to PANHs. Indeed, experimental results verified that protonated PANHs might contribute to the 6.2 μm feature of the UIB,[47] indicating that nitrogenated PAHs might

play an important role in various interstellar environments.[46] These compounds could be formed in planetary atmospheres such as of Saturn's largest moon, Titan, which mainly consists of nitrogen (≈98 %).[48,49] The shape of the 11.2 μm band is another good indicator for the presence of further PAH-related species, as it commonly exhibits an asymmetric tailing towards lower energies along with a peak position that can shift up to 11.25 μm.[50] The emission of relatively large PAH clusters could account for the observed red-shaded profile of the band due to CH out-of-plane bending modes that are red-shifted in comparison with highly diluted PAH monomers.[51] These species are potentially only formed in denser environments of molecular clouds that further act as a UV shield, which hampers an efficient decomposition of PAH clusters upon absorption of an UV photon.[50]

The local physical and chemical environment highly determines the habitat in which certain PAH-related species are present. Consequently, these compounds can act as a diagnostic tool to derive valuable information on their surrounding environment.[17] *E.g.*, PAH-related species can be used as tracers for the formation of stars and planets as they absorb most of the UV light emitted by young stars leading to very bright IR emission bands.[52] With its unprecedented spectral and spatial resolution, the JWST will help to unravel several PAH-related carriers of the UIB over the next decade, which will allow to gain a deeper understanding not only of their formation but also the formation of stars and planets as well. A se-

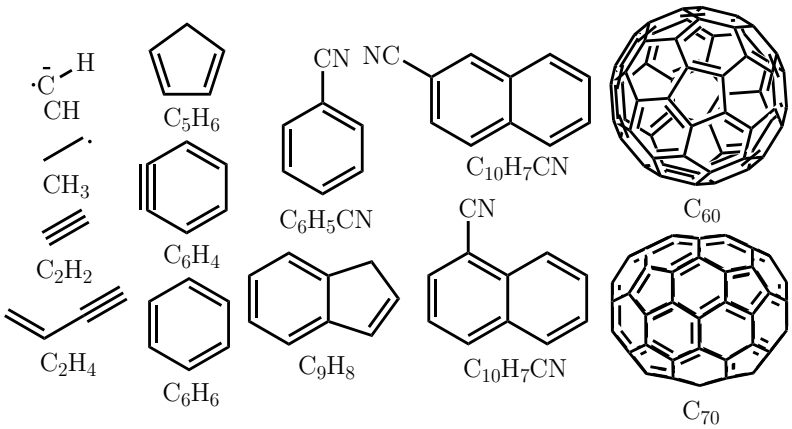

Figure 1.3. Selected hydrocarbons detected in space. Vinylacetylene (C_2H_4),[36] cyclopentadiene (C_5H_6),[37] *o*-benzyne (C_6H_4),[38] and indene (C_9H_8),[39] have been detected using the QUIJOTE[36] line survey. Methylidyne (CH) was among the first two molecules ever detected in space.[40] Methyl (CH_3),[41] acetylene (C_2H_4),[42] benzene (C_6H_6),[43] as well as the largest molecules ever detected in space, C_{60} and C_{70},[44] have been discovered *via* their IR spectra. Furthermore, the cyano-derivatives of the small (polycyclic) aromatics benzene (C_6HCN)[45] and naphthalene ($C_{10}H_7CN$)[33] have been detected just recently.[33,45]

lected set of (aromatic) hydrocarbons that have already been identified in space unambiguously is given in Figure 1.3. Among them are *o*-benzyne (C_6H_4),[38] indene (C_9H_8),[39] and the cyano-derivatives of naphthalene ($C_{10}H_7CN$).[33]

1.3 Formation of PAHs - From the Interstellar Medium to Combustion

Since PAHs have been proposed as the carriers of the UIB, astrophysicists and astrochemists have aimed for a fundamental understanding of their formation mechanisms as the missing link between small carbon molecules, fullerenes (Figure 1.3), and carbonaceous nanoparticles such as interstellar grains.[53] Inner envelopes of carbon-rich asymptotic giant branch (AGB) stars (low or intermediate mass stars at a late evolutionary phase in their life)[54] and planetary nebulae as their descendants were among the first interstellar objects that have been proposed as key sources for complex organic molecules such as PAHs.[55,56] In these environments temperatures of a few 1000 K are commonly reached,[57] enabling molecular growth *via* mechanisms which are presumably similar to pathways that are observed in combustion processes. Hence, many astrochemical PAH formation routes have been proposed on the basis of combustion models.[53]

In combustion research, PAHs have been identified as key building blocks for soot particles,[58] which originate from natural as well as anthropogenic processes. The understanding of the formation of PAHs and soot has been one of the central research goals in the area of combustion for several decades, mostly driven by health-hazard and pollution concerns due to their carcinogenic potential.[59,60] Generally, PAHs are unwanted byproducts of incomplete combustion processes (*e.g.,* of transportation fuels) and are generated *via* a large array of possible reactions that are difficult to disentangle due to a great diversity of potentially formed (isomeric) molecules.[61] Consequently, many key details of PAH formation still remain unresolved. However, a general scientific consensus has been found about basic mechanisms that are involved in this process. These pathways include sequential reactions of C_2, C_3, or other small (active) reactants, that are generated in comparatively large amounts in the decomposition of fossils fuels.[61] One mechanism that has received much attention over the last decades is the repetitive abstraction of a hydrogen atom followed by an addition of acetylene (C_2H_2), called the hydrogen abstraction - acetylene addition (HACA) mechanism, see Figure 1.4.[62] As HACA has been shown to be too slow to account for the efficient and fast formation of larger PAHs,[63] an alternative competing pathway was suggested called

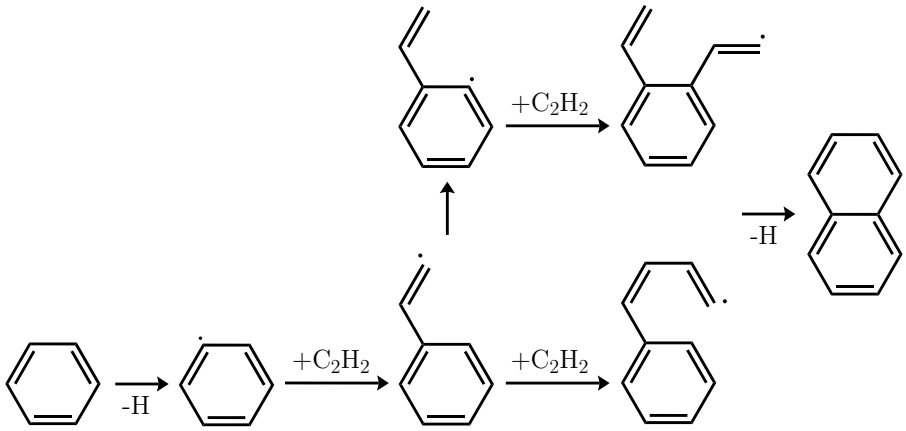

Figure 1.4. Formation of naphthalene *via* HACA.

the phenyl addition - (dehydro-)cyclization (PAC) mechanism.[63] This pathway includes an initial addition of phenyl radicals (C_6H_5) followed by a successive dehydrogenation leading to cyclization and aromatization.[26] Both mechanisms only function at high temperatures as the addition processes are accompanied with barriers between 5 and 30 kJ·mol^{-1}.[26] Furthermore, the vast majority of combustion models involve reactive open-shell species, in particular resonance-stabilized radicals (RSR) such as propargyl (C_3H_3), as key intermediates in the formation of PAHs, because they can accumulate in reacting environments owing to their relatively high stability.[64]

Astrochemical models have included these basic mechanisms to suggest pathways to PAH formation in high temperature carbon-rich circumstellar environments.[65] However, PAHs efficiently decompose in the ISM due to galactic cosmic rays, photolysis, and shock waves,[66,67] resulting in lifetimes of around 10^8 years, which is significantly shorter than the time periods of their formation and injection into the ISM ($\sim 10^9$ years) by carbon-rich envelopes.[68] Consequently, if PAHs were only produced in the proposed hot environments, they should not be present in the ISM at the observed high abundances. This contradiction is considered as a key paradox in astrochemistry,[69] indicating so far unexplained low-temperature routes which might exist in cold environments of the ISM.[53] These pathways might further constitute important mechanisms to PAH formation in hydrocarbon-rich atmospheres of planets and their moons such as Saturn and Titan.[26] Promising low-temperature routes are the so called hydrogen abstraction - vinylacetylene addition (HAVA)[70] and the methylidyne addition - cyclization/aromatization (MACA)[69] mechanisms, that have been shown to barrierlessly form the prototype PAHs indene and naphthalene.[26,69]

Interestingly, little is known so far about the formation of PANHs in the universe, in which a CH unit in a PAH is replaced by an isoelectronic nitrogen atom. The molecular structure of PANHs suggests that they might be important intermediates in the formation of biorelevant molecules such as nucleobases, the central components of DNA and RNA.[71] Traces of extraterrestrial nucleobases (pyrimidines, purines) have been found in carbonaceous chondrites (stony meteorites),[72–74] showing the astrochemical relevance of N-containing aromatic molecules. Although formation routes of the N-substituted analogs are much less understood in comparison with their PAH counterparts, it is reasonable to assume similarities in the various mechanisms considering that nitrogen is isoelectronic with the CH moiety in aromatic molecules.[55] For example, the gas-phase reaction of pyridyl radicals (C_5H_4N) with two acetylene molecules has been shown to form the two prototype PANHs isomers quinoline and isoquinoline (C_9H_7N) at high temperatures in a HACA type mechanism.[75,76] While this route possibly accounts for PANH growth in the inner regions of circumstellar envelopes of carbon rich stars,[77] the formation of pyridine is still unknown. A potential pathway has been proposed *via* the reaction of hydrogen cyanide (HCN) with two acetylene molecules in a computational study,[78] but has not yet been verified experimentally. Another possible pathway to pyridine is the reaction of the cyano vinyl radical (C_2H_2CN) with vinyl cyanide (C_2H_3CN) at high temperatures.[77]

Although the research on fundamental pathways for the formation of (nitrogenated) PAHs is still in its infancy, the astrochemical research community continuously discovers new potential mechanisms that might help to reveal the complex (carbon based) chemistry in the universe. As replicating the extreme environments, such as the hot inner envelopes of AGB stars or the low-temperature conditions found in the ISM, is extremely difficult under laboratory conditions on planet Earth, high-level quantum mechanical calculations as well as advanced experiments are required to gain a better understanding of the chemistry of cosmic PAHs.

1.4 Outline of this Thesis

The main goals of the work in this thesis were built on research-related questions that revolve around the bottom-up formation of PAHs in high-temperature environments as well as noncovalent interactions in PANH clusters in the gas-phase.

Understanding the generation of PAHs in high-temperature processes, *e.g.,* in the inner envelopes of AGB stars[55] or in the combustion of fuels,[61] is challenging due to various potential reactions that might contribute to their formation.[61]

The vast majority of astrochemical as well as combustion models involve sequential reactions of small hydrocarbons such as acetylene or RSR.[53] In the research conducted in this thesis, a *pyrolysis microreactor* was employed to generate these radicals from suitable precursors at a high number density to perform gas-phase experiments.[79] Additionally, the reactor was utilized to initiate bimolecular reactions to promote molecular growth under well-defined conditions.[80,81] Since the generated species need to be studied in isolation due to their high reactivity, the *molecular beam technique* was employed, which allowed to investigate the intrinsic properties of these species spectroscopically in a *time-of-flight (TOF) mass spectrometer*.[82] As basic mass spectrometry generally is not appropriate for a reliable product identification due to potentially formed isomers, *IR/UV ion dip spectroscopy (IR/UV-IDS)* was utilized to combine the mass-selectivity of UV photoionization with the structural sensitivity of IR radiation.[83] This method is based on the change of the vibrational population in the electronic ground state of a molecule by IR absorption, followed by *resonance-enhanced multiphoton ionization (REMPI)*[84] *via* intermediate electronically excited states. Thereby, species-selected IR spectra are obtained which allow to distinguish between different isomers with the aid of *ab initio density functional theory (DFT) calculations*.[85] All experiments were carried out in Nijmegen, The Netherlands, in collaboration with the group of *Prof. Dr. Anouk M. Rijs* using the *free electron laser (FEL)* radiation of FELIX.[86] Since the CH-stretch region (around 3 μm) of smaller PAHs is not molecule specific and dominated by Fermi resonances and anharmonic shifts,[87] the experiments were performed in the fingerprint region between 500 and 1750 cm^{-1}. A detailed overview of the aforementioned experimental and theoretical techniques is presented in **Chapter 2**.

One example of an open-shell molecule that is considered to contribute to molecular growth in reacting environments is the resonantly-stabilized *2-methylallyl radical, C_4H_7 (2-MA)*. This radical has been identified in the combustion of isobutene[88] and *tert*-butyl ethers,[89] which are used as common fuel additives. Also, it might be formed in the ISM *via* the reaction of methylidyne (CH) with propene (C_3H_6).[90] In **Chapter 3**, we recorded the gas-phase IR spectrum of 2-MA and identified several high-temperature reaction products that are formed in competing processes depending on the chosen experimental conditions in the pyrolysis microreactor.[91]

In **Chapter 4**, we extend the work of Chapter 3 and investigate the high-temperature chemistry of the *2-phenylallyl radical, C_9H_9 (2-PA)*, which formally is derived from 2-MA by substituting a methyl group (CH_3) by phenyl (C_6H_5). No spectroscopic information has been reported so far on this radical. In this study, we confirmed the formation of 2-PA from its nitrite precursor by pyrolysis along

with various reaction products based on their gas-phase IR spectra. The identified pyrolysis products demonstrated that similar pathways take place in molecular growth which have already been observed in the study of 2-MA.[92]

Finally, we investigate the non-covalent interactions between the individual monomer units in *benzo[f]quinoline* and *phenanthridine dimers* in **Chapter 5**. Noncovalently bound clusters are of significant interest to astrochemistry and combustion processes, as they represent the early stages of the formation of carbonaceous particles and soot. Additionally, PANHs have recently been proposed as novel electron-conducting materials,[93] showing their relevance in supramolecular chemistry as well as material sciences. While pure aromatic hydrocarbons only form stacked clusters, PANHs additionally can form hydrogen-bonded structures. In a joint experimental and computation study with the group of *Prof. Dr. Roland Mitric*, we revealed a preferential formation of π-stacked configurations for the dimers of benzo[f]quinoline and phenanthridine.[94]

References

[1] J. P. Gardner, J. C. Mather, M. Clampin, R. Doyon, M. A. Greenhouse, H. B. Hammel, J. B. Hutchings, P. Jakobsen, S. J. Lilly, K. S. Long, J. I. Lunine, M. J. Mccaughrean, M. Mountain, J. Nella, G. H. Rieke, M. J. Rieke, H.-W. Rix, E. P. Smith, G. Sonneborn, M. Stiavelli, H. S. Stockman, R. A. Windhorst, G. S. Wright, *Space Sci. Rev.* **2006**, *123*, 485–606.

[2] A. C. Carnall, R. Begley, D. J. McLeod, M. L. Hamadouche, C. T. Donnan, R. J. McLure, J. S. Dunlop, B. Milvang-Jensen, C. L. Bondestam, F. Cullen, S. M. Jewell, C. L. Pollock, *Mon. Not. R. Astron. Soc.* **2023**, *518*, 45–50.

[3] E.-M. Ahrer et al., *Nature* **2023**, *614*, 649–652.

[4] A. Claeyssens, A. Adamo, J. Richard, G. Mahler, M. Messa, M. Dessauges-Zavadsky, *Mon. Not. R. Astron. Soc.* **2023**, *520*, 2180–2203.

[5] NASA Image Gallery, First Deep Field Image, https://www.nasa.gov/image-feature/goddard/2022/nasa-s-webb-delivers-deepest-infrared-image-of-universe-yet/, [Online: accessed January - 9th, 2023], **2023**.

[6] M. D. Lallo, *Opt. Eng.* **2012**, *51*, 1–49.

[7] H. Okuda, *Proc. Jpn. Acad. Ser. B Phys. Biol. Sci.* **2019**, *95*, 495–522.

[8] L. Ashmore in *Unified Field Mechanics*, World Scientific, **2015**, pp. 456–463.

[9] S. N. Bose, *Z. Physik* **1924**, *26*, 178–181.

[10] R. T. Pierrehumbert, *Phys. Today* **2011**, *64*, 33–38.

[11] F. Pauzat, *EAS Publ. Ser.* **2011**, *46*, 75–93.

[12] M. Clampin, *Adv. Sp. Res.* **2008**, *41*, 1983–1991.

[13] A. G. G. M. Tielens, *EAS Publ. Ser.* **2011**, *46*, 3–10.

[14] F. C. Gillett, W. J. Forrest, K. M. Merrill, *Astrophys. J.* **1973**, *183*, 87–93.

[15] R. W. Russell, B. T. Soifer, S. P. Willner, *Astrophys. J.* **1977**, *217*, 149–143.

[16] S. P. Willner, R. W. Russell, R. C. Puetter, B. T. Soifer, P. M. Harvey, *Astrophys. J.* **1979**, *229*, 65–68.

[17] E. Peeters, *Proc. Int. Astron. Union* **2011**, *7*, 149–161.

[18] W. W. Duley, D. A. Williams, *Mon. Not. R. Astron. Soc.* **1981**, *196*, 269–274.

[19] W. W. Duley, D. A. Williams, *Mon. Not. R. Astron. Soc.* **1983**, *205*, 67–70.

[20] A. Sakata, S. Wada, T. Tanabe, T. Onaka, *Astrophys. J.* **1984**, *287*, 51–54.

[21] L. J. Allamandola, A. G. G. M. Tielens, J. R. Barker, *Astrophy. J.* **1985**, *290*, 25–28.

[22] A. Leger, J. L. Puget, *Astron. Astrophys.* **1984**, *137*, 5–8.

[23] A. P. Jones, L. d'Hendecourt, *Astron. Astrophys.* **2000**, *355*, 1191–1200.

[24] E. Peeters, L. J. Allamandola, D. M. Hudgins, S. Hony, A. G. G. M. Tielens, *Astron. Soc. Pac. Conf. Ser.* **2004**, *309*, 141–162.

[25] K. Sellgren, *Astrophys. J.* **1984**, *277*, 623–633.

[26] R. I. Kaiser, N. Hansen, *J. Phys. Chem. A* **2021**, *125*, 3826–3840.

[27] E. V. S. Maciel, N. G. Pereira dos Santos, D. A. Vargas Medina, F. M. Lanças, *Electrophoresis* **2022**, *43*, 1587–1600.

[28] J. D. T. Smith, B. T. Draine, D. A. Dale, J. Moustakas, R. C. Kennicutt, Jr., G. Helou, L. Armus, H. Roussel, K. Sheth, G. J. Bendo, B. A. Buckalew, D. Calzetti, C. W. Engelbracht, K. D. Gordon, D. J. Hollenbach, A. Li, S. Malhotra, E. J. Murphy, F. Walter, *Astrophys. J.* **2007**, *656*, 770–791.

[29] E. Peeters in *Astronomical Observations of the PAH Emission Bands*, EDP Sciences, **2021**, pp. 13–28.

[30] C. W. Bauschlicher, E. Peeters, L. J. Allamandola, *Astrophys. J.* **2008**, *678*, 316–327.

[31] A. Candian, T. H. Kerr, I.-O. Song, J. McCombie, P. J. Sarre, *Mon. Not. R. Astro. Soc.* **2012**, *426*, 389–397.

[32] C. W. Bauschlicher, E. Peeters, L. J. Allamandola, *Astrophys. J.* **2009**, *697*, 311–327.

[33] B. A. McGuire, R. A. Loomis, A. M. Burkhardt, K. L. K. Lee, C. N. Shingledecker, S. B. Charnley, I. R. Cooke, M. A. Cordiner, E. Herbst, S. Kalenskii, M. A. Siebert, E. R. Willis, C. Xue, A. J. Remijan, M. C. McCarthy, *Science* **2021**, *371*, 1265–1269.

[34] D. M. Hudgins, J. Charles W. Bauschlicher, L. J. Allamandola, *Astrophys. J.* **2005**, *632*, 316–332.

[35] M. Rapacioli, C. Joblin, P. Boissel, *Astron. Astrophys.* **2005**, *429*, 193–204.

[36] J. Cernicharo, M. Agúndez, C. Cabezas, N. Marcelino, B. Tercero, J. R. Pardo, J. D. Gallego, F. Tercero, J. A. López-Pérez, P. d. Vicente, *Astron. Astrophys.* **2021**, *647*, L2.

[37] J. Cernicharo, M. Agúndez, C. Cabezas, B. Tercero, N. Marcelino, J. R. Pardo, P. d. Vicente, *Astron. Astrophys.* **2021**, *649*, L15.

[38] J. Cernicharo, M. Agúndez, R. I. Kaiser, C. Cabezas, B. Tercero, N. Marcelino, J. R. Pardo, P. d. Vicente, *Astron. Astrophys.* **2021**, *652*, L9.

[39] A. M. Burkhardt, K. L. K. Lee, P. B. Changala, C. N. Shingledecker, I. R. Cooke, R. A. Loomis, H. Wei, S. B. Charnley, E. Herbst, M. C. McCarthy, B. A. McGuire, *Ap. J. Lett.* **2021**, *913*, L18.

[40] W. S. Adams, *Astrophys. J.* **1941**, *93*, 11.

[41] H. Feuchtgruber, F. P. Helmich, E. F. van Dishoeck, C. M. Wright, *Astrophys. J.* **2000**, *535*, L111–L114.

[42] S. T. Ridgway, D. N. B. Hall, S. G. Kleinmann, D. A. Weinberger, R. S. Wojslaw, *Nature* **1976**, *264*, 345–346.

[43] J. Cernicharo, A. M. Heras, A. G. G. M. Tielens, J. R. Pardo, F. Herpin, M. Guélin, L. B. F. M. Waters, *Astrophys. J.* **2001**, *546*, L123.

[44] J. Cami, J. Bernard-Salas, E. Peeters, S. E. Malek, *Science* **2010**, *329*, 1180–1182.

[45] B. A. McGuire, A. M. Burkhardt, S. Kalenskii, C. N. Shingledecker, A. J. Remijan, E. Herbst, M. C. McCarthy, *Science* **2018**, *359*, 202–205.

[46] C. W. Bauschlicher, A. Ricca, *Astrophys. J.* **2009**, *698*, 275–280.

[47] H. A. Galué, O. Pirali, J. Oomens, *Astron. Astrophys.* **2010**, *517*, A15.

[48] J. Bouwman, A. Bodi, P. Hemberger, *Phys. Chem. Chem. Phys.* **2018**, *20*, 29910–29917.

[49] P. P. Lavvas, A. Coustenis, I. M. Vardavas, *Planet. Space Sci.* **2008**, *56*, 27–66.

[50] J. E. Roser, A. Ricca, *Astrophys. J.* **2015**, *801*, 108.

[51] J. E. Roser, A. Ricca, *Proc. Int. Astron. Union* **2019**, *2019*, 1–3.

[52] E. Herbst, E. F. van Dishoeck, *Annu. Rev. Astron. Astrophys.* **2009**, *47*, 427–480.

[53] R. I. Kaiser, D. S. Parker, A. M. Mebel, *Annu. Rev. Phys. Chem.* **2015**, *66*, 43–67.

[54] N. Prantzos in *Encyclopedia of Astrobiology*, Springer, Berlin, Heidelberg, **2011**, pp. 117–118.

[55] D. S. N. Parker, R. I. Kaiser, *Chem. Soc. Rev.* **2017**, *46*, 452–463.

[56] P. Schmitt-Kopplin, Z. Gabelica, R. D. Gougeon, A. Fekete, B. Kanawati, M. Harir, I. Gebefuegi, G. Eckel, N. Hertkorn, *Proc. Natl. Acad. Sci. U.S.A* **2010**, *107*, 2763–2768.

[57] F. L. Plows, J. E. Elsila, R. N. Zare, P. R. Buseck, *Geochim. Cosmochim. Acta* **2003**, *67*, 1429–1436.

[58] M. Frenklach, D. W. Clary, W. C. Gardiner, S. E. Stein, *Symp. (Int.) Comb.* **1985**, *20*, 887–901.

[59] M. Frenklach, *Phys. Chem. Chem. Phys.* **2002**, *4*, 2028–2037.

[60] A. Tielens, *Annu. Rev. Astron. Astrophys.* **2008**, *46*, 289–337.

[61] H. Richter, J. B. Howard, *Prog. Energy Combust. Sci.* **2000**, *26*, 565–608.

[62] H. Wang, M. Frenklach, *Combust. Flame* **1997**, *110*, 173–221.

[63] B. Shukla, M. Koshi, *Phys. Chem. Chem. Phys.* **2010**, *12*, 2427–2437.

[64] T. Schmidt, *Int. Rev. Phys. Chem.* **2016**, *35*, 209–242.

[65] M. Frenklach, E. D. Feigelson, *Astrophys. J.* **1989**, *341*, 372.

[66] E. R. Micelotta, A. P. Jones, A. G. G. M. Tielens, *Astron. Astrophys.* **2010**, *510*, A37.

[67] E. R. Micelotta, A. P. Jones, A. G. G. M. Tielens, *Astron. Astrophys.* **2010**, *510*, A36.

[68] I. Cherchneff, *EAS Publ. Ser.* **2011**, *46*, 177–189.

[69] S. Doddipatla, G. R. Galimova, H. Wei, A. M. Thomas, C. He, Z. Yang, A. N. Morozov, C. N. Shingledecker, A. M. Mebel, R. I. Kaiser, *Sci. Adv.* **2021**, *7*, 1–11.

[70] D. S. N. Parker, F. Zhang, Y. S. Kim, R. I. Kaiser, A. Landera, V. V. Kislov, A. M. Mebel, A. G. G. M. Tielens, *Proc. Natl. Acad. Sci. U. S. A.* **2012**, *109*, 53–58.

[71] Z. Peeters, O. Botta, S. B. Charnley, R. Ruiterkamp, P. Ehrenfreund, *Astrophys. J.* **2003**, *593*, L129.

[72] M. P. Callahan, K. E. Smith, H. J. Cleaves, J. Ruzicka, J. C. Stern, D. P. Glavin, C. H. House, J. P. Dworkin, *Proc. Natl. Acad. Sci. U. S. A.* **2011**, *108*, 13995–13998.

[73] Z. Martins, O. Botta, M. L. Fogel, M. A. Sephton, D. P. Glavin, J. S. Watson, J. P. Dworkin, A. W. Schwartz, P. Ehrenfreund, *Earth Planet. Sci. Lett.* **2008**, *270*, 130–136.

[74] S. Russell in *Encyclopedia of Geochemistry: A Comprehensive Reference Source on the Chemistry of the Earth*, Springer International Publishing, Cham, **2018**, pp. 248–251.

[75] D. S. N. Parker, R. I. Kaiser, O. Kostko, T. P. Troy, M. Ahmed, A. M. Mebel, A. G. G. M. Tielens, *Astrophys. J.* **2015**, *803*, 53.

[76] D. B. Rap, J. G. M. Schrauwen, A. N. Marimuthu, B. Redlich, S. Brünken, *Nat. Astron.* **2022**, *6*, 1059–1067.

[77] D. S. N. Parker, R. I. Kaiser, O. Kostko, T. P. Troy, M. Ahmed, B.-J. Sun, S.-H. Chen, A. H. H. Chang, *Phys. Chem. Chem. Phys.* **2015**, *17*, 32000–32008.

[78] A. Ricca, C. W. Bauschlicher, E. L. O. Bakes, *Icarus* **2001**, *154*, 516–521.

[79] D. W. Kohn, H. Clauberg, P. Chen, *Rev. Sci. Instrum.* **1992**, *63*, 4003–4005.

[80] Q. Guan, K. N. Urness, T. K. Ormond, D. E. David, G. Barney Ellison, J. W. Daily, *Int. Rev. Phys. Chem.* **2014**, *33*, 447–487.

[81] A. Vasiliou, M. R. Nimlos, J. W. Daily, G. B. Ellison, *J. Phys. Chem. A* **2009**, *113*, 8540–8547.

[82] R. E. Smalley, L. Wharton, D. H. Levy, *Acc. Chem. Res.* **1977**, *10*, 139–145.

[83] A. M. Rijs, J. Oomens, *Top. Curr. Chem.* **2014**, *364*, 1–42.

[84] A. Hamachi, T. Okuno, T. Imasaka, Y. Kida, T. Imasaka, *Anal. Chem.* **2015**, *87*, 3027–3031.

[85] P. Geerlings, F. De Proft, W. Langenaeker, *Chem. Rev.* **2003**, *103*, 1793–1874.

[86] D. Oepts, A. F. G. van der Meer, P. W. van Amersfoort, *Infrared Phys. Technol.* **1995**, *36*, 297–308.

[87] E. Maltseva, A. Petrignani, A. Candian, C. J. Mackie, X. Huang, T. J. Lee, A. G. G. M. Tielens, J. Oomens, W. J. Buma, *Astrophys. J.* **2015**, *814*, 23.

[88] C.-W. Zhou, Y. Li, E. O'Connor, K. P. Somers, S. Thion, C. Keesee, O. Mathieu, E. L. Petersen, T. A. DeVerter, M. A. Oehlschlaeger, G. Kukkadapu, C.-J. Sung, M. Alrefae, F. Khaled, A. Farooq, P. Dirrenberger, P.-A. Glaude, F. Battin-Leclerc, J. Santner, Y. Ju, T. Held, F. M. Haas, F. L. Dryer, H. J. Curran, *Combust. Flame* **2016**, *167*, 353–379.

[89] T. Zhang, J. Wang, T. Yuan, X. Hong, L. Zhang, F. Qi, *J. Phys. Chem. A* **2008**, *112*, 10487–10494.

[90] J. M. Ribeiro, A. M. Mebel, *J. Phys. Chem. A* **2016**, *120*, 1800–1812.

[91] T. Preitschopf, F. Hirsch, A. K. Lemmens, A. M. Rijs, I. Fischer, *Phys. Chem. Chem. Phys.* **2022**, *24*, 7682–7690.

[92] T. Preitschopf, F. Sturm, I. Stroganova, A. K. Lemmens, A. M. Rijs, I. Fischer, *Chem. Euro. J.* **2023**, *29*, e202202943.

[93] L. Ahrens, J. Butscher, V. Brosius, F. Rominger, J. Freudenberg, Y. Vaynzof, U. H. F. Bunz, *Chem. Eur. J.* **2020**, *26*, 412–418.

[94] X. Miao, T. Preitschopf, F. Sturm, I. Fischer, A. K. Lemmens, M. Limbacher, R. Mitric, *J. Phys. Chem. Lett.* **2022**, 8939–8944.

CHAPTER 2

METHODS

2.1 Spectroscopic Techniques

Depending on the area of application, various techniques are used to ionize atoms or molecules, among them the widespread matrix-assisted laser desorption ionization (MALDI)[1] and electron ionization (EI)[2] approaches. As the latter commonly leads to fragmentation,[3] photoionization (PI) serves as an alternative soft ionization method that hampers unwanted fragmentation.[4] Due to increasingly available high-intensity light sources, this technique gained considerable popularity in many research-based applications.[4] In this work, laser-based single-photon ionization (SPI), see Section 2.1.1,[5] and resonance-enhanced multiphoton ionization (REMPI), see Section 2.1.2,[6] were employed for the analysis of (nitrogenated) hydrocarbons in the gas-phase. While SPI generally utilizes vacuum ultraviolet (VUV) radiation (around 105−165 nm) to ionize the vast majority of hydrocarbons,[7,8] REMPI is highly selective and sensitive for aromatic hydrocarbons using UV light in the range of 193−350 nm.[9]

As several isomers may contribute to one ion signal generated by PI, mass spectrometry is not sufficient to provide reliable structure assignments.[10] Therefore, structure-sensitive techniques have to be applied for an isomer-specific characterization of a given system. One approach is to record photoionization efficiency curves (PIE) by scanning the VUV photon energy.[10,11] A second dimension to this method is added by simultaneously detecting the photoelectron kinetic energy, which results in mass-selected threshold photoelectron spectroscopy (TPES) using the photoelectron photoion coincidence (PEPICO) method.[12,13] This technique provides structural information with high detection sensitivity,[13] and has been successfully applied for the isomer-specific identification of elusive intermediates and their reaction products in reactive environments.[14–16] For weakly bound systems, however, such as van der Waals clusters, often a resolution of around one cm^{-1} is required because small errors in the measured ionization energy (IE) can result in a false characterization of the system.[13] This condition is usually not fulfilled using TPES.[13] Instead, conformer-selectivity is accomplished *via* double-resonance techniques, that typically approach two transitions sharing a mutual lower state.[17] These methods generally comprise "hole-burning" and "ion dip" spectroscopy.[18,19] Both techniques are based on inducing a population change in the electronic ground state using UV or IR excitation, followed by a REMPI or laser-induced fluorescence (LIF) process.[17] In hole-burning spectroscopy the excitation laser frequency is fixed and the probe laser is scanned, while in ion dip spectroscopy the excitation laser is tuned and the probe laser frequency is fixed.[17] In this thesis, IR/UV ion dip spectroscopy (IR/UV-IDS), see Section 2.1.3, was uti-

lized to record conformation specific IR spectra using a free electron laser (FEL)[20] as an intense IR excitation light source.[17] This technique was recently applied to characterize inter- and intramolecular interactions of biomolecules[21,22], weakly-bound clusters,[23,24] and reactive intermediates.[25–27]

2.1.1 Single-Photon Ionization

One of the simplest and most efficient PI methods is achieved when atoms or molecules are exposed to VUV radiation. If the photon energy $h\nu$ surpasses the IE of the investigated species as illustrated in Figure 2.1, SPI initially forms two charged particles, an intact cation and an electron.[4] Any photon energy exceeding the IE is deposited into the kinetic energy of the electron and the internal energy of the cation.[28] Laboratories without access to VUV synchrotron radiation commonly utilize pulsed laser-based sources to generate VUV radiation with a photon energy of 10.5 eV.[4] As this energy is in the range of the IE of the vast majority of organic molecules (<10 eV),[29] the excess energy deposited into the cation is small which results in nearly no fragmentation of the investigated species.[30] Hence, 10.5 eV SPI is particularly well-suited for a thorough investigation of complex reaction mixtures. Generally, pulsed radiation with a photon energy of 10.5 eV is obtained by frequency tripling of the third harmonic (355 nm) of a neodymium-

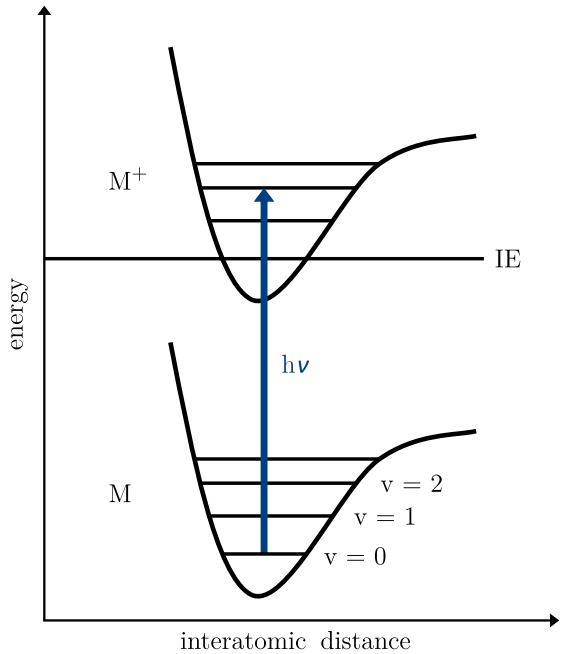

Figure 2.1. Photoionization of a molecule M with a single photon (SPI).

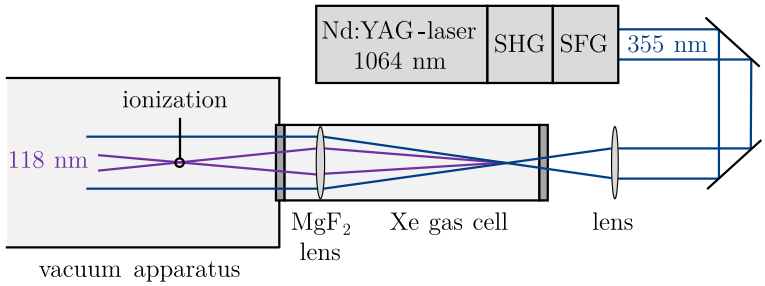

Figure 2.2. Tripling of the third harmonic of a Nd:YAG-laser in a xenon gas cell.

doped yttrium aluminum garnet (Nd:YAG) laser in a xenon or xenon/argon gas cell,[31,32] producing 118.2 nm with pulse lengths of a few nanoseconds,[30] see Figure 2.2.

The ion yield Y_{ion} generated by SPI depends on the SPI cross section σ_{SPI} of the gaseous atom or molecule, the VUV radiation intensity I and the number density of the gaseous neutral atoms or molecules Y_{gas} and is given by[6,33]

$$Y_{ion} = \sigma_{SPI} \cdot I \cdot Y_{gas}. \tag{2.1}$$

The ionization efficiency is mainly determined by σ_{SPI}, which varies by approximately one order of magnitude between ∼10−100 Mb (1 megabarn = 10^{-18} cm^2) for the vast majority of organic molecules at 10.5 eV.[34,35] Often, the cross section σ_{SPI} approaches 10 Mb around 1 eV above the IE,[36] which allows for a rough quantification of the relative molecular concentrations in the sample as opposed to other PI techniques such as REMPI.[4]

2.1.2 Resonance-Enhanced Multiphoton Ionization

Atoms or molecules can also be ionized with two or more photons in a multiphoton ionization (MPI) process. This technique can be classified into nonresonant multiphoton ionization (NRMPI) and resonance-enhanced multiphoton ionization (REMPI).[37]

The simplest case of MPI constitutes the consecutive absorption of two photons. In REMPI, the energy of the first photon is in resonance with an intermediate excited electronic state of the neutral molecule. Subsequently, the excited molecule is ionized by absorbing a second photon within the lifetime of the intermediate state with a photon energy exceeding the gap between the excited state and the ionization threshold,[6,37] see Figure 2.3a. In the research described in this thesis, pulsed nanosecond lasers with a narrow spectral bandwidth were used. Hence, molecules with long excited state lifetimes in the nanosecond range are advantageous for

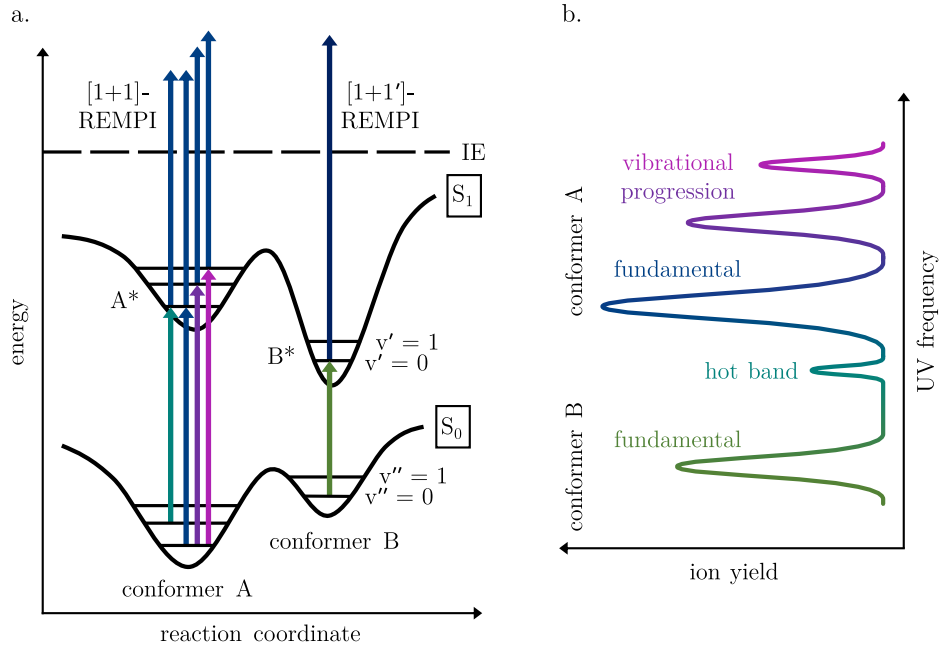

Figure 2.3. a) Schematic representation of an one color [1+1] and two color [1+1'] two-photon REMPI process for two different conformers A and B. b) Corresponding UV absorption spectrum of the REMPI scheme shown in a).

an efficient REMPI process.[17] Many PAHs observed in this thesis exhibit excited singlet state lifetimes between ∼10−1000 ns.[38,39] Additionally, they typically possess IEs below 9 eV,[40] allowing for the use of a single UV frequency for excitation and ionization originating from the same laser (one-color resonant two-photon ionization (R2PI) or [1+1]-REMPI), see left side of Figure 2.3a.[17] If the energy of the excited state is smaller than half of the IE of a molecule, two-color R2PI or [1+1']-REMPI has to be applied (see right side of Figure 2.3a).[17] Therefore, two independent lasers are required which allows to choose the UV frequency of the second laser freely to maximize the ionization efficiency.[17] The photon energy of the ionization laser should be kept as small as possible to reduce unwanted fragmentation. Since the two laser have to be overlapped both spatially as well as temporally to account for the lifetime of the electronically excited state, two-color REMPI is significantly more challenging than its one-color counterpart.

In general, the efficiency in REMPI is significantly higher than in NRMPI,[37] allowing for the on-line analysis of trace species (parts per trillion concentration) in complex gas mixtures.[4,9] The ion yield Y_{ion} is approximately given by[6,41,42]

$$Y_{ion} \approx \frac{1}{2} \cdot Y_{gas} \cdot \sigma_{GS} \cdot \sigma_{ES} \cdot I^2, \tag{2.2}$$

if saturation of the resonant transition is avoided by using sufficiently low laser intensities. In Eq. (2.2), Y_{gas} denotes the number density of the gaseous neutral atoms or molecules, σ_{GS} and σ_{ES} describe the absorption cross sections of the ground and excited state, and I is the laser intensity.

A common REMPI spectrum exhibits a wealth of peaks besides the $S_1 \longleftarrow S_0$ origin transition as shown in Figure 2.3b (blue for conformer A and green for conformer B). At higher photon energies, vibrational progressions (series of transitions with a common lower state to vibrationally excited states of an electronically excited state,[43] highlighted in violet in Figure 2.3) are observed.[17] Red-shifted to the origin, a hot band (transition from an excited vibrational state in the electronic ground state to an electronically excited state,[44] highlighted in cyan in Figure 2.3) may appear even despite supersonic cooling in a molecular beam experiment.[17] Additionally, several conformers with different $S_1 \longleftarrow S_0$ transition energies possibly coexist for an investigated system (highlighted in green in Figure 2.3).[17] This enables a conformer-selective investigation in double-resonance experiments such as IR/UV-IDS, provided that the excitation laser frequency is set to an unique transition of a specific conformer. However, each conformer might exhibit its own vibrational progression, possibly leading to a highly complex or even broad REMPI spectrum due to insufficient cooling.[17]

2.1.3 IR/UV Ion Dip Spectroscopy

In conventional infrared *absorption* spectroscopy, the absorbance of a sample as a function of the IR frequency is obtained by measuring the IR intensity before and after passing the sample, according to the Lambert-Beer law.[45] Generally, the particle number density and optical path length in molecular beam experiments is so low, that this intensity difference is very difficult to measure.[17,46] In IR *action* spectroscopy, the influence of IR radiation on the molecules is investigated, *e.g.* its impact on the ion yield as a function of the frequency,[17] rather than examining the effect of molecules on the light. Several types of IR action spectroscopy have been developed over the years, among them IR multiple photon dissociation spectroscopy,[17] IR/UV fluorescence depletion spectroscopy,[47], or IR/VUV action spectroscopy.[17] In this work, IR/UV ion dip spectroscopy[48] (IR/UV-IDS) was utilized on neutral molecules in a free jet as another powerful type of action spectroscopy, which is based on the change of the vibrational population in the ground state of a molecule by IR absorption, followed by REMPI.[17] A more detailed insight into this method is given in the following.

Fundamental principle

For IR/UV-IDS a constant ion signal of a specific conformer in its electronic and vibrational ground state is produced by setting the UV laser on a unique transition in its REMPI spectrum. Typically around 100−400 ns prior to the UV pulse, the neutral molecules are illuminated with IR radiation of a tunable IR laser that is scanned over a certain frequency range. When the IR frequency is resonant with a vibrationally excited state of the investigated conformer, its ground state gets depopulated and the detected ion signal decreases (*dip*) when probed by the UV laser,[17] see Figure 2.4a. The number of vibrationally excited molecules as a function of the IR frequency $Y(\nu)$ mainly depends on the number density of the gaseous neutral molecules Y_{gas}, the IR photon fluence $\Phi(\nu)$, and the IR absorption cross section $\sigma(\nu)$ according to[17]

$$Y(\nu) = Y_{gas} \cdot e^{-\sigma(\nu)\cdot\Phi(\nu)}. \tag{2.3}$$

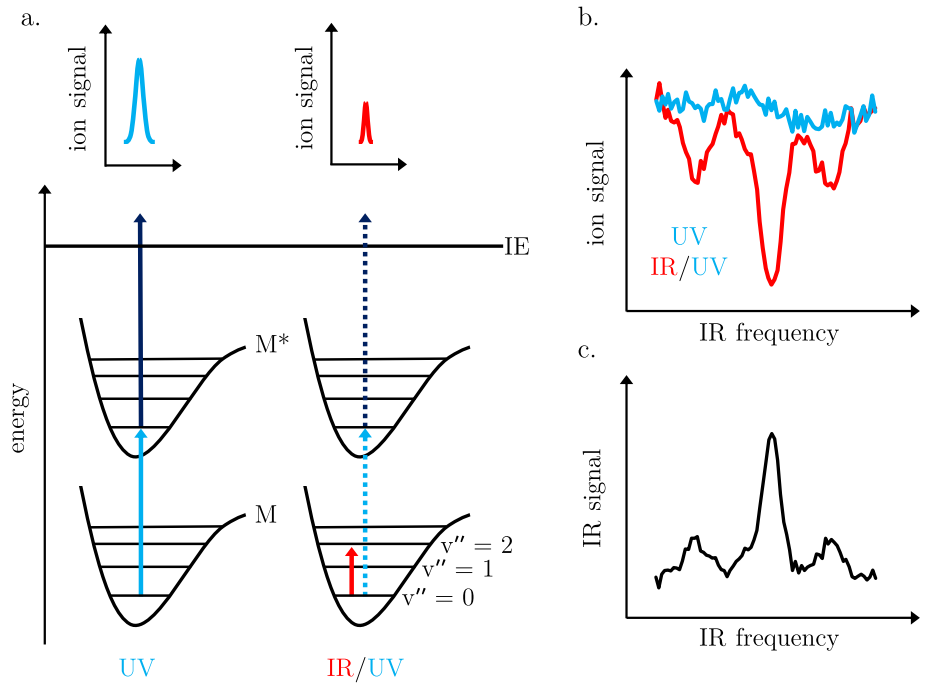

Figure 2.4. a) Schematic illustration of the mechanism of IR/UV ion dip spectroscopy. A depleted ion signal is observed upon resonant IR excitation. b) Alternating IR-OFF (blue) and IR-ON (red) ion yields are obtained when the UV frequency is fixed while the IR laser is scanned. c) Dividing the IR-OFF signal by the IR-ON signal and taking the decadic logarithm results in the mass-selected IR absorption spectra.

To facilitate a comparison of the experimental spectra with theory, the ion dip spectra (Figure 2.4b) are translated into absorbance spectra (Figure 2.4c). The absolute absorbance values depend on various experimental parameters such as the photon energy, pulse length, laser beam cross section, or the transmission of windows inside the beam path, which are challenging to measure on-line in a molecular beam experiment.[49] Therefore, only relative intensities A were derived assuming a single IR photon process:

$$A \sim \nu / P^0_{laser}(\nu) \cdot \log_{10}\left(\frac{Y_{IR_{OFF}}}{Y_{IR_{ON}}}\right), \tag{2.4}$$

where $P^0_{laser}(\nu)$ denotes the initial laser power and $Y_{IR_{ON}}$ and $Y_{IR_{OFF}}$ are the constant ion signals with and without IR radiation.[49]

Detailed insight into the underlying processes

Unambiguous assignments of experimental IR/UV spectra by theory are not only based on the positions of the IR absorption bands but also their intensities. Yet, in some cases, low-frequency absorption modes are observed with a much higher intensity than predicted by theory.[50] This demonstrates that an in-depth understanding of the underlying processes is pivotal for an accurate interpretation of the IR ion dip spectra.

As described above, a depleted ion signal generally results from a difference in the UV absorption by the cold and IR "preheated" molecules as a consequence from the difference in vibrational frequencies in the electronic ground and excited state, and/or reduced Frank-Condon (FC) factors.[51,52] Yet, the observed depletion of the ion signal commonly exceeds 50 %, in particular when high pulse energies are applied. Hence, a simple two-level system consisting of the vibrationally ground and excited state is not adequate to sufficiently characterize the IR absorption step.[53] Consequently, other events must take place, such as IR-induced fragmentation or redistribution of vibrational energy over the bath of vibrational background states of the molecule by intramoleculer vibrational energy redistribution (IVR).[17,54,55] The latter results in a rapid depopulation of the vibrationally excited state, allowing for the absorption of additional IR photons.[54] This typically results in broadened IR ion dip absorption bands which are affected in their relative intensity.[17]

One approach to uncover the various ion depletion mechanisms is to fix the IR laser on a specific vibrational transition of the molecule and record REMPI excita-

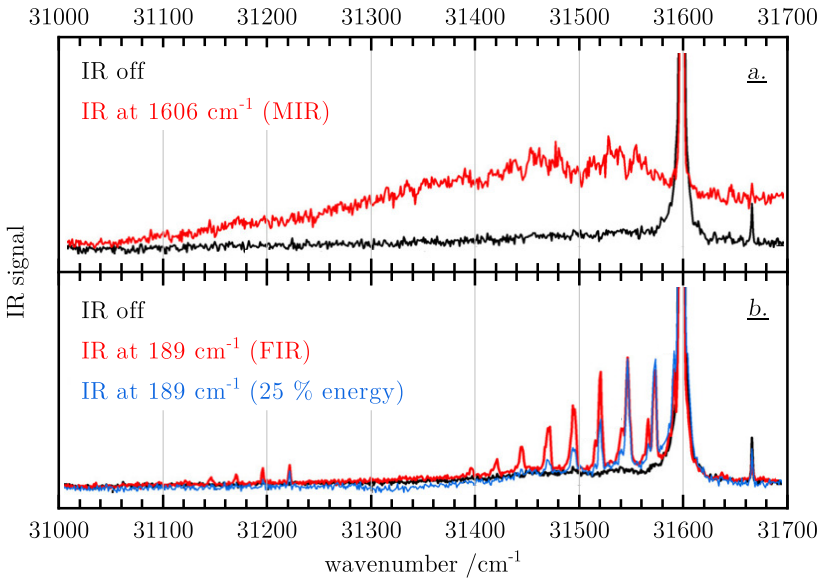

Figure 2.5. REMPI excitation spectra recorded at the $S_1 \leftarrow S_0$ origin transition of acenaphthene-d_{10} after (red and blue) and without IR excitation (black) in the MIR (trace a) and the FIR region (trace b). Adapted with permission from Ref. [50]. Copyright 2020 American Chemical Society.

tion spectra after IR absorption.[50,52,56] This technique allows to simultaneously probe the depopulation of the vibrational ground state as well as the population of vibrationally excited states.[52]

Figure 2.5, adapted with permission from Ref. [50], depicts the REMPI excitation spectra near the $S_1 \longleftarrow S_0$ origin band of acenaphthene-d_{10} without (in black) and after (in red and blue) resonant IR excitation in the MIR (trace a) and far-infrared (FIR) region (trace b). Broad and unstructured infrared ion gain (IRIG) signals at lower and higher wavenumbers relative to the origin band are shown in trace a, because excitation of a MIR band results in statistical inhomogeneous broadening of the origin band by IVR due to the high density of states (DOS) at this photon energy.[52] Conversely, distinctive IRIG signals are observed in the REMPI spectrum after excitation of a FIR band (trace b). This suggests, that the vibrational excitation is distributed over only a few eigenstates as a consequence of a much lower DOS at this photon energy in comparison with the MIR region.[50,52]

The potential IR and UV excitation routes leading to resolved IRIG features in the FIR region are presented in Figure 2.6. In a harmonic potential energy surface, higher vibrational levels are populated consecutively in a *ladder climbing* process at the IR photon energy of the excited fundamental vibrational transition (Figure 2.6a). Subsequently, the distribution is probed by the UV laser resulting

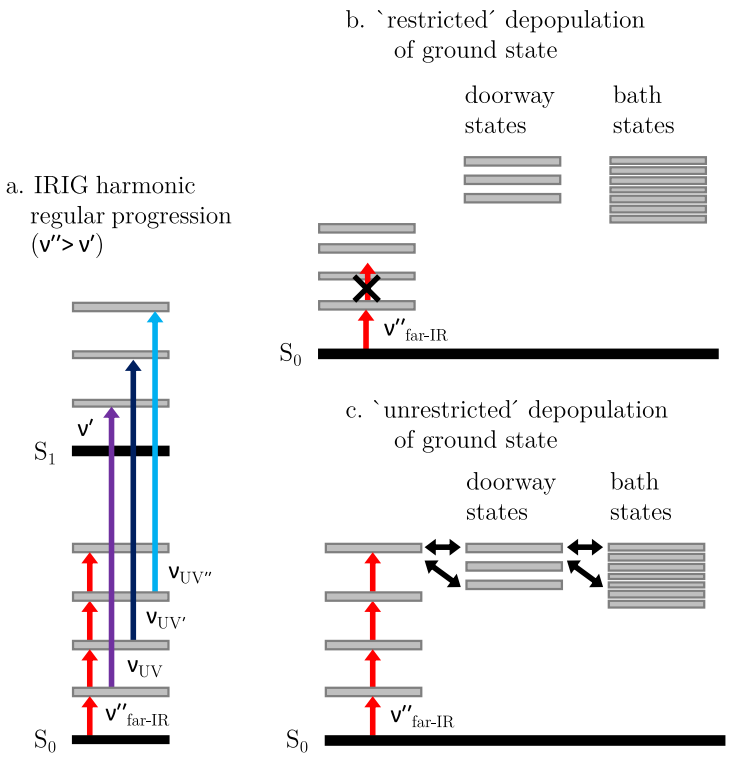

Figure 2.6. a) Schematic illustration of ladder climbing in a harmonic potential. b) Ladder climbing in an anharmonic potential is restricted due to nonequidistant vibrational levels which mainly impedes IVR for low-frequency modes. c) Ladder climbing in a harmonic potential leading to new IVR pathways. Adapted with permission from Ref. [50]. Copyright 2020 American Chemical Society.

in resolved and regularly spaced ion gain bands in the REMPI excitation spectrum (see Figure 2.5b).[50] The progression is a consequence from UV transitions between vibrational levels in the electronic ground and excited state with the same vibrational quantum number $(\nu_i)_{v''=n}^{v'=n}$ (Figure 2.6a).[50] In contrast, in an anharmonic potential energy surface, absorption is limited to a single IR photon due to nonequidistant vibrational levels which inhibits ladder climbing (Figure 2.6b). In addition, efficient IVR is hampered due to the low DOS in the FIR region leading to a maximum depopulation of 50 % of the ground state.[50] In harmonic vibrational modes, however, higher IR pulse energies allow to reach higher vibrational levels, which results in enhanced IVR, see Figure 2.6c. This facilitates the absorption of further IR photons and a depopulation of >50 % of the ground state.[50]

Consequently, the depletion mechanism critically depends on (i) the IR photon energy, (ii) the (an)harmonic character of the excited vibrational mode, and (iii) the

IR laser power.[50] All three can initiate different processes such as ladder climbing, IVR, and IR-induced fragmentation, which might introduce a nonlinearity into the intensity of the IR ion dip absorption bands.[50] Additionally, ion gain is not only correlated with IR cross sections as the absorption band intensities further depend on the UV frequencies that are chosen in the IR/UV experiment. Even for low IR pulse energies, IRIG signals might be observed in the IR/UV spectrum at certain UV wavelengths.[50] Hence, various events might contribute to the spectral pattern in IR/UV spectroscopy which results in a more complex analysis of IR/UV spectra.

IR/UV-IDS *via* broadened and unstructured electronic bands

Generally, the fundamental principle of IR/UV-IDS is described to proceed *via* distinct features in the REMPI spectrum of cold molecules. However, the UV spectra of some systems exhibit only broadened and unstructured bands without any distinct signals. This either suggests short excited state lifetimes (<1 ns), a high DOS of rovibronic states, or the presence of several isomers with UV features that overlap due to insufficient cooling.[17,57] Yet, IR/UV-IDS often can still be successfully performed despite a broad and structureless REMPI spectrum as shown in the research of this thesis and previous studies.[56,58–60] At high IR photon energies, this effect is based on an efficient redistribution of the vibrational excitation over a large number of vibrational modes as described above.[56] For low frequency modes, high IR pulse energies have to be utilized to induce a subsequent absorption of further IR photons in a ladder climbing process which allows IVR to occur more easily. Both cases lead to broadened UV signals in the IR-excited REMPI spectrum (*cf.* Figure 2.5) which results in a reduced ionization yield at any given UV wavelength.[56] For molecules with a completely unstructured REMPI spectrum, IR excitation at high IR photon and pulse energies thus effectively causes a disappearing IR-excited REMPI spectrum.[56] Consequently, a negligible ionization yield is observed after vibrational excitation for each UV wavelength in IR/UV-IDS, which facilitates to monitor IR ion dip absorption bands in the IR/UV spectrum.[56]

2.1.4 Comparison of Structure-Sensitive Spectroscopic Techniques

Various spectroscopic techniques are commonly applied to investigate the structure of molecules in a supersonic expansion. In the following, IR/UV-IDS is briefly compared to the SPI methods PIE and TPES as well as to the REMPI technique to outline its strengths but also weaknesses for possible applications in the future.

Generally, REMPI spectroscopy allows to selectively ionize a specific isomer in a jet expansion by choosing a unique rovibronic intermediate state of the molecule of interest.[6] This characterization typically holds true for sufficiently cold molecular beams, which results in well-resolved and distinct UV features in the REMPI spectrum.[41] For insufficiently cooled molecules, *e.g.* in combination with high-temperature experiments such as pyrolysis studies, the selectivity of REMPI is lost due to broadened UV features as a result of the high DOS.[61] In contrast, product identification in warm molecular beams can still be achieved using IR/UV-IDS as shown in the work of this thesis (*cf.* Chapter 3). However, scanning a wide UV wavelength region (200−350 nm) covers several electronic transitions for a given isomer, which might allow for an isomer-specific identification despite a predominantly broad UV spectrum.[61] This approach has for example successfully been applied to identify several aromatic hydrocarbons formed in a fuel-rich flame.[61] Yet, a straightforward identification generally requires a benchmark of reference REMPI spectra. However, until now, only few reference spectra exist that cover a wide temperature range (100−300 K). This is particularly important as the spectral pattern might significantly vary at different temperatures.[61] In addition, assignments *via* gas-phase UV/VIS absorption spectra are not unambiguous, as excited state lifetimes as well as photoionization efficiencies might result in different patterns in the REMPI spectrum.[61] Conversely, a large data base of (gas-phase) reference spectra is available for IR spectroscopy which facilitates a straightforward identification. Additionally, low-level quantum chemical simulations of IR absorption spectra for small molecules often yield a good agreement with the experimental spectra (*cf.* Chapter 3 and 4).

As IR/UV-IDS utilizes R2PI, both spectroscopic techniques suffer from an intrinsic lack of sensitivity, since molecules without an UV chromophore such as unsaturated alkenes are not identifiable. However, a complete detection is particularly relevant for an accurate characterization of complex systems as shown in Chapter 3. One approach of an isomer-specific identification of molecules without a UV chromophore is to record PIE curves using tunable synchrotron radiation. Here, the ion signal of a mass peak in the TOF-mass spectrum (MS) is monitored as a function of the VUV photon energy.[10] The resulting curve is then reproduced by a linear combination of known reference PIE curves of individual isomers.[62] This allows for an isomer-specific identification as well as to determine branching ratios when taking ionization cross sections into account.[62] The latter constitutes another advantage over IR/UV-IDS. Here, quantification of the relative molecular concentrations in the molecular beam relies on the absolute IR absorbance values, which depend on several varying experimental parameters that are difficult

to monitor on-line as shown in Section 2.1.3.[49] For larger molecules, however, a qualitative identification of the various isomers using PIE curves becomes significantly more challenging due to their similar IEs.[62]

TPES combined with PEPICO techniques further constitutes a complementary spectroscopic technique that allows to unravel isomer-specific reaction mechanisms in reacting environments.[13,15] Here, the photoelectron and photoion from each photoionization event are correlated and detected in coincidence resulting in mass-selected threshold photoelectron (TPE) spectra.[12,13,63] While this technique is particularly well-suited to investigate small molecules,[13] larger molecules, however, often exhibit broad and featureless TPE spectra due to the high DOS. Furthermore, an unstructured TPE spectrum is observed upon a significant geometry change of the ion state relative to the neutral,[13] see *e.g.* Figure S15 and S16 in the Appendix. Conversely, this effect does not affect successful measurements of PIE curves as well as of IR/UV spectra. From an experimental view, the latter two methods further constitute a significantly less challenging analysis technique, as they are based on monitoring the ion flow of each mass. In contrast, TPES using PEPICO additionally records the kinetic photoelectron energy which requires a considerably advanced experimental apparatus as well as a more complex data acquisition scheme.[64]

The investigation of a complex system such as reaction products in reactive environments by IR/UV-IDS requires reasonably sufficient absorption around the chosen UV photon energy. Typically, many aromatic hydrocarbons such as PAHs, which are investigated in the research of this thesis (Chapter 3 and 4), possess broad absorption bands in the range of 220−320 nm.[38,65] Often, an excitation wavelength around 266 nm is chosen, as the strong $S_3 \leftarrow S_0$ transitions of PAHs as well as the medium strong $S_2 \leftarrow S_0$ of some small PAHs are located in this wavelength region.[65] In addition, the photon energy around this wavelength (∼4.66 eV) commonly exceeds half of the IE of the vast majority of PAHs,[40] allowing for one-color R2PI. For PAHs that do not absorb at a certain UV frequency (*e.g.* acenaphthylene exhibits no absorption around 266 nm),[65] a complete detection might be obtained when performing IR/UV-IDS at several UV wavelengths. However, as some reaction products still might not be detected, IR/UV-IDS can only help to unravel some reaction mechanisms that occur in reacting environments.

In conclusion, IR/UV-IDS is a powerful method to investigate complex systems such as biomolecules,[60] clusters,[66] or reacting environments.[67] However, limits are reached when molecules with short excited state lifetimes or without an UV chromophore are investigated. Furthermore, quantitative determinations are challenging as they are based on various parameters that are difficult to monitor

on-line. Here, complementary methods such as PIE or TPES have to be taken into account for a comprehensive investigation of complex systems.

2.2 Experimental Details

The most important experimental methods used in this thesis to perform IR/UV-IDS of reactive intermediates and PANH clusters are introduced in the following section. As open shell molecules are typically thermodynamically stable but highly reactive towards bimolecular reactions, they have to be generated *in situ* from suitable precursors. Therefore, flash pyrolysis was applied using flow microreactors[68] that can further initiate uni- and bimolecular reactions,[69] as explained in Section 2.2.1. Due to their high reactivity, the research on these species needs to be performed in isolation. One approach is to trap the molecules in an argon-matrix in combination with Fourier-transform infrared (FT-IR) spectroscopy.[70] More commonly, the radicals are seeded in a noble gas such as argon or helium and expanded into vacuum, thereby creating a free jet,[71] see Section 2.2.2. Here, translationally, rotationally and vibrationally cold molecules can be studied using IR/UV-IDS resulting in ground-state IR spectra. The spectroscopy is performed in a TOF mass spectrometer,[17] which allows to monitor the parent molecules, potential fragments, clusters and reaction products in parallel. The experimental setup used in this thesis is discussed in more detail in Section 2.2.3. As an intense IR light source is required that additionally covers a wide IR photon energy range, FEL radiation was employed. The basic principles of the latter are presented in Section 2.2.4. Finally, commercially available optical parametric oscillator (OPO)/optical parametric amplifier (OPA) laser systems are discussed as another source of IR radiation that allow to perform IR/UV-IDS on a laboratory scale (Section 2.2.4).

2.2.1 Flash Pyrolysis

Several techniques such as electrical discharges[72] or photolysis[73] have been developed to generate open shell molecules *in situ*. While electrical discharges are rather harsh and non-selective, photolysis constitutes one of the most selective and widely used techniques to generate radicals.[74] However, it is typically prone to produce radicals at a low number density in the gas-phase due to a rather small conversion coefficient. In contrast, flash pyrolysis allows to generate radicals cleanly at a high-number density by unimolecular thermal decomposition of suitable organic precursors.[68] In this thesis, a high-temperature pulsed flash py-

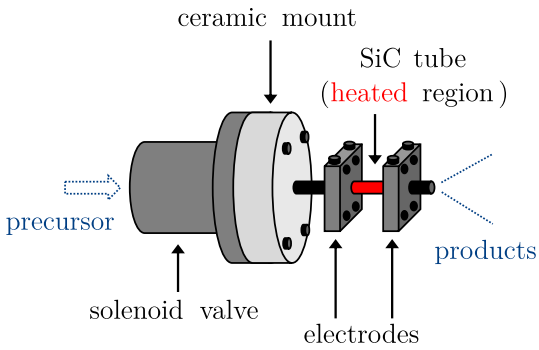

Figure 2.7. Schematic representation of a Chen pyrolysis nozzle.[68]

rolysis nozzle following the design of Peter Chen[68] was utilized for the pyrolytic formation of jet-cooled reactive intermediates. A schematic representation of such a *Chen Nozzle* is given in Figure 2.7. The nozzle consists of a 30−40 mm silicon carbide (SiC) tube (*Saint Gobain Keramik, Hexoloy Se*) with an inner diameter of 1.0 mm, which is mounted onto a solenoid valve (Series 9, *Parker General Valve*) *via* a ceramic tube. The latter acts as a thermal insulator to prevent excessive heating of the valve. Two stainless-steel electrode blocks are attached at the tube at a distance of 5−10 mm to each other, which determines the length of the heated region of the pyrolysis unit.

The reactive intermediates are generated at temperatures between 600−1800 K by cleaving appropriate organic precursors that are seeded in a noble gas (Ar or He, 1−3 bar). The design of the pyrolysis nozzle allows to achieve very short residence times in the pyrolysis tube (around 25 to 150 μs)[69] to suppress secondary reactions such as radical recombination or disproportionation.[68] In fact, computational fluid dynamics simulations showed that the vast majority of reactions occur in a "sweet spot" within the reactor, resulting in significantly shorter time spans over which the reactions take place.[69] Despite the short contact time, high conversion efficiencies are still preserved by increasing the pyrolysis temperature.[68] The flow velocity steadily increases down the tube reaching sonic conditions at the reactor exit.[69] Subsequently, the pyrolytically generated species are expanded into the vacuum chamber as a seeded supersonic jet resulting in isolated radicals under cold and collision-free conditions.[68] By varying several parameters such as the length of the heated region, backing gas pressure, precursor concentration, and pyrolysis temperature, the conditions in the microreactor can further be systematically adjusted to promote bimolecular reactions, which facilitates the formation of high-temperature reaction products.

The efficiency of (flash) pyrolysis further strongly depends on the chosen precursor as the desired intermediates are formed by homolytically cleaving the weakest bond in the gas-phase. Therefore, halohydrocarbons such as bromide or iodide derivatives are commonly chosen that generally exhibit relatively weak carbon-halogen bond dissociation energies (around 290 $kJ \cdot mol^{-1}$ for C−Br and 220 $kJ \cdot mol^{-1}$ for C−I, respectively).[75] In addition, nitrites[67] or highly-strained hydrocarbons[76] often allow for a clean generation of radicals at moderate pyrolysis conditions. As the spectroscopy is performed in the gas-phase and thus requires a sufficiently high molecule density, suitable precursors further need to exhibit a high vapor pressure. In addition, they must be thermally stable up to temperatures of around 500 K, as they are frequently heated to increase their molecular concentration in the gas-phase.

2.2.2 Molecular Beam Technique

For an accurate spectroscopic investigation in the gas-phase, the molecules of interest ideally should (i) be in a specific and well-defined quantum state (typically the lowest energy state), (ii) move with a narrow velocity distribution, and (iii) be diluted to a sufficiently low number density to exclude intermolecular interactions.[78] These properties are achieved to a large degree in a supersonic expansion

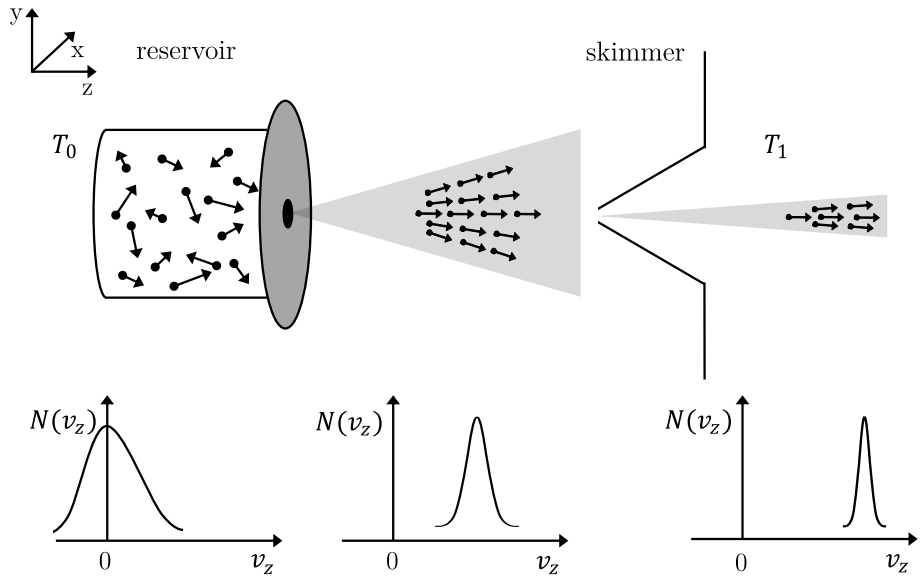

Figure 2.8. Schematic diagram of a free jet expansion.[77] Internal energy of the gas sample is transferred into a directed gas flow by several collisions resulting in a free jet travelling at several hundred metres per second with a narrow velocity distribution.[71,78]

of the sample molecules which are seeded in an inert carrier gas such as argon or helium.[78]

A free jet is established by expanding a high-pressure gas sample into a low-pressure downstream region through a small nozzle orifice.[71] The molecular motion in the gas reservoir behind the nozzle is random with a velocity distribution represented by the velocity-weighted Maxwell-Boltzmann distribution $N(v_z)$ at the equilibrium reservoir temperature T_0.[71,78] At sufficiently high pressures, the diameter of the orifice D is significantly larger than the molecular mean free path $\overline{\lambda}$ between collisions ($D \gg \overline{\lambda}$).[78] This results in several collisions close to the orifice, leading to molecules with a prevailing velocity component in the downstream direction (defined as the z-axis in this section).[71] Hence, random thermal motion is converted to directed motion as indicated in Figure 2.8.[77] The gas sample with an originally wide velocity distribution and an average moving speed of zero is transformed into a jet with a narrow velocity distribution moving at a significantly higher speed in the range of several hundred metres per second.[79] The conversion causes the sample temperature to decrease as internal energy of the gas is transferred into the directed flow velocity,[71] which is known as translational cooling. Minimal temperatures are reached in a supersonic expansion of a noble gas as it behaves closely to an ideal gas and does not possess vibrational and rotational degrees of freedom. The corresponding terminal velocity $\overline{v_z}$ as a function of the final translational temperature of the jet $T_1 (\ll T_0)$ is given by[79]

$$\overline{v_z} = \sqrt{\frac{2k_B(T_0 - T_1)}{M_{mol}} \cdot \frac{\gamma}{\gamma - 1}} \,, \tag{2.5}$$

where $\gamma = c_p/c_v$ is the specific heat ratio and M_{mol} denotes the molecular mass.

By seeding a polyatomic molecule in a noble gas at sufficiently low concentrations, almost all collisions of the molecule occur with the seed gas. Hence, the molecular sample is accelerated in the same direction as the seed gas atoms resulting in translational temperatures similar to that of the carrier gas.[17,71] Once an equilibrium of the velocities of the seed gas atoms and the sample molecules is reached, only low energy collisions occur which decreases the vibrational and rotational temperatures of the molecules.[71] As the expansion further proceeds in the downstream region, the gas density and hence the probability of collisions decrease.[77] At about a distance of roughly 20−30 orifice diameters D from the nozzle the molecular temperature asymptotically reaches its minimal value.[49] The central part of the jet is selected by a conically shaped skimmer[80,81] with an aperture diameter of 1−2 mm to subtract sample molecules with a consid-

erable transversal velocity component, see Figure 2.8.[79] Subsequently, isolated sample molecules with translational temperatures of less than 2 K[71,82] and rotational temperatures of about 1−10 K[71,77,83] can be studied. However, vibrational cooling is less effective[84,85] due to smaller depopulation collisional cross sections providing temperatures in the range of 50−150 K.[71] In the high-temperature pyrolysis experiments performed in the research of this thesis, vibrational cooling to about room temperature was estimated.[86]

Maintaining a large pressure gradient between the reservoir and the downstream region places high demands on the pumping system.[77] Hence, supersonic sources are often operated in a pulsed mode using a solenoid valve to generate beam pulses with a duration of around 100 μs.[79] This allows to reduce the total gas load on the vacuum pumps and provides additional cooling due to an increased pressure gradient.[79]

2.2.3 Time-of-Flight Mass Spectrometry

The separation of ions in a TOF mass spectrometer is based on the difference between the velocities of the ions with different mass-to-charge ratios (m/z). Hence, they take different flight times to travel through a given path.[87] The main advantages of TOF mass analyzers include a relatively high mass resolution, a virtually unlimited mass range, and the simplicity of their design.[88] The latter facilitates an easy handling, ruggedness, and a straightforward combination with several other techniques such as EI,[2] MALDI,[1] or PI.[4]

The most basic TOF setups consist of an ion source, an acceleration region with a homogeneous electric field E, and a field-free drift space with a subsequent ion detector.[88] In the research of this thesis a TOF mass spectrometer following the design of Wiley and McLaren[89] was employed. Here, the acceleration region is separated into two zones of different electric field strength.[17,89] This approach adds an additional freely adjustable parameter (the extractor voltage U_e) resulting in a tight ion package compression at the surface of the ion detector and hence a high mass resolution.[88] The ions, produced at a well-defined time and position between two electrostatic plates (repeller/extractor), are accelerated to the same kinetic energy into a field-free flight tube of length L and detected by microchannel plates (MCP) to monitor the ion flight time t_{flight}.[17] The latter is related to the mass-to-charge ratio of the ion according to[17]

$$t_{flight} = \frac{L}{v} = L\sqrt{\frac{m}{2z(rE_r + eE_e)}}\ , \tag{2.6}$$

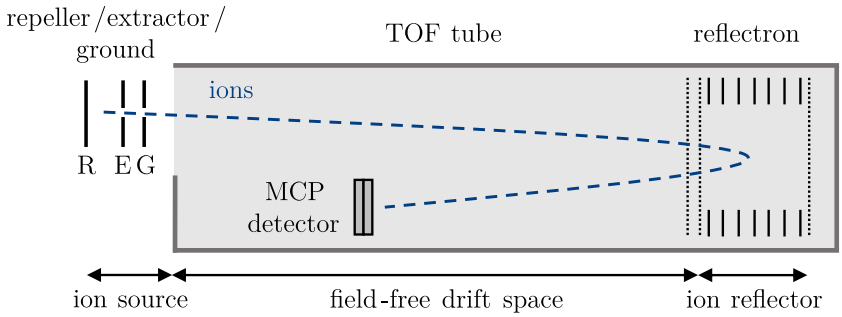

Figure 2.9. Scheme of a TOF tube equipped with a reflectron to enhance the mass resolution.

where v denotes the velocity of the ion with a mass-to-charge ratio m/z, and E_r and E_e are the electric potential differences between repeller/extractor and extractor/ground plate, respectively. The length between the ionization region and the extractor plate is represented by r, whereas the distance between the extractor and ground plate is given by e.[17]

In an ideal setup, the ions are generated exactly half-way between the repeller and extractor plates. In reality, the molecules are ionized at slightly different positions relative to the extractor plate, which results in different velocities even for ions with the same mass-to-charge ratio. Consequently, the ions will take slightly different flight times leading to broader mass signals in the TOF mass spectrum.[49] To increase the resolution, a reflectron (electrostatic ion mirror) is commonly employed at the end of the drift region,[87] see Figure 2.9. This unit consists of a series of ring electrodes with increasing voltages which generate retarding fields.[17] In this way, the spread of flight times of the ions with the same m/z is significantly diminished, as ions with higher kinetic energy penetrate more deeply into the ion mirror which extents the time until they are reflected.[87,88] Consequently, they hit the detector at almost the same time. Additionally, reflectrons increase (and almost double) the flight path, see Figure 2.9, which further substantially enhances the mass resolution.[17]

Experimental setup

In the following, the experimental setup used to perform the IR/UV-IDS experiments at the Free Electron Laser for Infrared eXperiments (FELIX) laboratory[20] at the Radboud University, Nijmegen, The Netherlands, is briefly described. An in-depth description is given in the literature.[17] The instrument consists of an in-vacuum molecular beam source,[90] a differentially pumped vacuum apparatus,[17] a reflectron TOF mass spectrometer, as well as UV and IR laser systems. The

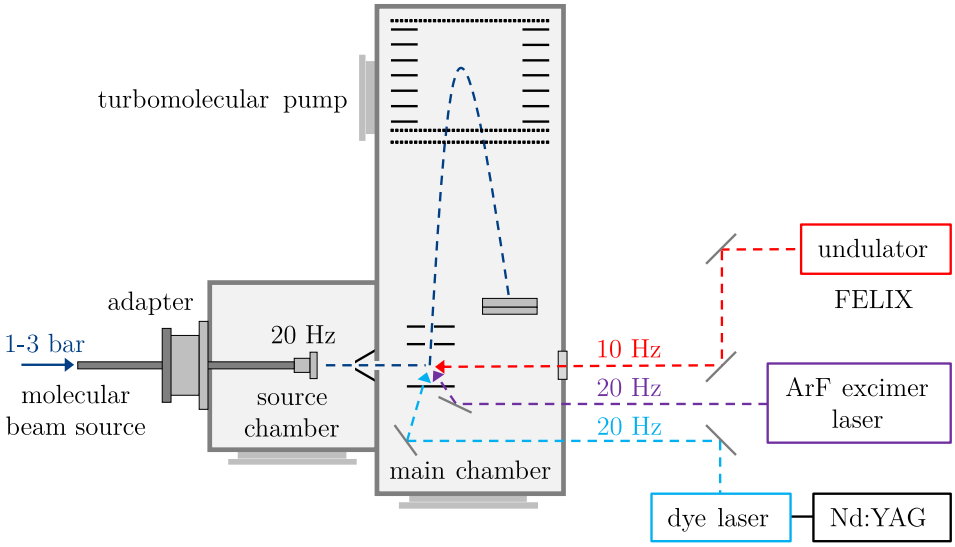

Figure 2.10. Schematic representation of the experimental setup utilized in the research of this thesis.

molecular beam source (operated at 20 Hz) was mounted onto the source chamber (10^{-6} mbar) of the vacuum apparatus *via* a home-built adapter producing a free molecular jet as shown in Figure 2.10. Subsequently, the supersonically cooled molecules were skimmed and delivered into the main chamber ($10^{-7} - 10^{-8}$ mbar) of a reflectron TOF mass spectrometer (resolution $m/\Delta m$=2800-3000, *R. M. Jordan Co.*).[49] Here, the free jet interacted with two perpendicular UV lasers beams and counterpropargating FEL-IR radiation. Excitation was provided by a tunable dye laser (LiopStar, *LiopTec*) pumped by a frequency doubled (532 nm) or tripled (355 nm) Nd:YAG laser (Pro-290-20-Hz, *Spectra Physics*, Spitlight 1200, *Innolas*). Ionization was accomplished by using a 193 nm ArF excimer laser (20 Hz, *Neweks*) to perform two-color [1+1']-REMPI. The scannable IR radiation in the FIR and MIR region was provided by the free-electron-laser FELIX.[20] The FEL was set around 200 ns prior to the UV radiation and operated at half the repetition rate of the UV lasers to perform IR/UV-IDS. Generally, FELIX (10 μs pulse) exhibits a bandwidth of around 1 % of the central photon frequency with pulse energies ranging from 25 mJ for the FIR up to 200 mJ for the MIR region.[20] A more detailed overview of selected specifications of FELIX is given in Table 2.1.

2.2.4 Intense and Tunable IR Light Sources

When tunability is not relevant but high power and photon fluence are required, commercially available CO_2 lasers are the laser systems of choice.[91] They can

achieve very high continuous-wave power levels of up to 100 W with emission bands centred around 9.6 and 10.6 μm (1042 and 944 cm^{-1}).[17] Such light sources are ideal to perform IR multiphoton excitation (IR-MPE) and IR multiphoton dissociation (IR-MPD) experiments on gas-phase molecules.[92] In contrast, IR/UV-IDS relies not only on the use of high-intense but also tunable IR light sources that cover a wide IR photon range. While OPO/OPA laser systems allow to scan roughly between 2200 and 4500 cm^{-1},[17] FEL facilitate the investigation of low-frequency vibrations in the FIR and fingerprint region at high intensity.[20] Both laser systems have been utilized in the research of this thesis and thus are presented in the following section in more detail.

Free electron laser

For conventional lasers, atoms or molecules in the gas-, liquid-, or condensed phase are employed as the gain medium which limits the emitted photon energy range due to absorption.[91] In contrast, free electrons moving at relativistic speeds serve as the lasing medium in a FEL to generate coherent and highly brilliant radiation.[20]

The general principle of a typical FEL is shown in Figure 2.11. A relativistic beam of electrons, generated by an electron gun and accelerator, is injected into an assembly of alternating permanent magnets, called undulator.[91] The magnetic field of the undulator is perpendicular to the direction of the electron beam, causing a periodic deflection, a "wiggling" motion, of the electrons while crossing the undulator.[91] The transverse acceleration along the sinusoidal trajectory results in the emission of dipole radiation that is captured in a laser cavity consisting of two high-reflectivity mirrors at opposite sides of the undulator,[20] see Figure 2.11.

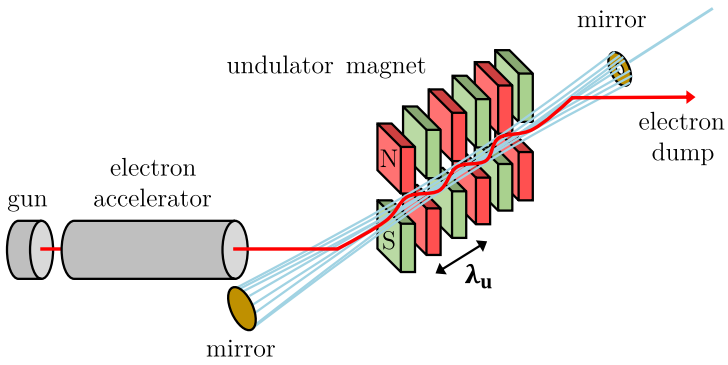

Figure 2.11. Generic layout of a free electron laser. FEL radiation is generated by a beam of relativistic electrons (red curve) injected into an undulator. Adapted with permission from Ref. [20]. Copyright 1995 American Chemical Society.

This radiation is in general very weak and incoherent as the spontaneous emission from randomly distributed electrons interferes constructively as well as destructively while traversing the undulator.[91] Gradually, a standing wave is formed inside the optical cavity (illustrated in blue in Figure 2.11) causing freshly injected electrons to interact with the transverse electric field of the radiation.[20] Consequently, some electrons gain while others lose energy to the optical field due to ponderomotive forces, inducing a bunching of the electrons (called *microbunching*).[20] These bunches behave similarly to a single particle resulting in coherently emitted radiation with a successively growing intensity (gain) until a saturated power level is reached that is typically $10^7 - 10^8$ times higher than that of the initial undulator radiation.[91] A fraction of the generated FEL radiation leaves the cavity through a central hole in one of the end mirrors with an output wavelength λ_{FEL} that is given by the FEL resonance condition[20]

$$\lambda_{FEL} = \frac{\lambda_u}{2\gamma^2} \cdot (1 + K^2) \quad \text{with} \quad \gamma = \frac{1}{\sqrt{1 - (\frac{v}{c})^2}}, \tag{2.7}$$

where λ_u denotes the distance between two magnets with the same polarity (see Figure 2.11) called undulator period, K is a dimensionless parameter that is proportional to the magnetic field strength,[20] and γ represents the relativistic Lorentz factor, which is a measure for the total electron energy.[91] Eq. (2.7) comprises two effects, the Lorentz contraction and the Doppler effect, that both shorten the undulator by γ as represented by $\lambda_u/(2\gamma^2)$.[91] The term $(1 + K^2)$ takes account of the longer travel distance of the electrons in comparison with the light beam due to their transverse motion induced by the magnetic field.[91] The formula demonstrates that the output wavelength λ_{FEL} depends on three macroscopic parameters (γ, λ_u, and K) and is not determined by microscopic properties of atoms or molecules.[20] Hence, FEL can in principle produce radiation for any desired wavelength region, which is, in practice, only constrained by technical limitations.[91] As the undulator period λ_u generally is fixed, λ_{FEL} is tuned continuously *via* the magnetic field strength (K) by changing the distance between the two rows of magnets in the undulator.[20] This facilitates a wavelength tuning range over a factor of about three for a given beam energy setting.[17] Larger wavelength changes are obtained by adjusting the electron beam energy (γ).[20]

Free Electron Laser for Infrared eXperiments (FELIX)

The FELIX free electron laser laboratory comprises the four lasers FELIX-1 (30−150 μm), FELIX-2 (3−45 μm), FELICE (5−100 μm) and FLARE (100−1500 μm),

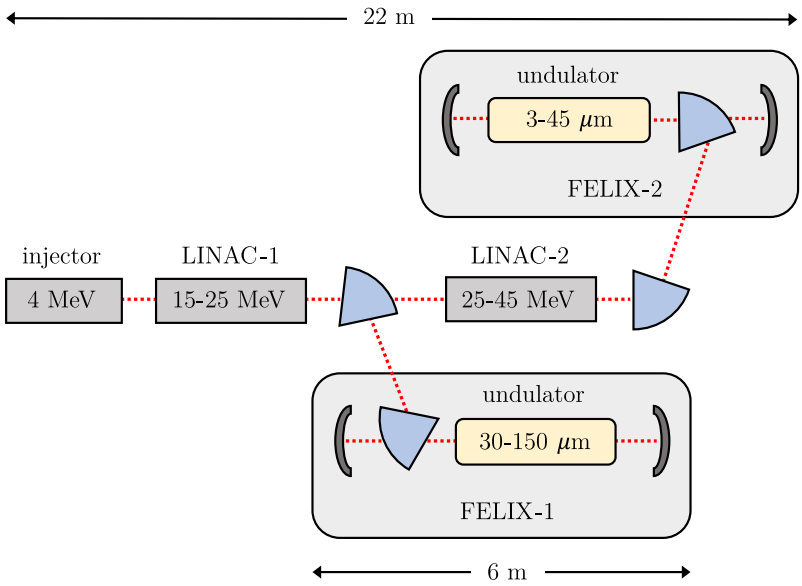

Figure 2.12. Schematic representation of the two lasers FELIX-1 and FELIX-2 at the FELIX free electron laser laboratory. Adapted with permission from Ref. [20]. Copyright 1995 American Chemical Society.

providing a wide range of wavelengths for the excitation of molecules and clusters to (mostly) study their ground state properties. In the research of this thesis, experiments were performed in the FIR and MIR region using the wavelength region of FELIX-1 and FELIX-2. A schematic layout of the two lasers is given in Figure 2.12. A thermionic triode electron gun operated at 1 GHz and followed by a 1 GHz prebuncher and 3 GHz buncher generates a pulsed 3.8 MeV electron beam which is further accelerated in two 3-GHz travelling-wave radio-frequency linear

Table 2.1. Selected specifications of FELIX-1 and FELIX-2.

parameter		FELIX
spectral range	/μm	2.7−150
	/cm^{-1}	3600−66
micropulse rep. rate	/MHz	25, 50, or 1000
micropulse energy	/μJ	<40
macropulse rep. rate	/Hz	<10
macropulse energy	/mJ	<200
macropulse stability[20]	[%]	1−2 (r.m.s)
bandwidth (FWHM)	[%]	0.4−5
polarization (linear)	[%]	>95

accelerators (LINAC). Here, an electron beam with energies of 15−25 MeV and 25−45 MeV is obtained that is bent into FELIX-1 for the long wavelength range or FELIX-2 for the short wavelength region.[20] The two FEL are equipped with an identical undulator that is an assembly of two rows of samarium-cobalt permanent magnets forming 38 field periods with $\lambda_u = 65$ mm. The FEL resonator is established by two gold-plated copper mirrors leading to a cavity length of 6 m.[20] A small portion of the FEL radiation is coupled out, collimated by a spherical mirror, and delivered to the user stations *via* an evacuated mirror-based beam transport system.[20] Selected specifications of FELIX-1 and FELIX-2 are given in Table 2.1.

OPO/OPA laser system

An OPO/OPA laser system is a commercially available coherent MIR light source that is based on nonlinear optical frequency conversion.[93] In the research of this thesis, an OPO/OPA system by *LaserVision* was utilized which produced tunable IR radiation in the 3 μm region (bandwidth <0.1 cm^{-1}) with pulse energies exceeding 10 mJ in a roughly 6 ns pulse.[17,49] A schematic outline of the system is given in Figure 2.13.

The fundamental of a pulsed Nd:YAG laser (1064 nm) is split into two beams, whereby one of the two is frequency-doubled (532 nm) in a potassium dideuterium phosphate (KDP) crystal.[49] Subsequently, the 532 nm beam (called *pump*) is injected into an optical parametric oscillation (OPO) source consisting of two potassium titanyl phosphate (KTP) crystals.[49] Here, the pump is converted into two output wavelengths, called *signal* and *idler*, at around 800 and 1600 nm by second-order nonlinear optical effects,[17] where the higher energetic beam is referred to as the signal. The sum of the two output photon energies is equal to the pump photon energy according to the law of energy conservation[93]

$$h\nu_{pump} = h\nu_{signal} + h\nu_{idler}, \tag{2.8}$$

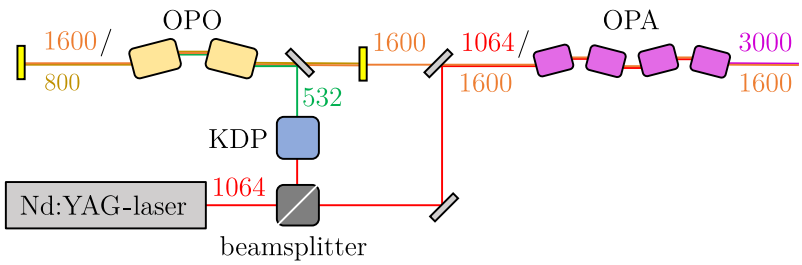

Figure 2.13. Schematic outline of the *LaserVision* OPO/OPA laser system.[17]

where h is Planck's constant. In addition, the conservation of momentum has to be fulfilled which is often referred to as *phase-matching* in nonlinear optics.[93] The idler beam (1600 nm) as well as the split 1064 nm beam is then directed into an optical parametric amplifier (OPA) stage consisting of four potassium titanyl arsenate (KTA) crystals.[49] Parametric amplification of the 1600 nm and parametric downconversion of the 1064 nm beam results in the generation of a second idler beam in the 3 μm region which is coupled out and used in the experiment.[17] By simultaneously varying the angles of the nonlinear crystals in the OPO and OPA stages, different output wavelengths are produced allowing to scan approximately between 2200 and 4500 cm^{-1} at moderate pulse energies.[17] For larger tuning ranges to around 1000 cm^{-1} or beyond, difference frequency generation (DFG) can be applied using an additional nonlinear crystal ($AgGaSe_2$).[93] However, this results in pulse energies below 1 mJ that is typically too low to investigate low-frequency vibrations with small IR absorption cross sections.[17,49]

2.3 Computation of Molecular Vibrations

Generally, the assignment of vibrational spectra is based on the calculation of molecular vibrational properties using computational quantum chemistry.[94] Today, such calculations are common practice for both experimentalists and theoreticians.[95] The vast majority of these computations are performed in the harmonic approximation, in which the potential energy surface (PES)[17] around the equilibrium structure of a molecule is approximated by a truncated, second-order Taylor series.[94] This approach allows to derive a general picture of the vibrational structure of the molecule.[95] However, anharmonic effects are not considered when higher-order terms are neglected in the Taylor expansion, leading to deviations of the predicted frequencies in comparison with the experimentally observed frequencies.[94] In general, the error in the harmonic approximation model is fairly systematic which results in predicted wavenumbers that are larger than the experimental ones.[95] A schematic representation of the deviation of the wavenumber of a vibrational mode ν_{calc} computed at various levels of theory using DFT[96] is given in Figure 2.14.[97] While the range of uncertainty ($\nu_{exp} - \nu_{calc}$) about the real experimentally observed value ν_{exp} is high at low levels of theory, it significantly decreases and finally approaches a convergence limit for higher theoretical levels.[97] Although the latter still differs from zero ($\nu_{exp} \neq \nu_{calc}$), it is fairly comparable for different molecules at a given level of theory.[97] This has led to multiplicative scaling of the harmonic frequencies which has shown to provide accurately predicted wavenumbers and thus accounts for anharmonic effects.[95] Generally, the

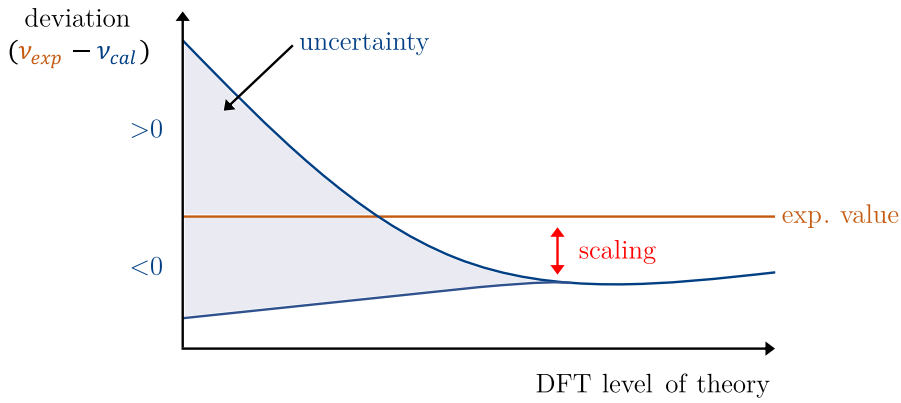

Figure 2.14. Schematic of the deviation of the calculated wavenumber of a vibrational mode from the experimental value as a function of the chosen level of theory using DFT. Adapted with permission from Ref. [97].

value of the scaling factor is determined empirically and has been benchmarked for various theoretical models in several studies.[98,99] While it is still common practice to scale all frequencies with a single empirical factor,[94] low and high frequency vibrational modes require slightly different scaling factors for a more accurate correction.[100,101] However, the main drawback of using multiple scaling factors is an increased level of empiricism and a more difficult transferability to other systems.[95]

Another way to improve the accuracy of the predicted frequencies is to introduce higher-order terms in the Taylor series which facilitates a more precise description of the PES of the molecule in comparison with the harmonic approximation model.[94] When combined with high-level potential energy functions, this anharmonic approach allows to compute vibrational frequencies at near-spectroscopic accuracy.[94] However, anharmonic computations require significantly higher computational costs than harmonic calculations which often is too inconvenient and time consuming for practical applications in research.[95] For example, the relative computation times of anharmonic and harmonic frequencies of fundamental molecular vibrations of formaldehyde (CH_2O) are depicted in Figure 2.15 using various low-level *ab initio* methods (Hartree-Fock (HF), second-order perturbation (MP2), and hybrid B3LYP (DFT), all combined with the 6-31+G(d,p) basis set).[94] The figure was adapted with permission from Ref. [94]. Even for such a small molecule and at moderate levels of theory, the computational time for anharmonic calculations is about ten times higher than for the harmonic approaches.[94] To classify the merit of applying higher computational costs for anharmonic calculations, the predicted harmonic and anharmonic frequencies for CH_2O were compared with

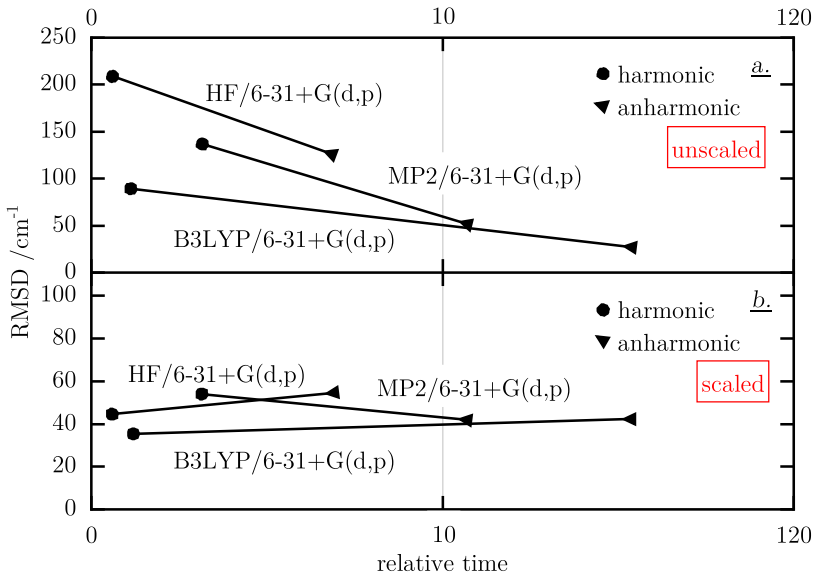

Figure 2.15. Root-mean-square deviation (RMSD) as a measure for the performance of unscaled (trace a) and scaled (b) harmonic (circle) and anharmonic (triangle) frequency computations for formaldehyde using various low-level methods plotted against the relative computational time. Adapted with permission from Ref. [94].

the experimentally observed values. Therefore, the root-mean-square deviation (RMSD) was determined as a statistical measure for each set of computed frequencies with respect to the experimental values.[94] As shown in Figure 2.15b, the anharmonic approaches provide more accurate frequencies for CH_2O when empirical scaling is not applied. However, scaled harmonic and scaled anharmonic calculations yield frequencies of comparable accuracy (trace b), showing that the computational cost of anharmonic calculations does not provide an advantage at the chosen level of theories.[94] This trend has been further investigated in a study by Jacobsen *et al.*[94] who examined a large set of 176 molecules with up to 2738 vibrational modes, showing that scaled anharmonic computations do not lead to more accurate frequency predictions than scaled harmonic predictions at moderate level of theories albeit at much higher computational expenses. A significant benefit from anharmonic calculations is generally only obtained when combined with very high-level theoretical methods.[94]

In this thesis, all computations were performed using the harmonic approach. Empirical scaling of the predicted frequencies was applied in all studies with empirical factors, that are in the range of values recommended by previous benchmark studies.

References

[1] M. Karas, F. Hillenkamp, *Adv. Mass Spectrom.* **1989**, 416–417.

[2] E. V. S. Maciel, N. G. Pereira dos Santos, D. A. Vargas Medina, F. M. Lanças, *Electrophoresis* **2022**, *43*, 1587–1600.

[3] P. T. Lynch, T. P. Troy, M. Ahmed, R. S. Tranter, *Anal. Chem.* **2015**, *87*, 2345–2352.

[4] L. Hanley, R. Zimmermann, *Anal. Chem.* **2009**, *81*, 4174–4182.

[5] J. B. Pallix, U. Schühle, C. H. Becker, D. L. Huestis, *Anal. Chem.* **1989**, *61*, 805–811.

[6] U. Boesl, *J. Phys. Chem.* **1991**, *95*, 2949–2962.

[7] R. Zimmermann, W. Welthagen, T. Gröger, *J. Chrom. A* **2008**, *1184*, 296–308.

[8] P. Misra, M. A. Dubinskii, *Ultraviolet Spectroscopy and UV Lasers*, Marcel Dekker, New York, **2002**.

[9] F. Mühlberger, K. Hafner, S. Kaesdorf, T. Ferge, R. Zimmermann, *Anal. Chem.* **2004**, *76*, 6753–6764.

[10] F. Qi, R. Yang, B. Yang, C. Huang, L. Wei, J. Wang, L. Sheng, Y. Zhang, *Rev. Sci. Instrum.* **2006**, *77*, 084101.

[11] F. Zhang, R. I. Kaiser, V. V. Kislov, A. M. Mebel, A. Golan, M. Ahmed, *J. Phys. Chem. Lett.* **2011**, *2*, 1731–1735.

[12] T. Baer, R. P. Tuckett, *Phys. Chem. Chem. Phys.* **2017**, *19*, 9698–9723.

[13] I. Fischer, S. T. Pratt, *Phys. Chem. Chem. Phys.* **2022**, *24*, 1944–1959.

[14] P. Hemberger, A. Bodi, *Chimia* **2018**, *72*, 227–227.

[15] M. N. McCabe, P. Hemberger, E. Reusch, A. Bodi, J. Bouwman, *J. Phys. Chem. Lett.* **2020**, *11*, 2859–2863.

[16] P. Hemberger, A. J. Trevitt, T. Gerber, E. Ross, G. da Silva, *J. Phys. Chem. A* **2014**, *118*, 3593–3604.

[17] A. M. Rijs, J. Oomens, *Top. Curr. Chem.* **2014**, *364*, 1–42.

[18] W. Y. Sohn, S.-i. Ishiuchi, M. Miyazaki, J. Kang, S. Lee, A. Min, M. Y. Choi, H. Kang, M. Fujii, *Phys. Chem. Chem. Phys.* **2012**, *15*, 957–964.

[19] C.-H. Zhang, G.-H. Sha, *Science* **1993**, *262*, 374–375.

[20] D. Oepts, A. F. G. van der Meer, P. W. van Amersfoort, *Infrared Phys. Technol.* **1995**, *36*, 297–308.

[21] S. Bakels, M.-P. Gaigeot, A. M. Rijs, *Chem. Rev.* **2020**, *120*, 3233–3260.

[22] S. Jaeqx, J. Oomens, A. Cimas, M.-P. Gaigeot, A. M. Rijs, *Angew. Chem. Int. Ed.* **2014**, *53*, 3663–3666.

[23] A. K. Lemmens, P. Chopra, D. Garg, A. L. Steber, M. Schnell, W. J. Buma, A. M. Rijs, *Mol. Phys.* **2021**, *119*, e1811908.

[24] A. K. Lemmens, S. Gruet, A. L. Steber, J. Antony, S. Grimme, M. Schnell, A. M. Rijs, *Phys. Chem. Chem. Phys.* **2019**, *21*, 3414–3422.

[25] R. G. Satink, G. Meijer, G. von Helden, *J. Am. Chem. Soc.* **2003**, *125*, 15714–15715.

[26] F. Hirsch, I. Fischer, S. Bakels, A. M. Rijs, *J. Phys. Chem. A* **2022**, *126*, 2532–2540.

[27] K. H. Fischer, J. Herterich, I. Fischer, S. Jaeqx, A. M. Rijs, *J. Phys. Chem. A* **2012**, *116*, 8515–8522.

[28] T. A. Carlson, *Annu. Rev. Phys. Chem.* **1975**, *26*, 211–234.

[29] B. V. King, M. J. Pellin, J. F. Moore, I. V. Veryovkin, M. R. Savina, C. E. Tripa, *Appl. Surf. Sci.* **2003**, *203-204*, 244–247.

[30] F. Mühlberger, T. Streibel, J. Wieser, A. Ulrich, R. Zimmermann, *Anal. Chem.* **2005**, *77*, 7408–7414.

[31] G. Bjorklund, *IEEE J. Quantum Electron.* **1975**, *11*, 287–296.

[32] P. D. Maker, R. W. Terhune, *Phys. Rev.* **1965**, *137*, 801–818.

[33] L. Hanley, O. Kornienko, E. T. Ada, E. Fuoco, J. L. Trevor, *J. Mass Spectrom.* **1999**, *34*, 705–723.

[34] T. Adam, R. Zimmermann, *Anal. Bioanal. Chem.* **2007**, *389*, 1941–1951.

[35] T. A. Cool, J. Wang, K. Nakajima, C. A. Taatjes, A. Mcllroy, *Int. J. Mass Spectrom.* **2005**, *247*, 18–27.

[36] B. Yang, J. Wang, T. A. Cool, N. Hansen, S. Skeen, D. L. Osborn, *Int. J. Mass Spectrom.* **2012**, *309*, 118–128.

[37] A. Hamachi, T. Okuno, T. Imasaka, Y. Kida, T. Imasaka, *Anal. Chem.* **2015**, *87*, 3027–3031.

[38] O. P. Haefliger, R. Zenobi, *Anal. Chem.* **1998**, *70*, 2660–2665.

[39] A. Li, T. Uchimura, H. Tsukatani, T. Imasaka, *Anal. Sci.* **2010**, *26*, 841–846.

[40] Y. Li, L. Zhang, Z. Tian, T. Yuan, J. Wang, B. Yang, F. Qi, *Energy Fuels* **2009**, *23*, 1473–1485.

[41] U. Boesl, A. Bornschlegl, C. Logé, K. Titze, *Anal. Bioanal. Chem.* **2013**, *405*, 6913–6924.

[42] D. S. Zakheim, P. M. Johnson, *Chem. Phys.* **1980**, *46*, 263–272.

[43] H.-H. Schmidtke in *Electronic and Vibronic Spectra of Transition Metal Complexes I*, Springer, Berlin, Heidelberg, **1994**, pp. 69–111.

[44] M. Rey, I. S. Chizhmakova, A. V. Nikitin, V. G. Tyuterev, *Phys. Chem. Chem. Phys.* **2018**, *20*, 21008–21033.

[45] D. F. Swinehart, *J. Chem. Educ.* **1962**, *39*, 333.

[46] T. Häber, U. Schmitt, M. A. Suhm, *Phys. Chem. Chem. Phys.* **1999**, *1*, 5573–5582.

[47] A. P. Milce, D. E. Heard, R. E. Miller, B. J. Orr, *Chem. Phys. Lett.* **1996**, *250*, 95–103.

[48] R. H. Page, Y. R. Shen, Y. T. Lee, *J. Chem. Phys.* **1988**, *88*, 5362–5376.

[49] S. Bakels, PhD thesis, Radboud University, Nijmegen, The Netherlands, **2022**.

[50] A. K. Lemmens, D. B. Rap, J. M. M. Thunnissen, S. Gruet, A. L. Steber, S. Panchagnula, A. G. G. M. Tielens, M. Schnell, W. J. Buma, A. M. Rijs, *J. Phys. Chem. Lett.* **2020**, *11*, 8997–9002.

[51] S. Ghosh, M. K. Dixit, S. P. Bhattacharyya, B. L. Tembe, *J. Chem. Educ.* **2013**, *90*, 1463–1471.

[52] N. S. Nagornova, T. R. Rizzo, O. V. Boyarkin, *Angew. Chem. Int. Ed.* **2013**, *52*, 6002–6005.

[53] A. M. Rijs, I. Compagnon, J. Oomens, J. S. Hannam, D. A. Leigh, W. J. Buma, *J. Am. Chem. Soc.* **2009**, *131*, 2428–2429.

[54] J. Oomens, B. G. Sartakov, G. Meijer, G. von Helden, *Int. J. Mass Spectrom.* **2006**, *254*, 1–19.

[55] R. A. Coveleskie, D. A. Dolson, C. S. Parmenter, *J. Chem. Phys.* **1980**, *72*, 5774–5775.

[56] M. Schmitt, F. Spiering, V. Zhaunerchyk, R. T. Jongma, S. Jaeqx, A. M. Rijs, W. J. v. d. Zande, *Phys. Chem. Chem. Phys.* **2016**, *18*, 32116–32124.

[57] L. Oudejans, A. Touati, B. K. Gullett, *Anal. Chem.* **2004**, *76*, 2517–2524.

[58] H. Fricke, A. Funk, T. Schrader, M. Gerhards, *J. Am. Chem. Soc.* **2008**, *130*, 4692–4698.

[59] A. M. Rijs, M. Kabeláč, A. Abo-Riziq, P. Hobza, M. S. de Vries, *ChemPhysChem* **2011**, *12*, 1816–1821.

[60] A. M. Rijs, G. Ohanessian, J. Oomens, G. Meijer, G. von Helden, I. Compagnon, *Angew. Chem. Int. Ed.* **2010**, *49*, 2332–2335.

[61] Y. Carpentier, T. Pino, P. Bréchignac, *J. Phys. Chem. A* **2013**, *117*, 10092–10104.

[62] D. S. N. Parker, R. I. Kaiser, B. Bandyopadhyay, O. Kostko, T. P. Troy, M. Ahmed, *Angew. Chem. Int. Ed.* **2015**, *54*, 5421–5424.

[63] T. Baer, *Int. J. Mass Spectrom.* **2000**, *200*, 443–457.

[64] M. Gerlach, S. Monninger, D. Schleier, P. Hemberger, J. T. Goettel, H. Braunschweig, I. Fischer, *ChemPhysChem* **2021**, *22*, 2164–2167.

[65] J. E. Rink, U. Boesl, *Eur. J. Mass Spectrom.* **2003**, *9*, 23–32.

[66] X. Miao, T. Preitschopf, F. Sturm, I. Fischer, A. K. Lemmens, M. Limbacher, R. Mitric, *J. Phys. Chem. Lett.* **2022**, 8939–8944.

[67] T. Preitschopf, F. Hirsch, A. K. Lemmens, A. M. Rijs, I. Fischer, *Phys. Chem. Chem. Phys.* **2022**, *24*, 7682–7690.

[68] D. W. Kohn, H. Clauberg, P. Chen, *Rev. Sci. Instrum.* **1992**, *63*, 4003–4005.

[69] Q. Guan, K. N. Urness, T. K. Ormond, D. E. David, G. Barney Ellison, J. W. Daily, *Int. Rev. Phys. Chem.* **2014**, *33*, 447–487.

[70] X. Zhang, A. V. Friderichsen, S. Nandi, G. B. Ellison, D. E. David, J. T. McKinnon, T. G. Lindeman, D. C. Dayton, M. R. Nimlos, *Rev. Sci. Instrum.* **2003**, *74*, 3077–3086.

[71] M. V. Johnston, *Trends Analyt. Chem.* **1984**, *3*, 58–61.

[72] B. Penetrante, M. Hsiao, B. Merritt, G. Vogtlin, P. Wallman, *IEEE Trans. Plasma Sci.* **1995**, *23*, 679–687.

[73] I. R. Slagle, J. Y. Park, M. C. Heaven, D. Gutman, *J. Am. Chem. Soc.* **1984**, *106*, 4356–4361.

[74] C. Alcaraz, I. Fischer, D. Schröder in *Encyclopedia of Radicals in Chemistry, Biology and Materials*, John Wiley & Sons, Ltd, **2012**.

[75] C. M. Nichols, Z. Yang, B. B. Worker, D. R. Hager, N. M. M. Nibbering, V. M. Bierbaum, *Phys. Chem. Chem. Phys.* **2012**, *15*, 561–567.

[76] F. Hirsch, K. Pachner, I. Fischer, K. Issler, J. Petersen, R. Mitric, S. Bakels, A. M. Rijs, *ChemPhysChem* **2020**, *21*, 1515–1518.

[77] T. A. Miller, *Science* **1984**, *223*, 545–553.

[78] R. E. Smalley, L. Wharton, D. H. Levy, *Acc. Chem. Res.* **1977**, *10*, 139–145.

[79] T. E. Wall, *J. Phys. B: At. Mol. Opt. Phys.* **2016**, *49*, 243001.

[80] S. D. Eder, A. Salvador Palau, T. Kaltenbacher, G. Bracco, B. Holst, *Rev. Sci. Instrum.* **2018**, *89*, 113301.

[81] W. R. Gentry, C. F. Giese, *Rev. Sci. Instrum.* **1975**, *46*, 104–104.

[82] D. H. Levy, *Annu. Rev. Phys. Chem.* **1980**, *31*, 197–225.

[83] G. Meijer, M. S. de Vries, H. E. Hunziker, H. R. Wendt, *Appl. Phys. B* **1990**, *51*, 395–403.

[84] H. G. Bennewitz, G. Buess, *Chem. Phys.* **1978**, *28*, 175–185.

[85] G. M. McClelland, K. L. Saenger, J. J. Valentini, D. R. Herschbach, *J. Phys. Chem.* **1979**, *83*, 947–959.

[86] T. Preitschopf, F. Sturm, I. Stroganova, A. K. Lemmens, A. M. Rijs, I. Fischer, *Chem. Euro. J.* **2023**, *29*, e202202943.

[87] B. A. Mamyrin, *Int. J. Mass Spectrom.* **2001**, *206*, 251–266.

[88] U. Boesl, *Mass Spectrom. Rev.* **2017**, *36*, 86–109.

[89] W. C. Wiley, I. H. McLaren, *Rev. Sci. Instrum.* **1955**, *26*, 1150–1157.

[90] Florian Hirsch, PhD thesis, University of Wuerzburg, Wuerzburg, **2021**.

[91] G. von Helden, D. van Heijnsbergen, G. Meijer, *J. Phys. Chem. A* **2003**, *107*, 1671–1688.

[92] V. N. Bagratashvili, V. S. Letokhov, A. A. Makarov, E. A. Ryabov, *Laser Chem.* **1984**, *4*, 311–423.

[93] M. Vainio, L. Halonen, *Phys. Chem. Chem. Phys.* **2016**, *18*, 4266–4294.

[94] R. L. Jacobsen, R. D. I. Johnson, K. K. Irikura, R. N. Kacker, *J. Chem. Theory Comput.* **2013**, *9*, 951–954.

[95] M. W. D. Hanson-Heine, M. W. George, N. A. Besley, *J. Phys. Chem. A* **2012**, *116*, 4417–4425.

[96] P. Geerlings, F. De Proft, W. Langenaeker, *Chem. Rev.* **2003**, *103*, 1793–1874.

[97] M. A. Palafox, *Phys. Sci. Rev.* **2017**, *2*, 1–21.

[98] I. M. Alecu, J. Zheng, Y. Zhao, D. G. Truhlar, *J. Chem. Theory Comput.* **2010**, *6*, 2872–2887.

[99] A. P. Scott, L. Radom, *J. Phys. Chem.* **1996**, *100*, 16502–16513.

[100] M. D. Halls, J. Velkovski, H. B. Schlegel, *Theor. Chem. Acc.* **2001**, *105*, 413–421.

[101] H. Yoshida, K. Takeda, J. Okamura, A. Ehara, H. Matsuura, *J. Phys. Chem. A* **2002**, *106*, 3580–3586.

CHAPTER 3

THE GAS-PHASE INFRARED SPECTRA OF THE 2-METHYLALLYL RADICAL AND ITS HIGH-TEMPERATURE REACTION PRODUCTS

This chapter is reproduced and partly adapted from

T. Preitschopf, F. Hirsch, A. K. Lemmens, A. M. Rijs, I. Fischer, *Phys. Chem. Chem. Phys.* **2022**, *24*, 7682–7690

with permission from the PCCP Owner Societies.

3.1 Abstract

The resonance-stabilized 2-methylallyl radical, 2-MA, is considered as a possible intermediate in the formation of polycyclic aromatic hydrocarbons (PAHs) in combustion processes. In this work, we report on its contribution to molecular growth in a high-temperature microreactor and provide mass-selective IR/UV ion dip spectra of the radical, as well as the various jet-cooled reaction products, employing free electron laser radiation in the MIR region. Small (aromatic) hydrocarbons such as fulvene, benzene, styrene, or *para*-xylene, as well as polycyclic molecules, like (methylated) naphthalene, were identified with the aid of *ab initio* DFT computations. Several reaction products differ by one or more methyl groups, suggesting that molecular growth is dominated by (de)methylation in the reactor.

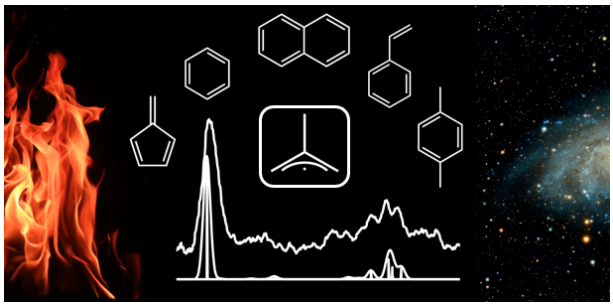

Figure 3.1. ToC graphic of published work on the high-temperature reactions of 2-methylallyl radicals. Reproduced from Ref. [1] with permission from the Physical Chemistry Chemical Physics (PCCP) Owner Societies.

3.2 Introduction

Open-shell molecules are known to play an important role in the formation of polycyclic aromatic hydrocarbons (PAHs) and soot.[2] PAH formation has been a central topic in combustion research due to the carcinogenic potential of the compounds. It has also been realized that radical reactions similar to the ones in combustion lead to the formation of PAHs and related molecules in interstellar space.[3] A recent review summarizes the various mechanisms that are thought to form PAHs.[4] However, the process is far from understood, because the complex chemistry of the relevant systems is difficult to disentangle. Resonance-stabilized radicals (RSR) are of particular relevance, because they can accumulate in a reactive environment and contribute to molecular growth.[5] The 2-methylallyl radical (2-MA), **2** in Scheme 3.1, is an example of such an RSR. Methylallyl radi-

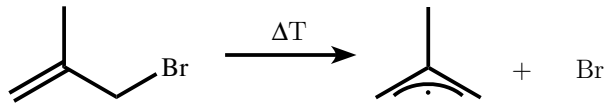

m/z = 134 / 136 m/z = 55

1 2

Scheme 3.1. Generation of the 2-methylallyl radical **2** by flash pyrolysis from 3-bromo-2-methylpropene **1**. Adapted from Ref. [1] with permission from the PCCP Owner Societies.

cals (C_4H_7) have been identified in the combustion of isobutene[6] and *tert*-butyl ethers.[7] Substituted allyl radicals are also important in the decomposition of unsaturated fatty acid esters, which are considered as potential biofuels. At high temperature, they preferentially loose H-atoms in the α-position to the C=C double bonds and form intermediates that can be described as alkylated allyl radicals.[8] Furthermore, the CH + C_3H_6 reaction could be a substantial source for C_4H_7 radicals in the interstellar medium.[9] Unsurprisingly, numerous studies on isolated 1- and 2-MA generated mostly by pyrolysis have been reported, including resonance-enhanced multiphoton ionization (REMPI),[10,11] time-resolved spectroscopy,[12,13] photofragment spectroscopy to identify the unimolecular dissociation products[11] and threshold photoelectron spectroscopy (TPES) to obtain ionization energies (IE) of 7.88 eV for 2-MA, 7.48 eV for *E*-1-methylallyl radical (1-MA) and 7.59 eV for *Z*-1-MA.[14] Some information on the vibrational frequencies of **2** is available from infrared spectroscopy in a rare gas matrix[15,16] and from resonance Raman spectroscopy in the gas-phase.[17] In contrast, bimolecular reactions of 2-MA have scarcely been investigated. Recently, our group studied the kinetics of the reaction 2-MA + O_2 between 1 and 3 mbar and derived a high-pressure limit rate constant $k_\infty = (5.1\pm1.0)\cdot10^{11}$ $cm^3\cdot(mol\cdot s)^{-1}$ for the reaction.[18]

High-temperature (pyrolysis) microreactors are not only an efficient method to generate hydrocarbon radicals, but are also well-suited to investigate their chemical reactions at high temperature.[19–21] A pyrolysis reactor also provides an environment to study bimolecular reactions of radicals and to detect polycyclic aromatic hydrocarbons that are efficiently formed. In most experiments, photoionization mass spectrometry (PIMS)[22] or threshold photoelectron spectroscopy (TPES) using synchrotron radiation[23] were employed to characterize the reaction products. Alternatively, IR/UV ion dip spectroscopy[24] in a supersonically cooled free jet is well suited to study reactions in a flow reactor, because it combines the structural sensitivity of infrared spectroscopy with mass information. The ground-state IR spectra are obtained by monitoring the depletion of the REMPI signal upon IR-absorption of a selected m/z peak, resulting in a species-selected IR spectrum.

Since an intense IR source is required to excite dilute samples in the MIR fingerprint region, the experiments employed radiation from a free electron laser (FEL). Gas-phase IR-spectra of several reactive molecules have been recorded[25–28] and bimolecular reaction products[27,29–32] of radicals have been characterized using IR/UV ion dip spectroscopy.

3.3 Experimental

2-MA (**2**) was produced by flash pyrolysis from 3-bromo-2-methylpropene (**1**) (Sigma-Aldrich, assay 97.0 %, used without further purification), see Scheme 3.1. This precursor has been shown before to efficiently generate **2** at high number density.[10,12] The 1-methylallyl isomer is not produced from this precursor, as concluded from TPES.[14] The precursor was seeded in 2.0 bar of argon (mole fraction $\approx$ 5 %) and a pulsed jet was produced using a solenoid valve (20 Hz) with a resistively heated SiC-tube (microreactor)[33] of 35 mm length, an inner diameter of 1 mm and a heated region of 8 mm, to cleave the precursor molecules. Note that the large length of the SiC tube fosters bimolecular reactions. The pyrolysis temperature was estimated to be around 1000 K. In the beginning of the gas pulse only a few bimolecular reactions occurred and supersonically cooled 2-MA can be studied, while in the centre of the pulse bimolecular reactions became more apparent. Therefore, the timing of the laser was chosen to overlap with the centre of the gas pulse. The pulsed free jet was expanded into a differentially pumped vacuum apparatus.[24] While the experimental conditions were optimized by PIMS using 118 nm radiation (Nd:YAG laser 9th harmonic), the IR/UV experiments were carried out at the FELIX free electron laser laboratory[24,34] at the Radboud University, Nijmegen, The Netherlands.

Here, the skimmed molecular jet was crossed in the interaction region of a time-of-flight mass spectrometer by two laser beams.[24] Molecules were ionized *via* [1+1] REMPI by a perpendicular, unfocused UV laser (20 Hz) at 255.3 nm with 1–1.2 mJ of power per pulse. This wavelength is resonant with the $(\nu_{28})^1(\nu_{25})^1$ combination band of the B $^2A_1$ (3s) state of **2**.[35] To record the IR/UV spectra,[24] the colinearly propagating free electron laser FELIX[34] was fired with a repetition rate of 10 Hz around 200 ns prior to the UV laser. It was scanned over the fingerprint region from 620 to 1750 cm^{-1} in steps of 2 cm^{-1}. Usually, FELIX (10 μs pulse) delivers up to 200 mJ of output power and has a bandwidth of roughly 1 % of the central photon frequency. At each step, 50 shots were recorded with the IR radiation present and 50 shots without. The IR/UV spectra were then obtained by dividing the signal without IR radiation by the signal with IR radiation, taking the

decadic logarithm and correcting for IR laser power. The quality of the spectra was improved by averaging over several scans and using digital Savitzky–Golay filtering.

The spectra were assigned based on harmonic IR frequency computations performed at the DFT/B3LYP/6-311++G(d,p) level of theory[36] employing the *Gaussian09* computational chemistry software.[37] All frequencies were scaled with an empirical factor of 0.985, within the range of values recommended by previous benchmark studies.[38] Only for *para*-xylylene (m/z 104) computations including anharmonicity were available.[39] The resulting stick spectra were convolved with a Gaussian-shaped function with a full width at half maximum (FWHM) of 30 cm^{-1} to facilitate comparison with the experimental IR/UV spectra. For m/z 106 and 120, *cf.* Figure 3.4 and Figure S1 in Appendix A, gas-phase FT-IR spectroscopy was employed to substantiate the assignment using a Bruker IFS 120HR spectrometer with a long path cell. The spectra were deliberately recorded with a resolution of 16 cm^{-1} for better comparison. Vibrational modes were grouped according to their symmetry and numbered with decreasing wavenumber.

Ionization energies of possible pyrolysis products were computed using the CBS-QB3 approach, while the calculations of standard enthalpies of potential reaction routes were conducted at the DFT/B3LYP/6-311++G(d,p) level of theory.[36]

3.4 Results

3.4.1 Mass spectra

The mass spectra illustrating the pyrolysis conditions are displayed in Figure 3.2. The upper spectrum was recorded at 118 nm (10.5 eV), which is sufficient to ionize almost all molecules in the molecular beam in a single photon process (SPI). It permits to monitor species with low m/z, which usually do not absorb in the UV. Although distinct concentration measurements demand near-threshold ionization cross sections,[40] the spectrum gives a better representation of the relative molecular concentrations in the jet than the REMPI TOF-MS spectrum (Figure 3.2b). At a pyrolysis temperature of around 1000 K, the precursor **1** (m/z 134/136) is almost fully converted and the spectrum is dominated by m/z 55 assigned to **2**. A comparison of a 118 nm mass spectrum with and without pyrolysis is given in Figure S2 in Appendix A. In addition a breakdown diagram is given in Figure S3 (Appendix A), yielding an $AE_{0K}(C_4H_7Br, C_4H_7^+) = 10.38$ eV. This shows that dissociative photoionization plays a minor role in the REMPI TOF-MS experi-

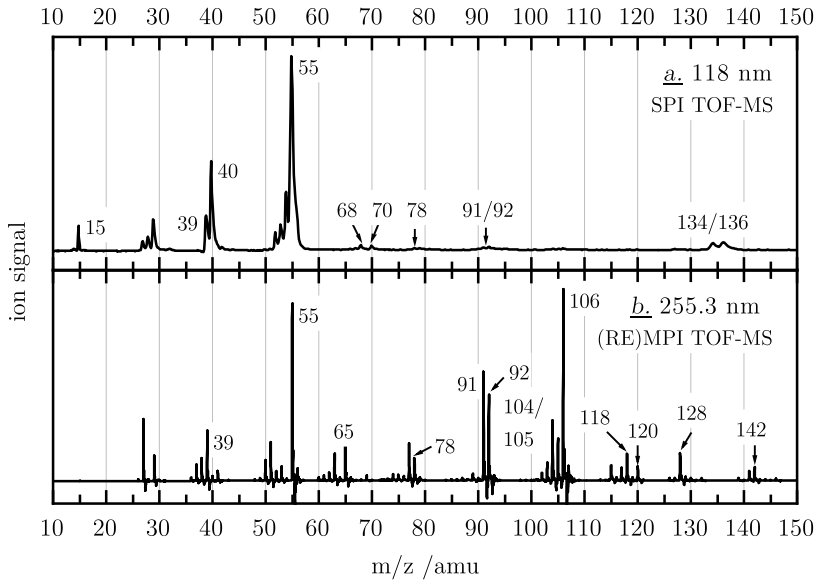

Figure 3.2. Photoionization mass spectra of **1** with pyrolysis (around 1000 K) recorded at 118 nm (10.5 eV) in a single photon ionization process (SPI, trace a) and at 255.3 nm (4.86 eV) in a [1+1] REMPI process (b). Adapted from Ref. [1] with permission from the PCCP Owner Societies.

ment. Four peaks at low mass have been characterized by TPES.[41] The intense peak at m/z 40 originates from beta scission of **2** to allene and a methyl radical (m/z 15),[42,43] whereas the signal at m/z 70 is identified as 2-methyl-1-butene due to recombination of **2** with a methyl radical (see Figure S4 in Appendix A).[42] Furthermore, 2-methyl-1,3-butadiene (m/z 68) is formed by H_2 loss (Figure S5). The peak at m/z 39 corresponds to the propargyl radical (Figure S6, Appendix A), which can be formed by hydrogen abstraction of allene at high temperature as observed in shock tube studies,[44,45] or by CH_4 loss from **2**. Small signals at m/z 78, 91 and 92, corresponding to the masses of C_6H_6 isomers, benzyl and toluene, suggest that aromatic hydrocarbons start to form from **2** under the experimental conditions.

Figure 3.2b shows a [1+1] REMPI TOF-MS spectrum recorded at 255.3 nm (4.86 eV), which allows to efficiently monitor molecules with a UV chromophore. Several peaks appear with enhanced intensity (*e.g.*, m/z 78, 91, 92) and additional higher masses are observed. This is due to electronic excited states that resonantly enhance the ionization probability of hydrocarbons with an aromatic chromophore.[46] Note that the vast majority of aromatic hydrocarbons possess (broad) intermediate electronic excited states around 255 nm.[47] The most prominent peak in the spectrum appears at m/z 106. Further peaks of significant inten-

sity are present at m/z 118, 120, 128 and 142. Interestingly, several peaks differ by 14 atomic mass unit (amu) (*e.g.*, masses 78–92–106–120), which already suggests that (de)methylation plays an essential role in the chemistry of **2** in the reactor.

3.4.2 IR/UV spectra

Although mass spectrometry allows to derive qualitative models of the chemistry in the reactor, it is not sufficient to provide reliable structure assignments. Before possible chemical reactions are discussed, the molecular pyrolysis products identified by IR/UV ion dip spectroscopy will be presented combined with quantum chemical calculations. As shown below, very good agreement is achieved, and most reaction products can be unambiguously identified. Many of the molecules studied here are resonantly ionized *via* unstructured electronic bands at 255.3 nm, rather than well defined (ro-) vibronic transitions. However, IR excitation can lead to a large change in the absorption cross section even for broad bands.[48–52] In addition, absorption of further IR photons may cause fragmentation and thus induce a dip in the REMPI spectrum.[51] As absorption of the first IR photon is the bottleneck for this process, linear IR spectra are recorded.

m/z 55. Only few IR spectra of isolated radicals in a free jet have been recorded so far.[25–28] In Figure 3.3 the IR/UV spectrum of m/z 55 is presented (black line). As mentioned above, the UV wavelength of 255.3 nm is resonant with the $(\nu_{28})^1(\nu_{25})^1$ combination band of the B $^2A_1$ (3s) state of **2**.[35] A lifetime of 9.3 ps was reported for this band.[12]

The width of the vibrational bands in the IR/UV spectrum is likely caused by the rotational temperature of the pyrolytically generated species and by power broadening due to the high power IR radiation. The excellent agreement with the computation (blue line) and previous work[15–17] proves that **2** is the only carrier of the spectrum and no isomerization takes place. For the most intense band at 799 cm^{-1} a depletion of the ion signal of roughly 50 % was observed. The band is assigned to the ν_{12} symmetric CH_2 out-of-plane bending vibration. The value is in excellent agreement with the wavenumber of 795 cm^{-1} observed in matrix.[15,16] At higher wavenumbers the IR/UV spectrum displays a broad band beginning around 1370 cm^{-1} with three identifiable maxima. The first one at 1397 cm^{-1} is assigned to the ν_7 symmetric deformation (umbrella) motion of the CH_3 group. The next maximum at 1451 cm^{-1} is composed of three fundamentals which overlap to a single broad signal as shown by the computation. The third maximum at 1492 cm^{-1} is finally assigned to the ν_5 symmetric CH_2 scissor vibration. A comparison of the observed frequencies with previous work[15–17] is given in Table 3.1.

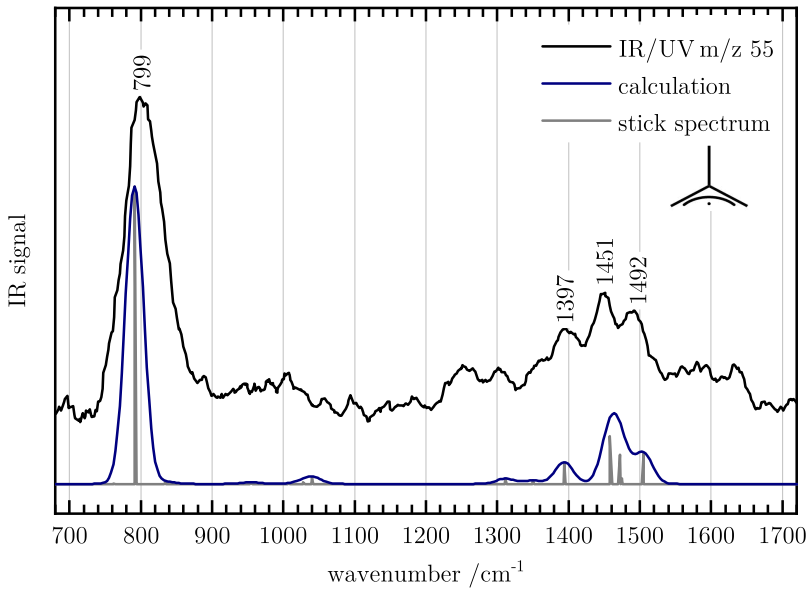

Figure 3.3. IR/UV spectrum of m/z 55 (black line) in comparison to a computed IR spectrum of **2** (blue line). A stick spectrum (in grey) is presented for a proper assignment of the various normal modes. Adapted from Ref. [1] with permission from the PCCP Owner Societies.

m/z 106. The IR/UV spectrum of the most prominent mass signal at m/z 106 in the REMPI TOF-MS spectrum is depicted in Figure 3.4a. The mass already indicates an isomer of xylene (C_8H_{10}) as the carrier of the spectrum. In fact, *para*-xylene could be easily formed from the dimerization of two 2-MA radicals. For comparison, the computed IR spectrum of *para*-xylene is presented in Figure 3.4c. Interestingly, the computation overestimates the intensities of the bands at 1046 cm^{-1} and 1474 cm^{-1}. On the other hand, the band positions are predicted properly. To check the assignment, a gas-phase FT-IR spectrum of *para*-xylene was recorded (Figure 3.4b) and excellent agreement was observed. As no bands from *ortho*- and *meta*-xylene are identified (see Figure S7 in Appendix A), m/z 106 can be conclusively assigned to the isomer *para*-xylene as the sole carrier of the spectrum.

m/z 78. One of the most interesting traces is the IR/UV spectrum of m/z 78 (Figure 3.5a), which indicates the formation of benzene (C_6H_6) in the reactor (Figure 3.5b). This is confirmed by its characteristic C–H out-of-plane wagging vibration at 680 cm^{-1} in the experimental spectrum. Due to its high symmetry (D_{6h}), benzene displays only a small number of symmetry-allowed vibrations. However, several more bands are observed in the IR/UV spectrum that cannot be assigned to

Table 3.1. Vibrational frequencies of **2** in comparison with previous work. Adapted from Ref. [1] with permission from the PCCP Owner Societies.

Vib. mode	Assignment	This work (gas-phase)	Matrix-IR Ref. [15, 16]	Resonance Raman (gas-phase) Ref. [17]	Computation
ν_5	CH_2 scissors (sym)	1492 cm^{-1}	1498 cm^{-1}	1492 cm^{-1}	1505 cm^{-1}
ν_7	CH_3 sym deform (umbrella)	1397 cm^{-1}	1394 cm^{-1}	1392 cm^{-1}	1394 cm^{-1}
ν_{12}	CH_2 out-of-plane bend (sym)	799 cm^{-1}	795 cm^{-1}	–	791 cm^{-1}

this compound. This suggests the formation of further C_6H_6 isomers. Based on the comparison with a computed IR spectrum (Figure 3.5c), the remaining bands can be allocated to fulvene. The peak at 782 cm^{-1} is assigned to the C-H out-of-plane bending vibration. The wavenumber is in good agreement with the value of 769 cm^{-1} reported in a previous vapour-phase infrared spectrum.[53] Further, the CH_2 out-of-plane bending vibration at 910 cm^{-1} and the ring C=C symmetric stretching mode at 1496 cm^{-1} match the reported wavenumbers well.[53] Note that fulvene has been identified during the pyrolysis of **1** by TPES,[41,54], see Figure S8 in Appendix A.

m/z 104. Based on comparison with a computed IR spectrum (Figure 3.6b), the IR/UV spectrum of m/z 104 (Figure 3.6a) is dominated by styrene (C_8H_8). In particular, the strong ring puckering mode at 706 cm^{-1} and the out-of-plane deformation mode at 779 cm^{-1} are in excellent agreement with the computation. Further, the peaks observed at 916 cm^{-1} and at 996 cm^{-1} originating from the CH_2 wagging vibration and the deformation mode respectively, match the computed frequencies very well. Interestingly, the CH_2 wagging vibration exhibits a pronounced shoulder at lower wavenumbers that is not represented by the computation. This indicates the formation of additional C_8H_8 isomers. In particular, xylylenes were suggested

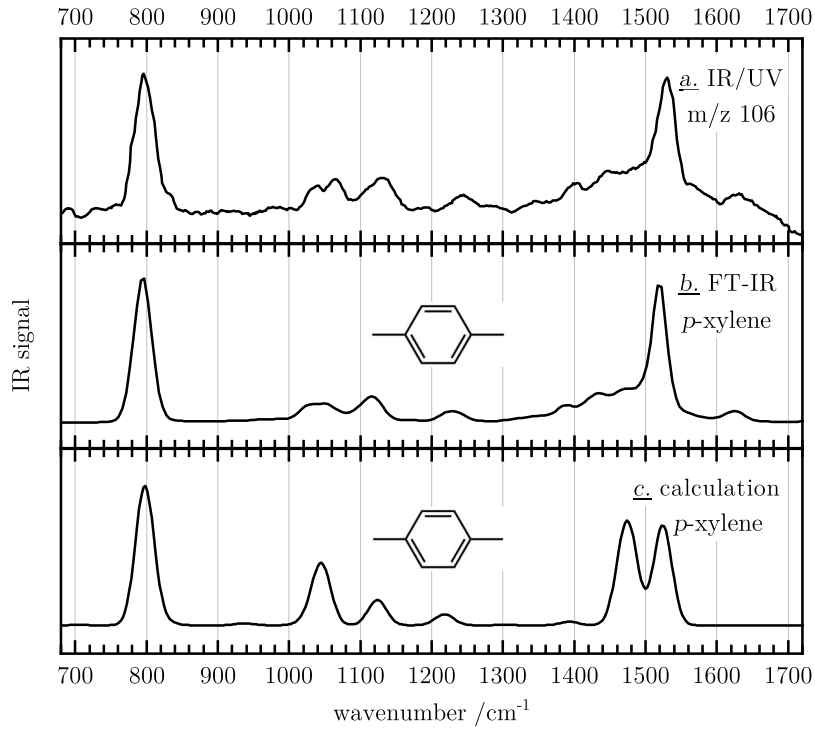

Figure 3.4. The IR/UV spectrum of m/z 106 (trace a) is assigned to *para*-xylene based on comparison with a gas-phase FT-IR spectrum (b). The computed IR spectrum (trace c) represents the band positions well, but the intensities of the bands at 1046 cm^{-1} and 1474 cm^{-1} are overestimated. Adapted from Ref. [1] with permission from the PCCP Owner Societies.

as intermediates during styrene formation in the combustion of xylenes.[55] In fact, *para*-xylylene was detected by TPES in previous work on 2-MA,[41] see Figure S9 in Appendix A. A comparison with the computed spectrum in the bottom trace indicates that this isomer might be responsible for the broadening and thus confirms a small contribution. Note that the computed oscillator strength f for the $S_2 \leftarrow S_0$ transition in *para*-xylylene is roughly a factor of three larger than for the bright $\pi\pi^*$ transition in styrene.[39]

m/z 128, 142. The first polycyclic aromatic molecule is identified in the IR/UV spectrum of m/z 128 (Figure 3.7d). Here, a band at 782 cm^{-1} appears and is assigned to the characteristic C-H wagging vibration (in-phase) of naphthalene ($C_{10}H_8$). As the computed (Figure 3.7e) and the experimental spectrum are in excellent agreement, the polycyclic hydrocarbon can be unambiguously identified as the only carrier of the spectrum. The peak at m/z 142 in the mass spectrum is closely linked to m/z 128 as both signals differ by 14 amu. This indicates the

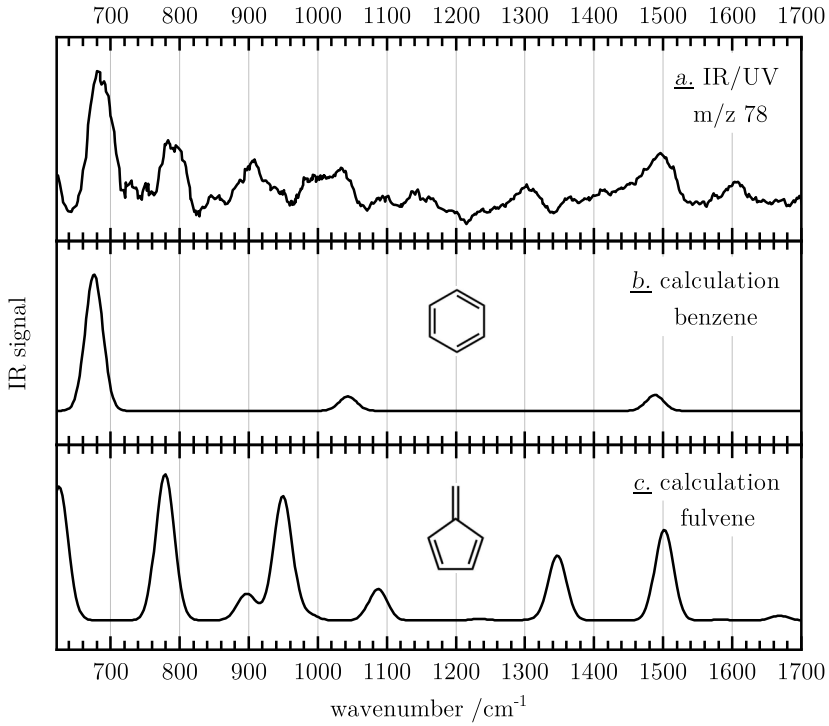

Figure 3.5. The IR/UV spectrum of m/z 78 (trace a) displays the formation of the C_6H_6 isomers benzene (b) and fulvene (c) in the reactor. Adapted from Ref. [1] with permission from the PCCP Owner Societies.

formation of methylated naphthalene isomers ($C_{11}H_{10}$) in the reactor which is confirmed by the corresponding IR/UV spectrum (Figure 3.7a). The spectrum is dominated by 2-methylnaphthalene as all major C-H wagging vibrations at 741, 811, and 848 cm^{-1} are represented well by the computation (Figure 3.7b). Although a shoulder at 788 cm^{-1} (highlighted by an arrow) might be allocated to two wagging fundamentals of 1-methylnaphthalene (Figure 3.7c), the contribution of this isomer is small at best.

Further masses. In addition, the mass signal at m/z 92 was assigned to toluene (Figure S10), m/z 118 to *para*- and *ortho*-methylstyrene (Figure S11), and m/z 120 to 1-ethyl-4-methylbenzene (Figure S1). The corresponding IR/UV spectra are given in Appendix A.

3.5 Discussion

The IR spectra presented above confirm that bimolecular reactions of **2** occur in a high temperature microreactor at around 1000 K and compete with unimolecular

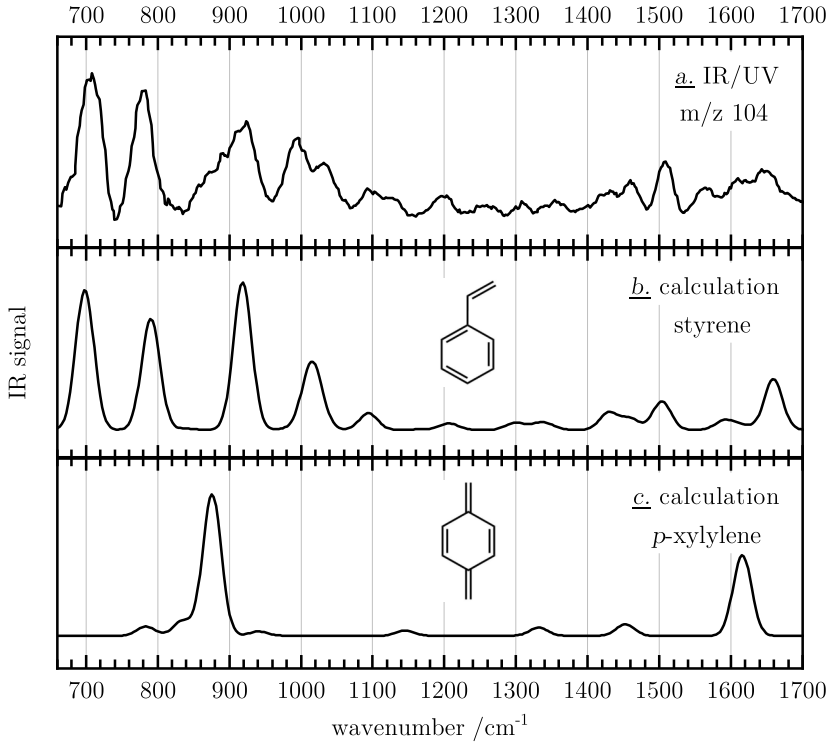

Figure 3.6. IR/UV spectrum of m/z 104 (trace a) is dominated by styrene (b). The pronounced shoulder at around 870 cm^{-1} might indicate the formation of further C_8H_8 isomers (trace c). Adapted from Ref. [1] with permission from the PCCP Owner Societies.

decomposition. The various reaction products (highlighted in red) and suggested reaction pathways are depicted in Scheme 3.2. Several small molecules and radicals without a UV chromophore have been characterized by TPES[41] and are indicated in black. Products that are presented in a dashed box were neither identified *via* IR/UV ion dip spectroscopy nor by TPES but are suggested to participate in the chemistry of the reactor based on mass spectrometric observation (*cf.* Figure 3.2). and comparison with earlier work. Selected recombination and decomposition reactions of **2** have been investigated before, see Ref. [6, 42, 56, 57]. Three essential reactions were identified that compete depending on the ambient temperature and pressure. Based on combined flame speed and shock tube studies by Zhou *et al.*, the self-recombination reaction of **2** to 2,5-dimethyl-1,5-hexadiene (**3**), **A** in Scheme 3.2, dominates at moderate temperatures (850–1000 K).[6] The dimerization is highly exothermic by -254 $kJ \cdot mol^{-1}$.[57] At higher temperature (> 1100 K), Tranter *et al.* observed significant unimolecular decomposition of **2** to allene and a methyl radical ($\Delta_r H^0$ = +204 $kJ \cdot mol^{-1}$, reaction **B** in Scheme 3.2).[57] This reaction has been verified by the observation of allene in previous TPES work.[41]

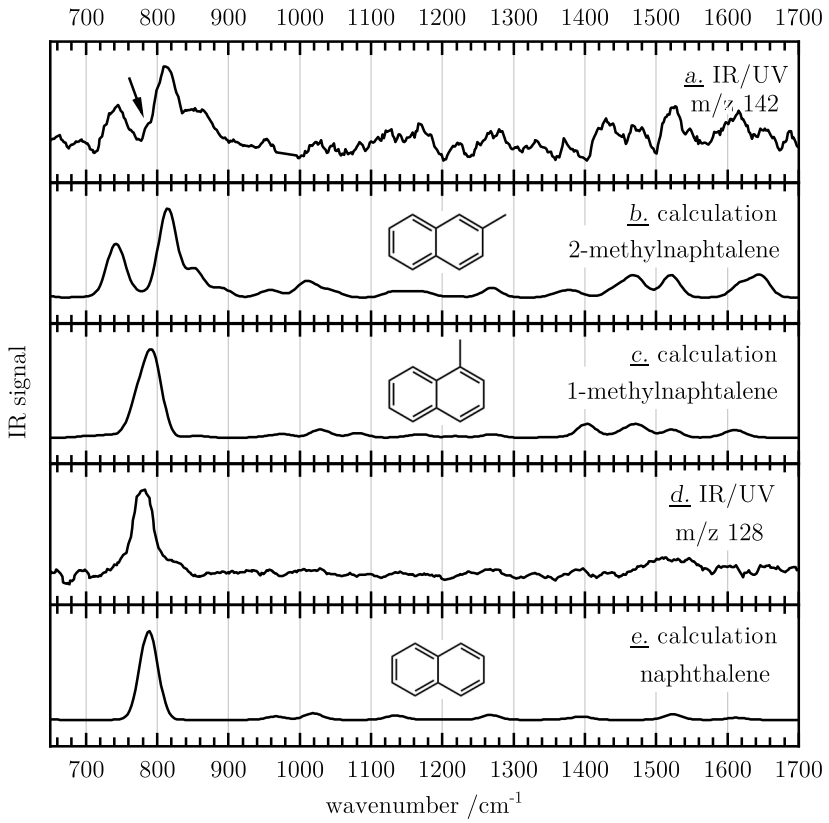

Figure 3.7. The carrier of the IR/UV spectrum of m/z 128 is identified as naphthalene (traces d and e). The spectrum of m/z 142 is dominated by 2-methylnaphthalene (traces a and b). Possible formation of 1-methylnaphthalene (trace c) could be indicated by the shoulder at 787 cm^{-1} (arrow). Adapted from Ref. [1] with permission from the PCCP Owner Societies.

It serves as a source of methyl radicals and influences the third reaction, recombination with CH_3, which becomes more relevant with an increasing number of CH_3 radicals in the reactor.[42,57] In the present study, dissociation of **2** as well as addition of CH_3 are indicated by the mass signals at m/z 15, 40, and 70 in the 10.5 eV SPI spectrum (*cf.* Figure 3.2a). Interestingly, the recombination product **3** (m/z 110) is not observed in the mass spectrum despite a computed ionization energy of 9.09 eV. However, the presence of reaction **A** and thus compound **3** is suggested by the formation of *para*-xylene (m/z 106), which is identified by IR/UV ion dip spectroscopy (see Figure 3.4), and is most likely generated *via* dehydrocyclization ($-H_2$) and aromatization ($-H_2$) of **3**. The absence of a mass signal suggests dissociative photoionization at 10.5 eV or a very efficient conversion of **3** to *para*-xylene at high temperature in the microreactor. The latter is further sub-

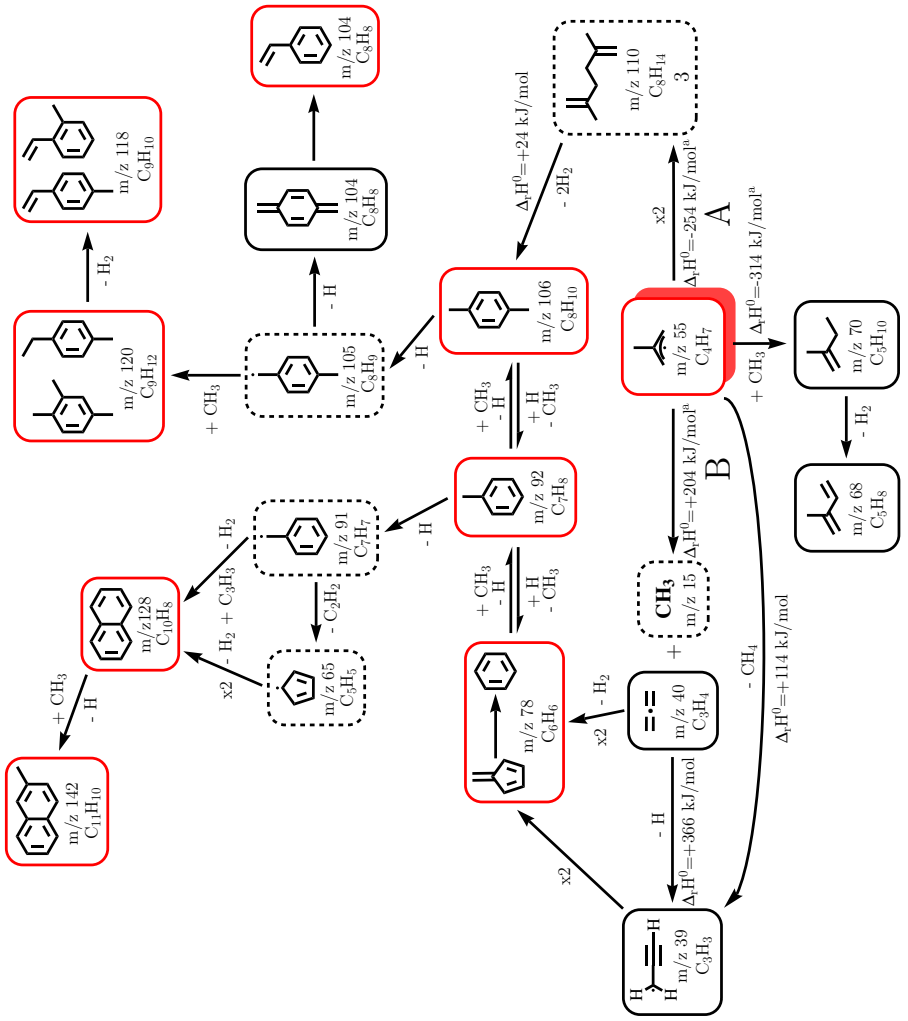

Scheme 3.2. The 2-methylallyl radical and its high temperature self-reaction products identified by IR/UV ion dip spectroscopy (red boxes). Molecules that are highlighted in black were identified by TPES.[41] Products that are marked by dashed boxes are suggested to be generated in the microreactor based on mass spectrometry (*cf.* Figure 3.2) and literature data. [a]Ref. [57]. Adapted from Ref. [1] with permission from the PCCP Owner Societies.

stantiated by a small, computed heat of reaction of +24 kJ·mol^{-1}, see eq. (3.1), and the entropically favourable H_2 loss.

$$\mathbf{3} \longrightarrow \textit{para}\text{-xylene} + 2H_2,\ \Delta_r H^0 = +24\ \text{kJ·mol}^{-1} \tag{3.1}$$

As indicated in the mass spectra (Figure 3.2) and confirmed by IR/UV ion dip spectroscopy, several molecules are connected by addition or loss of methyl groups.

Some examples are benzene and toluene, *para*-xylene and *para*-ethyltoluene as well as naphthalene and 2-methylnaphthalene. This suggests that methylation, driven by the significant amounts of CH_3 radicals present in the reactor due to **B**, plays a dominant role in the molecular growth. Demethylation of toluene (see Figure S10 in Appendix A) has been observed in the pyrolysis of *para*-xylene[58,59] and in the combustion of *para*-xylene fuels.[55] Consecutive demethylation of benzene has been shown to be present as well.[55,60,61] However, the reverse reaction benzene + CH_3 and toluene + CH_3 might also occur.[62] Significant contributions to benzene formation can possibly be attributed to the propargyl radical self-recombination reaction, which is considered as a primary route to benzene formation in combustion processes.[63,64] The formation of propargyl in the microreactor is indicated by the mass peak at m/z 39 in the SPI spectrum (see Figure 3.2a) and confirmed by TPES (Figure S6, Appendix A).[41] It might be formed by abstraction of a H atom from allene ($\Delta_r H^0 = +366$ kJ·mol^{-1}).[44,45] A less endothermic alternative is CH_4 loss from methylallyl with $\Delta_r H^0 = +114$ kJ·mol^{-1}. However, this reaction will certainly be associated with an additional barrier for H-migration. Here, the detection of fulvene by IR/UV ion dip spectroscopy becomes relevant (Figure 3.5). Fulvene is known to be an intermediate at high temperature in the recombination reaction of propargyl radicals and has been observed in several studies.[65,66] A shock tube study of Tranter *et al.* indicates that fulvene and benzene are formed simultaneously below 1200 K, with benzene predominantly being formed *via* routes that do not pass through fulvene, and fulvene to benzene isomerization not being significant.[63,66]

$$2C_3H_4 \longrightarrow \text{fulvene} + H_2,\ \Delta_r H^0 = \text{-158 kJ·mol}^{-1} \tag{3.2}$$

$$2C_3H_4 \longrightarrow \text{benzene} + H_2,\ \Delta_r H^0 = \text{-299 kJ·mol}^{-1} \tag{3.3}$$

A related route to fulvene and benzene starting from allene was suggested by Bermudez and co-workers, see eq. (3.2) and (3.3).[67] Following dimerization to 1,2-dimethylenecyclobutane,[68] the open chain C_6H_6 isomer 1,5-hexadiyne is formed by H_2 loss, which is an important intermediate to fulvene and benzene in the propargyl self-recombination reaction, too.[63,65] As the generation of benzene is significantly more exothermic than that of fulvene,[69–71], see eq. (3.2) and (3.3), generation of benzene in the microreactor dominates. The substantial fulvene signal likely appears due to the much higher UV cross section.[72]

Styrene was identified as the dominant carrier of the mass signal at m/z 104 (*cf.* Figure 3.6), but *para*-xylene (C_8H_8) was observed under comparable condi-

tions by TPES (see Figure S9 in Appendix A).[41] After consecutive loss of an H atom, it is most likely generated *via* the *para*-xylyl radical (C_8H_9) in the decomposition of *para*-xylene.[73–75] As the most stable isomer,[76] styrene might be created *via* isomerization of *para*-xylylene at high temperature, when sufficient energy is present to surmount the activation barrier. A possible mechanism has been suggested before.[55]

The *para*-xylyl radical, indicated by the mass peak at m/z 105 in the REMPI TOF-MS spectrum (Figure 3.2b), can further act as an intermediate to *para*-ethyltoluene and 1,2,4-trimethylbenzene. Based on the IR/UV data (see Figure S1 in Appendix A) it is hard to decide which isomer is preferentially formed. Chemical intuition suggests the generation of *para*-ethyltoluene due to a combination of the *para*-xylyl radical with a methyl radical. This is supported by previous studies that reported *para*-ethyltoluene as the sole C_9H_{12} isomer in the pyrolysis of *para*-xylene.[55,58,59] Furthermore, IR/UV spectra of methylated styrene isomers have been observed (C_9H_{10}, see Figure S11 in Appendix A). These products are readily accessible from *para*-ethyltoluene by loss of a hydrogen molecule.[58] A heat of reaction of +102 kJ·mol^{-1} was computed for the generation of *para*-methylstyrene. The IR/UV data indicate the formation of the *ortho* isomer, too, while signals of *meta*-methylstyrene are not apparent.

Naphthalene ($C_{10}H_8$, *cf.* Figure 3.7d) is assumed to mainly result from the reaction between propargyl and a benzyl radical,[61,62,77] a primary pyrolysis product of toluene (Figure S10 in Appendix A).[60,62,78] Benzyl formation is indicated by the peak at m/z 91 in the mass spectra (see Figure 3.2). Furthermore, contributions to naphthalene generation might be traced back to the self-reaction of the cyclopentadienyl radical (C_5H_5, m/z 65 in Figure 3.2b),[79,80] which has also been observed in the decomposition of toluene.[80,81] At high temperature, 1- and 2-naphthylradicals will be formed,[61] which can easily combine with a methyl radical to form 1-methyl- and 2-methylnaphthalene. However, the IR/UV data (*cf.* Figure 3.7a) display only strong signals of the 2-methylnaphthalene radical, while the formation of 1-methylnaphthalene is not confirmed unambiguously. It should be noted that a recent study on PAH formation in a plasma jet also found a propensity for 2-substituted naphthalene compared to their 1-substituted counterparts.[32]

3.6 Conclusions

Resonance-stabilized methylallyl radicals are involved in the formation of PAHs and soot. In this work we recorded the gas-phase IR spectrum of the 2-methylallyl radical (**2**) in the fingerprint region and investigated its contribution to molecular growth in a high-temperature microreactor by IR/UV ion dip spectroscopy employing free electron laser radiation. This approach combines the isomer selectivity of IR spectroscopy with the mass selectivity of resonant photoionization. Products without a UV chromophore have been identified by threshold photoelectron spectroscopy.[41] Radical **2** was generated by flash pyrolysis from 3-bromo-2-methylpropene at around 1000 K and resonantly ionized *via* the $(\nu_{28})^1(\nu_{25})^1$ combination band of the B $^2A_1$ (3s) state at 255.3 nm.[35] Our work confirms that unimolecular decomposition to allene and methyl competes with the recombination of **2**, which facilitates direct access to aromatic hydrocarbons in a single bimolecular step as suggested by the formation of *para*-xylene. Several further small aromatics were identified such as benzene, toluene, or styrene. Furthermore, the C_6H_6 isomer fulvene was observed, probably mainly by recombination of propargyl, but possibly also due to dimerization of allene. Several pyrolysis products are connected by addition or loss of methyl groups which indicates that (de)methylation is of key importance for molecular growth of **2**. Some examples are methylated styrene isomers, *para*-ethyltoluene or 2-methylnaphthalene that are formed by secondary reactions. The appearance of the latter as well as of naphthalene substantiates the relevance of **2** in the formation of PAHs in reactive environments.

References

[1] T. Preitschopf, F. Hirsch, A. K. Lemmens, A. M. Rijs, I. Fischer, *Phys. Chem. Chem. Phys.* **2022**, *24*, 7682–7690.

[2] M. Frenklach, *Phys. Chem. Chem. Phys.* **2002**, *4*, 2028–2037.

[3] E. Peeters, C. Mackie, A. Candian, A. G. G. M. Tielens, *Acc. Chem. Res.* **2021**, *54*, 1921–1933.

[4] R. I. Kaiser, N. Hansen, *J. Phys. Chem. A* **2021**, *125*, 3826–3840.

[5] T. Schmidt, *Int. Rev. Phys. Chem.* **2016**, *35*, 209–242.

[6] C.-W. Zhou, Y. Li, E. O'Connor, K. P. Somers, S. Thion, C. Keesee, O. Mathieu, E. L. Petersen, T. A. DeVerter, M. A. Oehlschlaeger, G. Kukkadapu, C.-J. Sung, M. Alrefae, F. Khaled, A. Farooq, P. Dirrenberger, P.-A. Glaude, F. Battin-Leclerc, J. Santner, Y. Ju, T. Held, F. M. Haas, F. L. Dryer, H. J. Curran, *Combust. Flame* **2016**, *167*, 353–379.

[7] T. Zhang, J. Wang, T. Yuan, X. Hong, L. Zhang, F. Qi, *J. Phys. Chem. A* **2008**, *112*, 10487–10494.

[8] C. K. Westbrook, *Annu. Rev. Phys. Chem.* **2013**, *64*, 201–219.

[9] J. M. Ribeiro, A. M. Mebel, *J. Phys. Chem. A* **2016**, *120*, 1800–1812.

[10] C.-C. Chen, H.-C. Wu, C.-M. Tseng, Y.-H. Yang, Y.-T. Chen, *J. Chem. Phys.* **2003**, *119*, 241–250.

[11] M. Gasser, A. Bach, P. Chen, *Phys. Chem. Chem. Phys.* **2008**, *10*, 1133–1138.

[12] J. Herterich, T. Gerbich, I. Fischer, *ChemPhysChem* **2013**, *14*, 3906–3908.

[13] A. Röder, K. Issler, L. Poisson, A. Humeniuk, M. Wohlgemuth, M. Comte, F. Lepetit, I. Fischer, R. Mitric, J. Petersen, *J. Chem. Phys.* **2017**, *147*, 013902.

[14] M. Lang, F. Holzmeier, P. Hemberger, I. Fischer, *J. Phys. Chem. A* **2015**, *119*, 3995–4000.

[15] L. E. Gusel'nikov, G. Zimmermann, U. Ziegler, V. V. Volkova, K. S. Konobevskii, V. I. Smirnov, B. Ondrushka, V. G. Avakyan, N. S. Nametkin, *Dokl. Akad. Nauk SSSR* **1985**, *282*, 1416–1420.

[16] V. G. Avakyan, V. V. Volkova, L. E. Gusel'nikov, U. Ziegler, G. Zimmermann, B. Ondrushka, N. S. Nametkin, *Dokl. Akad. Nauk SSSR* **1986**, *290*, 1133–1137.

[17] J. D. Getty, X. Liu, P. B. Kelly, *J. Chem. Phys.* **1996**, *104*, 3176–3180.

[18] D. Schleier, E. Reusch, M. Gerlach, T. Preitschopf, D. P. Mukhopadhyay, N. Faßheber, G. Friedrichs, P. Hemberger, I. Fischer, *Phys. Chem. Chem. Phys.* **2021**, *23*, 1539–1549.

[19] Q. Guan, K. N. Urness, T. K. Ormond, D. E. David, G. Barney Ellison, J. W. Daily, *Int. Rev. Phys. Chem.* **2014**, *33*, 447–487.

[20] A. Vasiliou, M. R. Nimlos, J. W. Daily, G. B. Ellison, *J. Phys. Chem. A* **2009**, *113*, 8540–8547.

[21] A. M. Scheer, C. Mukarakate, D. J. Robichaud, G. B. Ellison, M. R. Nimlos, *J. Phys. Chem. A* **2010**, *114*, 9043–9056.

[22] L. Zhao, R. I. Kaiser, B. Xu, U. Ablikim, M. Ahmed, M. V. Zagidullin, V. N. Azyazov, A. H. Howlader, S. F. Wnuk, A. M. Mebel, *J. Phys. Chem. Lett.* **2018**, *9*, 2620–2626.

[23] M. N. McCabe, P. Hemberger, E. Reusch, A. Bodi, J. Bouwman, *J. Phys. Chem. Lett.* **2020**, *11*, 2859–2863.

[24] A. M. Rijs, J. Oomens, *Top. Curr. Chem.* **2014**, *364*, 1–42.

[25] R. G. Satink, G. Meijer, G. von Helden, *J. Am. Chem. Soc.* **2003**, *125*, 15714–15715.

[26] K. H. Fischer, P. Hemberger, I. Fischer, A. M. Rijs, *ChemPhysChem* **2010**, *11*, 3228–3230.

[27] K. H. Fischer, J. Herterich, I. Fischer, S. Jaeqx, A. M. Rijs, *J. Phys. Chem. A* **2012**, *116*, 8515–8522.

[28] F. Hirsch, M. Flock, I. Fischer, S. Bakels, A. M. Rijs, *J. Phys. Chem. A* **2019**, *123*, 9573–9578.

[29] P. Constantinidis, H.-C. Schmitt, I. Fischer, B. Yan, A. M. Rijs, *Phys. Chem. Chem. Phys.* **2015**, *17*, 29064–29071.

[30] P. Constantinidis, F. Hirsch, I. Fischer, A. Dey, A. M. Rijs, *J. Phys. Chem. A* **2017**, *121*, 181–191.

[31] F. Hirsch, P. Constantinidis, I. Fischer, S. Bakels, A. M. Rijs, *Chem. Eur. J.* **2018**, *24*, 7647–7652.

[32] A. K. Lemmens, D. B. Rap, J. M. M. Thunnissen, B. Willemsen, A. M. Rijs, *Nat. Commun.* **2020**, *11*, 269.

[33] D. W. Kohn, H. Clauberg, P. Chen, *Rev. Sci. Instrum.* **1992**, *63*, 4003–4005.

[34] D. Oepts, A. F. G. van der Meer, P. W. van Amersfoort, *Infrared Phys. Technol.* **1995**, *36*, 297–308.

[35] M. Gasser, J. A. Frey, J. M. Hostettler, A. Bach, *J. Mol. Spectrosc.* **2010**, *263*, 93–100.

[36] R. Krishnan, J. S. Binkley, R. Seeger, J. A. Pople, *J. Chem. Phys.* **1980**, *72*, 650–654.

[37] M. J. Frisch, G. W. Trucks, H. B. Schlegel, G. E. Scuseria, M. A. Robb, J. R. Cheeseman, G. Scalmani, V. Barone, B. Mennucci, G. A. Petersson, H. Nakatsuji, M. Caricato, X. Li, H. P. Hratchian, A. F. Izmaylov, J. Bloino, G. Zheng, J. L. Sonnenberg, M. Hada, M. Ehara, K. Toyota, R. Fukuda, J. Hasegawa, M. Ishida, T. Nakajima, Y. Honda, O. Kitao, H. Nakai, T. Vreven, J. A. Montgomery, Jr., J. E. Peralta, F. Ogliaro, M. Bearpark, J. J. Heyd, E. Brothers, K. N. Kudin, V. N. Staroverov, R. Kobayashi, J. Normand, K. Raghavachari, A. Rendell, J. C. Burant, S. S. Iyengar, J. Tomasi, M. Cossi, N. Rega, J. M. Millam, M. Klene, J. E. Knox, J. B. Cross, V. Bakken, C. Adamo, J. Jaramillo, R. Gomperts, R. E. Stratmann, O. Yazyev, A. J. Austin, R. Cammi, C. Pomelli, J. W. Ochterski, R. L. Martin, K. Morokuma, V. G. Zakrzewski, G. A. Voth, P. Salvador, J. J. Dannenberg, S. Dapprich, A. D. Daniels, Ö. Farkas, J. B. Foresman, J. V. Ortiz, J. Cioslowski, D. J. Fox, Gaussian 09 Revision B.01, Gaussian Inc., Wallingford CT 2009.

[38] M. L. Laury, M. J. Carlson, A. K. Wilson, *J. Comput. Chem.* **2012**, *33*, 2380–2387.

[39] F. Hirsch, K. Pachner, I. Fischer, K. Issler, J. Petersen, R. Mitric, S. Bakels, A. M. Rijs, *ChemPhysChem* **2020**, *21*, 1515–1518.

[40] T. A. Cool, J. Wang, K. Nakajima, C. A. Taatjes, A. Mcllroy, *Int. J. Mass Spectrom.* **2005**, *247*, 18–27.

[41] M. Lang, PhD thesis, University of Wuerzburg, Wuerzburg, **2015**.

[42] W. Tsang, *Int. J. Chem. Kinet.* **1973**, *5*, 929–946.

[43] K. Brezinsky, F. L. Dryer, *Combust. Sci. Technol.* **1986**, *45*, 225–232.

[44] A. Lifshitz, M. Frenklach, A. Burcat, *J. Phys. Chem.* **1976**, *80*, 2437–2443.

[45] C. H. Wu, R. D. Kern, *J. Phys. Chem.* **1987**, *91*, 6291–6296.

[46] J. E. Rink, U. Boesl, *Eur. J. Mass Spectrom.* **2003**, *9*, 23–32.

[47] O. P. Haefliger, R. Zenobi, *Anal. Chem.* **1998**, *70*, 2660–2665.

[48] A. M. Rijs, N. Sändig, M. N. Blom, J. Oomens, J. S. Hannam, D. A. Leigh, F. Zerbetto, W. J. Buma, *Angew. Chem. Int. Ed.* **2010**, *49*, 3896–3900.

[49] A. M. Rijs, G. Ohanessian, J. Oomens, G. Meijer, G. von Helden, I. Compagnon, *Angew. Chem. Int. Ed.* **2010**, *49*, 2332–2335.

[50] A. M. Rijs, M. Kabeláč, A. Abo-Riziq, P. Hobza, M. S. de Vries, *ChemPhysChem* **2011**, *12*, 1816–1821.

[51] M. Schmitt, F. Spiering, V. Zhaunerchyk, R. T. Jongma, S. Jaeqx, A. M. Rijs, W. J. v. d. Zande, *Phys. Chem. Chem. Phys.* **2016**, *18*, 32116–32124.

[52] A. K. Lemmens, D. B. Rap, J. M. M. Thunnissen, S. Gruet, A. L. Steber, S. Panchagnula, A. G. G. M. Tielens, M. Schnell, W. J. Buma, A. M. Rijs, *J. Phys. Chem. Lett.* **2020**, *11*, 8997–9002.

[53] R. D. Brown, P. J. Domaille, J. E. Kent, *Aust. J. Chem.* **1970**, *23*, 1707–1720.

[54] Z. Pan, A. Puente-Urbina, A. Bodi, J. A. v. Bokhoven, P. Hemberger, *Chem. Sci.* **2021**, *12*, 3161–3169.

[55] D. Gregory, R. A. Jackson, P. J. Bennett, *Combust. Flame* **1999**, *118*, 459–468.

[56] W. R. Roth, F. Bauer, A. Beitat, T. Ebbrecht, M. Wüstefeld, *Chem. Ber.* **1991**, *124*, 1453–1460.

[57] R. S. Tranter, A. W. Jasper, J. B. Randazzo, J. P. A. Lockhart, J. P. Porterfield, *Proc. Combust. Inst.* **2017**, *36*, 211–218.

[58] L. V. Shevel'kova, V. G. Sokolovskaya, L. Y. Gusel'nikov, V. N. Guryshev, *Pet. Chem.* **1989**, *29*, 114–123.

[59] J. R. Schaefgen, *J. Polym. Sci.* **1955**, *15*, 203–219.

[60] M. B. Colket, D. J. Seery, *25th Symp. (Int.) Combust.* **1994**, *25*, 883–891.

[61] W. Yuan, Y. Li, P. Dagaut, J. Yang, F. Qi, *Combust. Flame* **2015**, *162*, 3–21.

[62] T. Zhang, L. Zhang, X. Hong, K. Zhang, F. Qi, C. K. Law, T. Ye, P. Zhao, Y. Chen, *Combust. Flame* **2009**, *156*, 2071–2083.

[63] J. A. Miller, S. J. Klippenstein, *J. Phys. Chem. A* **2003**, *107*, 7783–7799.

[64] J. A. Miller, C. F. Melius, *Combust. Flame* **1992**, *91*, 21–39.

[65] E. V. Shafir, I. R. Slagle, V. D. Knyazev, *J. Phys. Chem. A* **2003**, *107*, 8893–8903.

[66] R. S. Tranter, W. Tang, K. B. Anderson, K. Brezinsky, *J. Phys. Chem. A* **2004**, *108*, 3406–3415.

[67] L. D. Pfefferle, J. Boyle, G. Bermudez, *Prepr. Pap. - Am. Chem. Soc. Div. Fuel Chem.* **1991**, *36*, 1443.

[68] B. Alcaide, P. Almendros, C. Aragoncillo, *Chem. Soc. Rev.* **2010**, *39*, 783–816.

[69] D. Bakowies, *J. Chem. Theory Comput.* **2020**, *16*, 399–426.

[70] W. R. Roth, H.-W. Lennartz, E. Vogel, M. Leiendecker, M. Oda, *Chem. Ber.* **1986**, *119*, 837–843.

[71] H. A. Skinner, A. Snelson, *Trans. Faraday Soc.* **1959**, *55*, 404–407.

[72] E. J. P. Malar, F. Neumann, K. Jug, *J. Mol. Struct.* **1995**, *336*, 81–84.

[73] H. Hippler, S. Seisel, J. Troe, *25th Symp. (Int.) Combust.* **1994**, *25*, 875–882.

[74] P. Hemberger, A. Bodi, *Chimia* **2018**, *72*, 227–227.

[75] G. da Silva, E. E. Moore, J. W. Bozzelli, *J. Phys. Chem. A* **2009**, *113*, 10264–10278.

[76] P. Hemberger, A. J. Trevitt, T. Gerber, E. Ross, G. da Silva, *J. Phys. Chem. A* **2014**, *118*, 3593–3604.

[77] M. Kamphus, M. Braun-Unkhoff, K. Kohse-Höinghaus, *Combust. Flame* **2008**, *152*, 28–59.

[78] R. Sivaramakrishnan, J. V. Michael, *Proc. Combust. Inst.* **2011**, *33*, 225–232.

[79] K. Narayanaswamy, G. Blanquart, H. Pitsch, *Combust. Flame* **2010**, *157*, 1879–1898.

[80] G. Blanquart, P. Pepiot-Desjardins, H. Pitsch, *Combust. Flame* **2009**, *156*, 588–607.

[81] R. D. Smith, *J. Phys. Chem.* **1979**, *83*, 1553–1563.

CHAPTER 4

IR/UV DOUBLE RESONANCE STUDY OF THE 2-PHENYLALLYL RADICAL AND ITS PYROLYSIS PRODUCTS

This chapter is reproduced and partly adapted from

T. Preitschopf, F. Sturm, I. Stroganova, A. K. Lemmens, A. M. Rijs, I. Fischer, *Chem. Eur. J.* **2023**, *29*, e202202943

with permission from Wiley.

4.1 Abstract

Isolated 2-phenylallyl radicals (2-PA), generated by pyrolysis from a nitrite precursor, have been investigated by IR/UV ion dip spectroscopy using free electron laser radiation. 2-PA is a resonance-stabilized radical that is considered to be involved in the formation of polycyclic aromatic hydrocarbons (PAHs) in combustion, but also in interstellar space. The radical is identified based on its gas-phase IR spectrum. Furthermore, a number of bimolecular reaction products are identified, showing that the self-reaction as well as reactions with unimolecular decomposition products of 2-PA form several PAHs efficiently. Possible mechanisms are discussed and the chemistry of 2-PA is compared with the one of the related 2-methylallyl and phenylpropargyl radicals.

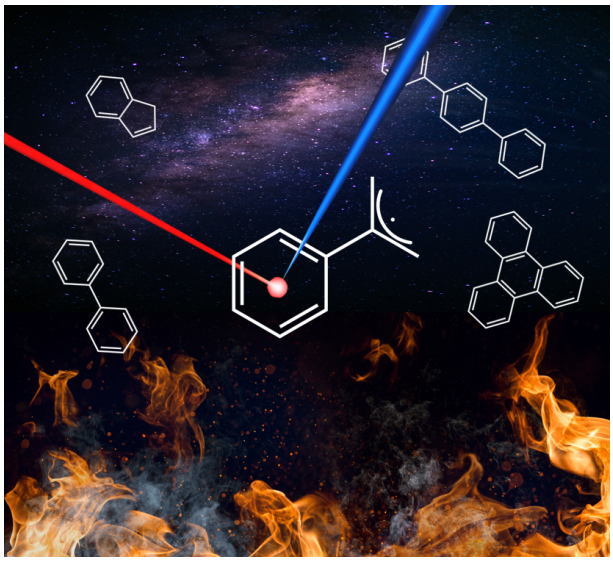

Figure 4.1. ToC graphic of published work on the high-temperature reactions of 2-phenylallyl radicals. Reproduced from Ref. [1] with permission from Wiley.

4.2 Introduction

To understand the formation of polycyclic aromatic hydrocarbons (PAHs) and soot is still a challenging task for chemistry. In high temperature processes, in particular combustion, one tries to avoid formation of these carcinogenic and environmentally harmful molecules as much as possible.[2,3] On the other hand, in astrochemistry PAHs are considered as likely carriers of the unidentified infrared bands (UIB),

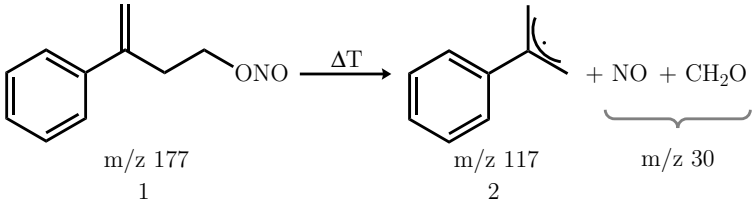

Scheme 4.1. Pyrolysis of 3-phenylbut-3-en-1-yl nitrite **1** is used to generate the 2-phenylallyl radical **2**. Adapted from Ref. [1] with permission from Wiley.

emission bands characteristic for aromatic molecules and PAHs.[4] The most important pathways to PAH formation have been reviewed recently,[5] among them the HACA (hydrogen abstraction C_2H_2 addition) and the PAC (phenyl addition (dehydro-)cyclization) mechanisms. However, almost all models agree on the central role of resonantly stabilized radicals (RSR) in the growth of aromatic species.[6] RSR can accumulate in reactive environments due to their lower reactivity towards O_2 and therefore be involved in secondary reactions.[7] Hence, the spectroscopic identification of RSR and the investigation of their chemistry is of considerable interest. Here, we focus on reactions of the 2-phenylallyl radical, **2** in Scheme 4.1, and compare its high temperature chemistry with the one of the related 2-methylallyl[8] and phenylpropargyl radicals.[9] While for its isomer 1-phenylallyl, a study of the $D_1 \leftarrow D_0$ transition by laser-induced fluorescence has been reported,[10,11] no spectroscopic information is available so far on **2**. Theoretical work is limited to studies on reactions of chemically activated C_9H_9 isomers.[12,13] This lack of information hampers *in situ* detection in reactive environments. Thus, laboratory experiments on isolated radicals under well-defined conditions are required to get more insight into the chemistry of RSR. Thermal reactions in pyrolysis microreactors are well suited to generate reactive molecules cleanly and at a sufficiently high number density to conduct gas-phase experiments.[14] The properties of such a microreactor were recently modeled using fluid dynamics simulations.[15] Depending on the mode of operation and the choice of parameters (backing gas pressure, length of the heated region and time delay between laser and gas pulse), such microreactors can be used to characterize isolated radicals, but also serve to initiate unimolecular and bimolecular chemical reactions.[15–17] In the present work we employed this technique to generate **2** from 3-phenylbut-3-en-1-yl nitrite (**1**), as visible in Scheme 4.1. Reaction products are often characterized by photoionization with tunable synchrotron radiation, either using the ionization energy (IE) derived from ion yields for identification[18–20] or photoelectron spectra.[21,22] IR/UV ion dip spectroscopy is an alternative tool to characterize reaction products, because it combines the structural sensitivity of infrared spectroscopy with mass information.[23] It is par-

ticularly well suited for the isomer-selective characterization of aromatic molecules and PAHs, which generally absorb in the UV. Recently, we employed IR/UV spectroscopy to record IR spectra of isolated RSR with relevance to combustion and to monitor their chemical reactions, among them phenylpropargyl,[9] benzyl,[24] *ortho*-benzyne[25] and 2-methylallyl.[8] In contrast, small molecules without a UV chromophore are difficult to detect by IR/UV, thus complementary photoionization data are helpful, as shown for the *ortho*-benzyne self-reaction.[25] As an alternative to pyrolysis, electrical discharges have been employed to generate RSR and follow their chemistry. Recently, a discharge of naphthalene has been utilized to study the formation of PAHs by IR/UV spectroscopy.[26]

4.3 Experimental

The experiments were carried out at the FELIX free electron laser laboratory[27] at the Radboud University, Nijmegen, The Netherlands. 2-phenylallyl (**2**) was generated by flash pyrolysis from 3-phenylbut-3-en-1-yl nitrite (**1**), see Scheme 4.1. The nitrite precursor, synthesized from but-3- yn-1-ol according to literature[28,29] (see Figure S20 in Appendix B), was heated to 115-125 °C in an in-vacuum molecular beam source, seeded in 2.5 bar of argon, and expanded into a differentially pumped vacuum apparatus[23] using a solenoid valve (Series 9, Parker General Valve) pulsed at 20 Hz. The latter was equipped with a resistively heated SiC tube (length: 40 mm, ∅: 1.0 mm, heated region: 10 mm) with a pyrolysis temperature of around 800 K to generate **2** and record its IR spectrum.[14] Subsequently, the temperature was increased to around 1000 K to promote further chemical reactions of **2** in the microreactor.[15–17] In the resulting free jet, molecules are adiabatically cooled to approximately room temperature. The jet was skimmed and crossed by perpendicular UV light and counterpropagating FEL-IR radiation in the interaction region of a reflectron time-of-flight mass spectrometer (R. M. Jordan Co.).[23] The UV light was provided by an unfocused Nd:YAG-laser pumped dye laser (Lioptec, operated at 20 Hz) followed by frequency doubling to perform [1+1]-REMPI at 270 nm (∼1.5 mJ/pulse). To record IR/UV spectra[23] of the pyrolytically generated species, FELIX[27] was set around 200 ns prior to the UV laser and operated at 10 Hz to obtain alternating IR-OFF/IR-ON ion yields in the range of 560-1600 cm^{-1} in steps of 2 cm^{-1}. Note that FELIX (10 μs pulse) typically exhibits a bandwidth of around 1 % of the central photon frequency with an output power of up to 150 mJ/pulse in the MIR region. The resulting mass-selected IR spectra were obtained by dividing the IR-OFF ion signal by the IR-ON ion signal, taking the decadic logarithm, correcting for IR laser power, averaging

over several scans, and using digital Savitzky-Golay filtering. The experimental details for recording the TPE spectrum of **2** using synchrotron radiation are given in Appendix B.

The spectra were compared to harmonic vibrational DFT calculations at the B3LYP/6-311++G** level of theory[30] using the GAUSSIAN16 computational chemistry software.[31] All computed spectra were scaled with an empirical factor of 0.985, which is in the range of values recommended by previous benchmark studies,[32] and convolved with a Gaussian-shaped function (FWHM=24 cm^{-1}). Computations of standard heat of reactions of possible reactions occurring in the reactor as well as ionization energies were likewise performed at the DFT/B3LYP/6-311++G** level of theory. The relative Gibbs energies at 300 K and 1000 K of the structural isomers were computed at the same theoretical level employing the ORCA 5.0 software package.[33]

4.4 Results

4.4.1 Mass spectra

SPI TOF-MS. The single-photon ionization (SPI) time-of-flight mass spectrum of the pyrolysis products of **1**, recorded using synchrotron radiation at the Swiss Light Source (SLS), is presented in Figure 4.2a. The spectrum gives an approximate distribution of the relative molecular concentrations in the jet.[34,35] At around 800 K, an almost complete conversion of **1** (m/z 177) and a relative intense signal at m/z 117, corresponding to the mass of **2**, are observed. In addition, a small signal is visible at m/z 30 due to NO, confirming the decomposition shown in Scheme 4.1. Contributions of formaldehyde (CH_2O) can be excluded due to its high IE.[36] Addition of an H atom to **2** leads to the most dominant peak at m/z 118, while H atom loss results in m/z 116. Dimerization of **2** is evident from the signal at m/z 234. Several further signals such as m/z 78, 92, or 104, indicate that small aromatics are formed in the unimolecular decomposition of **2** and might contribute to the formation of higher (polycyclic) aromatic hydrocarbons as suggested by m/z 128 or 154. Further mass spectra with and without pyrolysis are given in Figure S12 in Appendix B.

REMPI TOF-MS. Figure 4.2b depicts the [1+1]-REMPI mass spectrum at around 1000 K. The higher pyrolysis temperature was chosen to promote bimolecular reactions in the microreactor.[15–17] At the excitation wavelength of 270 nm (4.59 eV), many PAH possess absorption bands,[37,38] that lead to enhanced signal

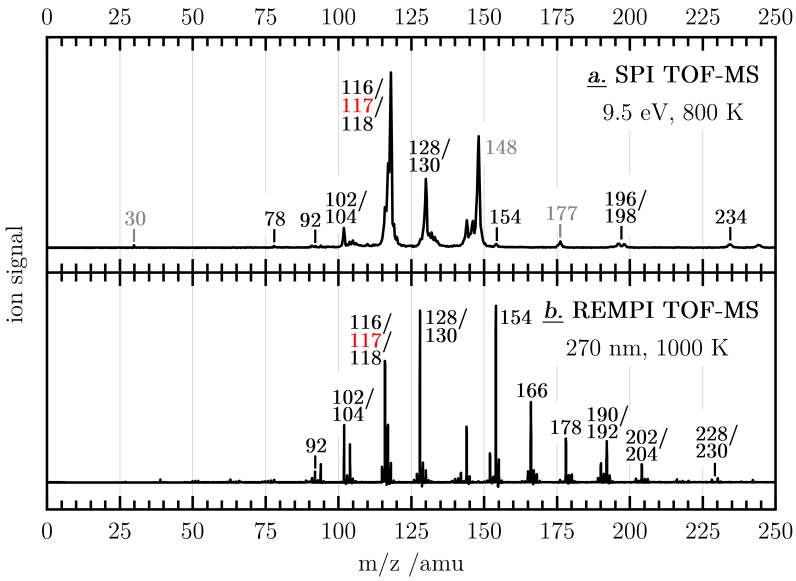

Figure 4.2. Time-of-flight mass spectra (TOF-MS) of **1** with pyrolysis recorded at 9.5 eV in a single-photon ionization process (SPI) at T_{pyro} around 800 K (trace a) and at 270 nm (4.59 eV) in a [1+1]-REMPI process at T_{pyro} around 1000 K (b). Adapted from Ref. [1] with permission from Wiley.

intensities in comparison with the SPI spectrum (see for instance m/z 92, 104, 116, 128, or 154). Commonly, the strong $S_3 \leftarrow S_0$ and/or the medium strong $S_2 \leftarrow S_0$ transitions of the vast majority of PAH lie around this wavelength region.[38] Hence, excitation around 270 nm is ideal to monitor a large number of aromatic high-temperature reaction products. In addition, sufficient absorption of **2** at this wavelength is secured (see Figure S13). In comparison with the SPI TOF-MS (trace a), higher masses are visible due to the high sensitivity of resonant photoionization.[38] Note, that the mass-to-charge ratio of many of the peaks differs by 76 amu in comparison with signals at lower m/z (*e.g.*, m/z 102 and 178, 116 and 192, 128 and 204, 154 and 230). This indicates that molecular growth is dominated by addition of phenyl radicals (accompanied with a loss of an H atom), which is followed by dehydrocyclization (H_2 loss) as suggested by the signals at m/z 190 and 192, 202 and 204, 228 and 230.

The corresponding REMPI excitation spectra (260−280 nm) recorded at a pyrolysis temperature of 1000 K exhibit unstructured and broadened UV features due to overlapping bands of the pyrolysis products,[23] which impedes isomer identification. Note that the molecules are cooled in the jet expansion, but possibly to room temperature only.

4.4.2 IR/UV spectra

In the following section, we present mass-selected IR/UV spectra in combination with quantum chemical calculations of vibrational spectra, that allow to unambiguously identify the mass signals observed in the REMPI TOF-MS (*cf.* Figure 4.2b). Several additional spectra are presented in Appendix B. The width of the vibrational absorption bands is mostly determined by power broadening owing to the intense IR radiation and the rotational temperature of the pyrolysis products. Most reaction products are present in the temporal center of the gas pulse, where rotational cooling is less effective. Note, that narrow electronic transitions are not crucial to obtain an ion depletion signal, since IR excitation can result in large variations of the UV absorption cross section even for broad bands.[39–41] Additionally, the high IR intensity facilitates absorption of further IR photons, possibly leading to fragmentation.[42] As absorption of the first IR photon remains the bottleneck for the process, ground state IR spectra are obtained.

m/z 117 and 118. Figure 4.3a presents the IR/UV spectrum of m/z 117 obtained from pyrolysis of **1** (see Scheme 4.1) at around 800 K. A depletion of 15-20 % was observed for the most dominant band at 721 cm^{-1}. The wavenumber of the peak centre was determined using Gaussian fitting. The band is well represented in the computed IR spectrum of **2** (trace b) and is assigned to the aryl C−H out-of-plane wagging vibration. Two further distinct bands are identified at 767 and 786 cm^{-1}, originating from an out-of-plane wagging mode and the symmetric CH_2 out-of-plane bending vibration. Note, that the latter is in excellent agreement with the wavenumber of the CH_2 out-of-plane bending mode of the related 2-methylallyl radical.[8] Several further bands of smaller and medium intensity are predicted in the higher wavenumber region by the computation, but are difficult to identify in the experimental spectrum due to the low S/N ratio. To exclude (partial) isomerization of **2** in the microreactor, the experimental data are compared to computed IR spectra of the *E*- and *Z*-1-phenylallyl radical (see Figure S14 in Appendix B). A disagreement is evident.

A threshold photoelectron spectrum (TPES) of **2**, recorded at the SLS, is given in Figure S15. The spectrum is broad and unstructured due to the large geometry change upon ionization (see Figure S16). It is therefore only discussed in Appendix B. Here, we just note that an adiabatic IE of 7.6±0.1 eV has been determined.

The mass signal at m/z 118 (Figure 4.2b) already indicates addition of an H atom to **2**. The corresponding experimental and computed IR spectra (see Figure 4.3c and d) confirm the formation of α-methylstyrene (C_9H_{10}). The absence

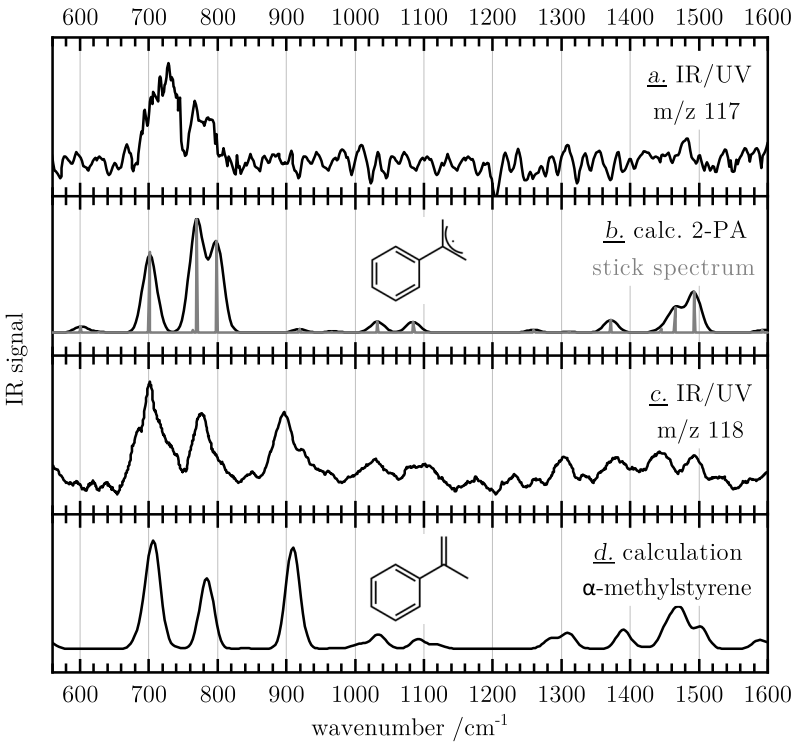

Figure 4.3. The IR/UV spectrum of m/z 117 (trace a) is assigned to **2** based on comparison with a computed spectrum (b). Addition of an H atom leads to the formation of α-methylstyrene as shown in traces c and d. Adapted from Ref. [1] with permission from Wiley.

of the band at around 900 cm^{-1} in trace a rules out that the signal of m/z 117 originates from dissociative photoionization of m/z 118, with its otherwise rather similar IR spectrum.

m/z 228 and 230. The peak at m/z 230 is one of the most interesting signals in the REMPI TOF-MS (Figure 4.2b) as it corresponds to direct dimerization of **2** to m/z 234 (see Figure 4.2a) followed by dehydrocyclization, a pattern previously observed for 2-methylallyl radicals.[8] Based on comparison with computed IR spectra of terphenyl isomers (Figure 4.4d-f), the corresponding IR/UV spectrum (Figure 4.4c) is best represented by *p*-terphenyl ($C_{18}H_{14}$) in terms of the energetic positions and relative intensities of the vibrational bands. In particular, the characteristic band at 842 cm^{-1}, the C−H out-of-plane wagging vibration of the central aromatic ring, is only present in the computed spectrum of *p*-terphenyl. The formation of *m*-terphenyl is excluded by the computed band at 621 cm^{-1}, which is absent in the experimental spectrum, while contributions of *o*-terphenyl

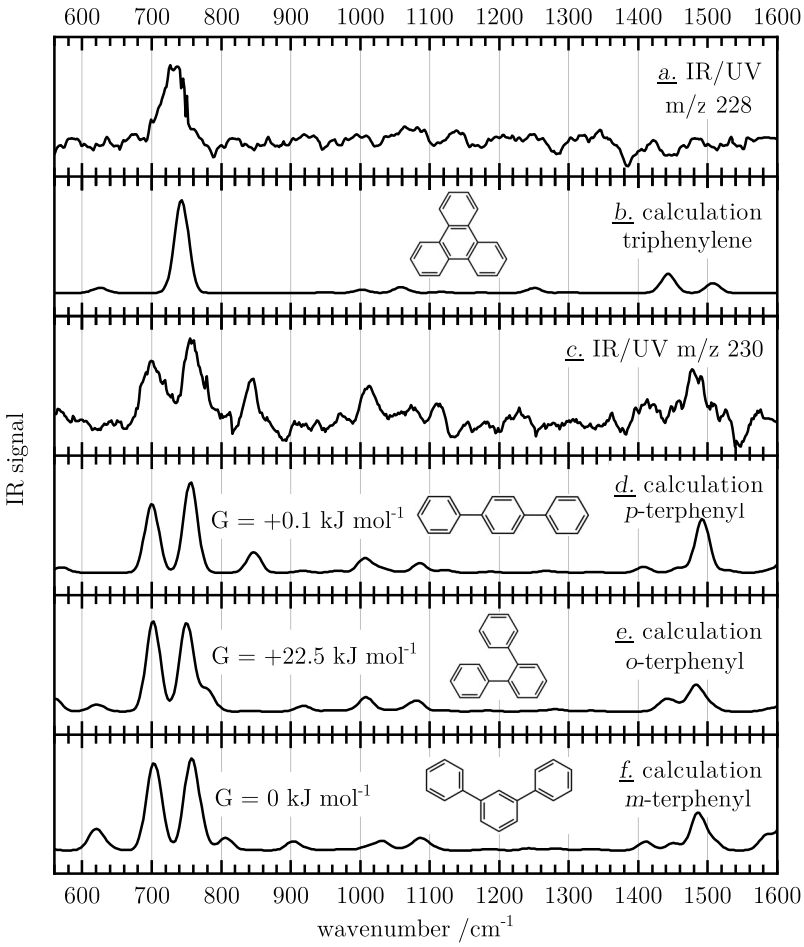

Figure 4.4. The IR/UV spectrum of m/z 228 (trace a) is due to triphenylene (b), whereas the one of m/z 230 (c) is dominated by p-terphenyl (d). Contributions of the thermochemically less stable *ortho* isomer (e) are small at best and conclusively presumed by the generation of triphenylene. Adapted from Ref. [1] with permission from Wiley.

are small at best. Note, that the latter is slightly higher in energy than *p*- and *m*-terphenyl which are almost degenerate and constitute the lowest energy structures at 1000 K. Interestingly, the *para* isomer was also observed as a dimerization product of phenylpropargyl radicals.[9]

The IR/UV spectrum of m/z 228 (Figure 4.4a) is readily assigned to triphenylene ($C_{18}H_{12}$, trace 4.4b) by the small number of vibrational transitions due to the high symmetry (D_{3h}) and its distinctive C−H out-of-plane wagging vibration (in-phase) at 731 cm^{-1}. The observation of triphenylene suggests the formation of

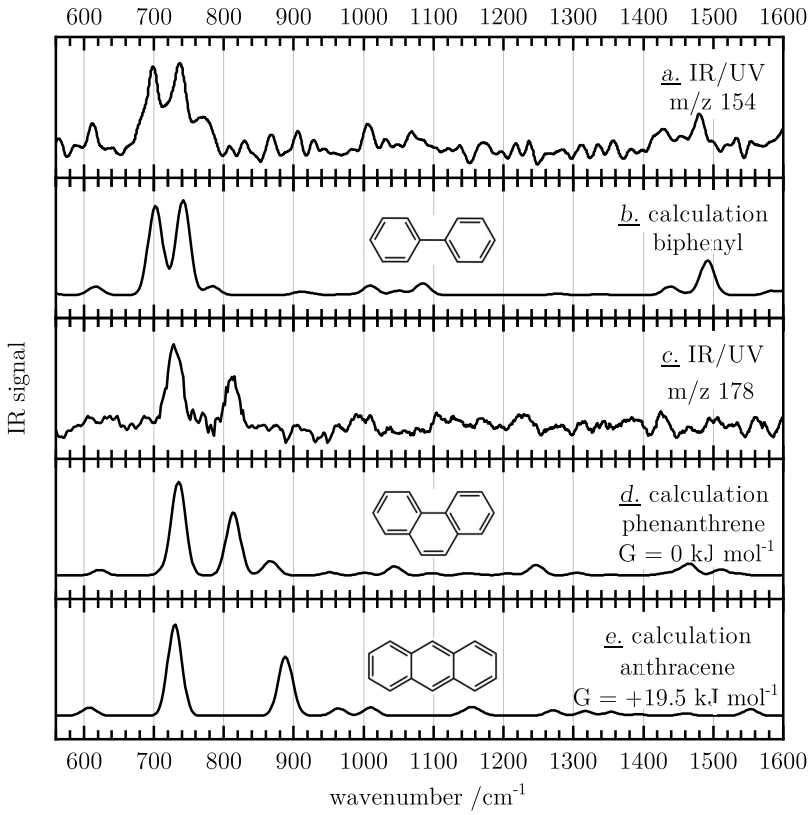

Figure 4.5. The carrier of the IR/UV spectrum of m/z 154 is identified as biphenyl (traces a and b). M/z 178 (c) is assigned to the thermochemically more stable phenanthrene (d). Adapted from Ref. [1] with permission from Wiley.

o-terphenyl as an intermediate, followed by dehydrocyclization (-H_2) into the more stable condensed PAH.[5,43]

m/z 154 and 178. Phenyl chemistry in the microreactor is further indicated by the spectrum of m/z 154 (Figure 4.5a). In addition to the characteristic C−H out-of-plane bending vibrations at 699, 736, and 767 cm^{-1}, the spectrum exhibits several further features, for example, at 612 or 1480 cm^{-1}, that permit an unambiguous assignment to biphenyl ($C_{12}H_{10}$, trace 4.5b).

The mass-selected IR/UV spectrum of m/z 178 (Figure 4.5c) displays the formation of phenanthrene ($C_{14}H_{10}$), as the two dominant bands at 730 and 812 cm^{-1} are in excellent agreement with the computed spectrum (trace 4.5d). Contributions of the thermochemically less stable isomer anthracene are ruled out by the absence of its prominent C−H out-of-plane wagging vibration at 889 cm^{-1} in the spectrum (trace 4.5e).

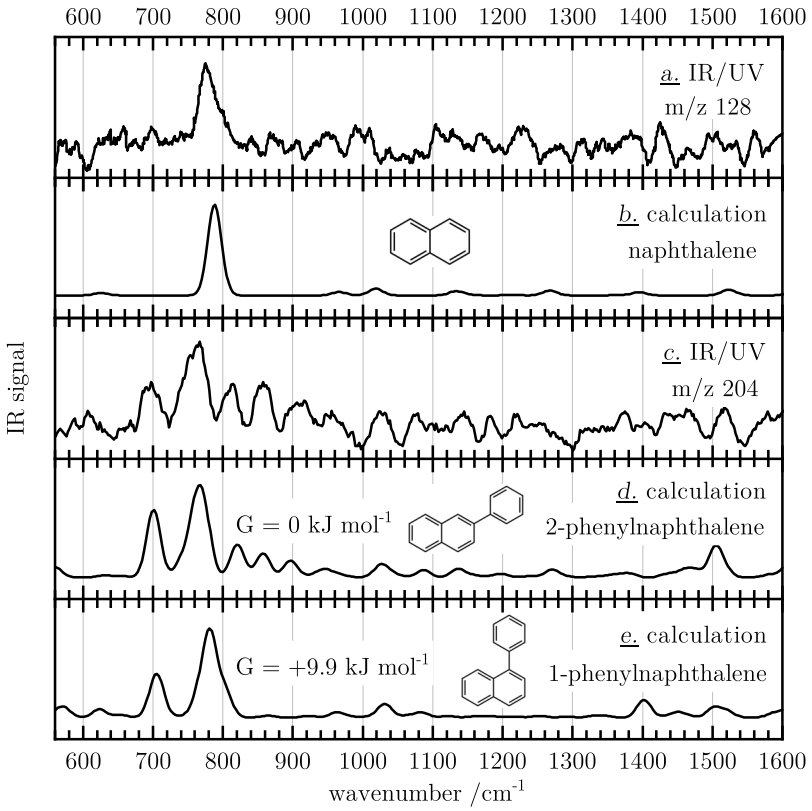

Figure 4.6. The structural information of the IR/UV spectrum of m/z 128 facilitates unambiguous assignment of naphthalene (traces a and b). The IR/UV spectrum of m/z 204 (c) is best represented by the thermochemically more stable 2-phenylnaphthalene (d). Adapted from Ref. [1] with permission from Wiley.

m/z 128 and 204. Based on comparison with a computed IR spectrum, the IR/UV spectrum of m/z 128 (Figure 4.6a) is dominated by the characteristic C−H out-of-plane wagging vibration (in-phase) at 779 cm^{-1} of naphthalene ($C_{10}H_8$, trace 4.6b). No further vibrational bands are observed in the spectrum, so the PAH is readily assigned as the only carrier of m/z 128.

The mass signal at m/z 204 in the REMPI TOF-MS (*cf.* Figure 4.2b) is closely related to m/z 128 as both peaks are separated by 76 amu. This suggests the addition of a phenyl radical to naphthalene, resulting in the formation of the two possible isomers 1- and 2-phenylnaphthalene ($C_{16}H_{12}$). A comparison of the corresponding IR/UV spectrum (Figure 4.6c) with the computed IR spectrum (trace 4.6d) verifies the generation of 2-phenylnaphthalene in the reactor, as spacing and relative intensities of the most intense out-of-plane wagging vibrations between 670 to 940 cm^{-1} agree well. Formation of the thermochemically less sta-

ble 1-phenylnaphthalene is unlikely, because the most dominant band at 782 cm^{-1} is predicted at higher wavenumbers (trace 4.6e) compared with the predominant band of 2-phenylnaphthalene (shift ∼15 cm^{-1}).

Additional observed masses. Several further mass signals were assigned based on the IR/UV spectra shown in Appendix B. Among them are m/z 102 and 104 identified as phenylacetylene and styrene (see Figure S17), m/z 116 assigned to indene (Figure S18), and m/z 166 identified as fluorene (Figure S19).

4.5 Discussion

Three key reactions of **2** are involved in molecular growth as summarized in Scheme 4.2. At around 800 K, the radical selfreaction, **A** in Scheme 4.2, sets in as apparent from the mass peak at m/z 234 in the SPI TOF-MS (Figure 4.2a). A heat of reaction $\Delta_R H^0 = -193$ kJ·mol^{-1} was computed for the exothermic reaction. The reaction product 2,5-diphenyl-1,5-hexadiene (**3**) with a computed IE of 7.46 eV was not identified by IR/UV ion dip spectroscopy, possibly due to a low UV absorption cross section at the excitation wavelength. However, its formation is concluded from the formation of *p*-terphenyl (m/z 230), see Figure 4.4c. The latter is most likely formed in a Cope rearrangement of **3** *via* a cyclic, diradical intermediate followed by aromatization as suggested in theoretical studies.[44,45] A $\Delta_R H^0 = -45$ kJ·mol^{-1} was computed for the reaction that is accompanied by the entropically favorable loss of two hydrogen molecules.

At around 1000 K, dimerization competes with unimolecular decomposition of **2** to a phenyl radical and likely allene, see reaction **B** in Scheme 4.2 ($\Delta_R H^0 = +222$ kJ·mol^{-1}). The presence of significant amounts of phenyl in the microreactor is evident as several reaction products identified by IR/UV ion dip spectroscopy exhibit phenyl groups. Some examples are biphenyl or 2-phenylnaphtalene, which highlight the prevailing role of phenyl chemistry in the reactor. While allene has not been detected in the SPI TOF-MS (Figure 4.2a) due to its high IE,[46] its formation in **B** was predicted in theoretical work on reactions of chemically activated C_9H_9 isomers.[13] The reverse reaction of **B** was computed to proceed with a barrier of just +18 kJ·mol^{-1}.[13]

Further pressure and temperature dependent dissociation reactions of **2** on the C_9H_9 PES were characterized by Vereecken and Peeters.[12] Decomposition to indene (C_9H_8) + H was predicted as a dominant product along with additional exit channels, for example leading to phenylacetylene (C_8H_6) + CH_3. Both aromatics are identified in our study too, see Figure S18 and S17 in Appendix B. Furthermore, the reaction of allene with phenyl has also been observed to form indene in

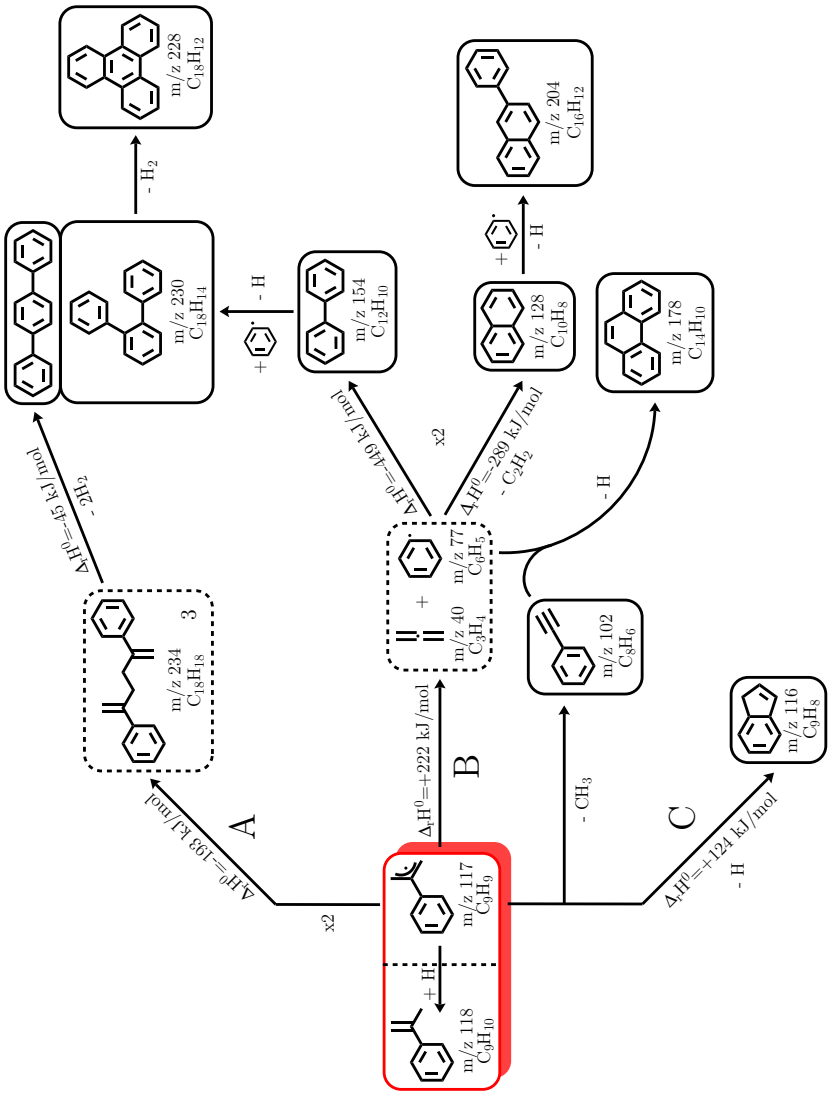

Scheme 4.2. High temperature reaction products of **2** in a flow microreactor identified by IR/UV ion dip spectroscopy (in black). Molecules in dashed boxes are suggested to be formed based on mass spectrometry (*cf.* Figure 4.2) and reported literature, see Ref. [13]. Adapted from Ref. [1] with permission from Wiley.

a VUV photoionization study.[47] The reaction was proposed to either proceed via **2** (reverse reaction of **B**) or a second resonantly stabilized C_9H_9 radical.[13,47] The observation of indene is of considerable interest, as it is among the few PAH that have been identified unambiguously in interstellar space.[48]

In addition to the self-recombination reaction **A**, the reaction with phenyl radicals formed in **B** provides another efficient pathway for molecular growth at high

temperature, known as the PAC mechanism.[49] Here, addition of a phenyl radical to an aromatic hydrocarbon is followed by successive dehydrogenation, cyclization and aromatization. The mechanism was already indicated by the pattern of the mass peaks in the REMPI TOF-MS (cf. Figure 4.2b) and is further substantiated by the identification of biphenyl (m/z 154), terphenyl (m/z 230), and triphenylene (m/z 228), see Figure 4.5 and Figure 4.4a. Preferentially, phenyl will add at the bay position of biphenyl.[5] The latter is itself a product of the self-reaction of phenyl.[50] Additionally, the disproportionation products of the phenyl selfreaction, benzene and *o*-benzyne,[51] might also contribute to the formation of biphenyl,[52] as the presence of benzene is suggested by the mass signal at m/z 78 in the SPI TOF-MS (*cf.* Figure 4.2a).

After phenyl addition, *o*-terphenyl could be formed by loss of an H atom.[5] However, the IR/UV spectrum of m/z 230 is clearly dominated by *p*-terphenyl, see Figure 4.4c-f. This is in agreement with a recent photoionization study by Zhao *et al.*, who investigated the mechanism of the reaction of phenyl with biphenyl.[53] Yet, the formation of triphenylene (m/z 228, Figure 4.4a) will proceed via dehydrogenation and cyclization of *o*-terphenyl,[43,53] and thus likely accounts for its absence in the spectrum. A rapid conversion of the latter is further suggested thermochemically as *o*-terphenyl is slightly higher in energy than *p*- and *m*-terphenyl at 1000 K (*cf.* Figure 4.4). Although phenyl addition at the bay position is favored,[5] minor contributions to *p*-terphenyl by PAC are expected in addition to reaction **A**, since the initial addition reaction is also possible in the *para* position of the phenyl moiety of biphenyl.[43] Addition in the *meta* position is less likely due to a low electron density as known for aromatic radical substitution reactions,[43,54] explaining the absence of *m*-terphenyl in the IR/UV spectrum (see Figure 4.4c).

The identification of 2-phenylnaphthalene (*cf.* Figure 4.6c) further indicates efficient mass growth via PAC. Phenyl can add to the C1 or C2 carbon atom of naphthalene with computed $\Delta_R H^0 = -137$ and -116 kJ·mol^{-1} respectively, yielding 1- and 2- phenylnaphthalene after loss of H atom.[53] In our study, only the thermochemically more stable 2-substituted isomer is identified (Figure 4.6). Interestingly, naphthalene (m/z 128, Figure 4.6a) further reflects the dominant phenyl chemistry occurring in the reactor, as it can be formed by two phenyl units in a radical/π-bond addition reaction according to Equation (4.1):[52,55]

$$2\ C_6H_5 \longrightarrow C_{10}H_8 + C_2H_2,\ \Delta_R H^0 = -298\ \text{kJ·mol}^{-1} \tag{4.1}$$

Furthermore, the reaction of propargyl (m/z 39) with a benzyl radical (m/z 91),[56] as well as the self-reaction of the cyclopentadienyl radical (m/z 65),[57] are known

as primary routes for the formation of naphthalene. However, as neither m/z 39 nor 65 or 91 are observed in the TOF-MS (Figure 4.2) naphthalene formation via Equation (4.1) is most likely.

The generation of phenanthrene (m/z 178, Figure 4.5c) in combustion processes is expected to proceed *via* the acetylene-based HACA mechanism from biphenyl.[58,59] Furthermore, the addition of phenyl to phenylacetylene (see Figure S17 in Appendix B) *via* four-membered ring intermediates as a variation of the PAC mechanism[43,60] was reported as another efficient route.[61] Recently, the route was predicted to preferentially proceed *via* the formation of 2-ethynylbiphenyl by PAC, followed by H-assisted isomerization to phenanthrene.[62] Considering the significant amounts of phenyl in the reactor, this reaction is expected to occur. The less stable isomer anthracene has not been observed (see Figure 4.5c). This indicates that the PAH formation under the present conditions is mostly driven thermodynamically and the product with the lowest Gibbs energy is preferentially formed.

Recently, we investigated the high temperature chemistry of the 2-methylallyl (2-MA)[8] and 1- and 3-phenylpropargyl radicals (PPR)[9] in a microreactor. While 2-MA exhibits a methyl group instead of phenyl, PPR and **2** are composed of three C_3 units that play an important role in the formation of aromatic hydrocarbons.[63] Due to their close relation, similar reactions of the radicals are expected to be involved in molecular growth and thus are compared in the following.

Related to the work described here, unimolecular decomposition of 2-MA to methyl and allene (rather than phenyl and allene) has been observed as a key reaction to yield building blocks involved in the formation of larger aromatics.[8] Several reaction products were connected by addition of methyl groups, which suggests that methylation in the high temperature chemistry of 2-MA parallels the reactions observed in the present work.[8] While allene was experimentally identified by previous TPES work,[64] its formation due to **B** in the present study (see Scheme 4.2) was predicted by theoretical work[13] and is indirectly concluded from the various reaction products with phenyl groups. Interestingly, a preferential addition of methyl and phenyl to naphthalene at the C2 carbon atom was found in both studies, indicating that formation of the 2-substituted naphthalene isomer is favored over its 1-substituted counterpart at high temperature.[8]

While dimerization of **2** is evident from the mass signal at m/z 234 in the SPI TOF-MS (Figure 4.2a), the recombination product of 2-MA was not observed in the TOF mass spectra,[8] but has been reported in previous work.[65] Yet, its formation was suggested by the generation of *p*-xylene *via* dehydrocyclization ($-H_2$)

and aromatization ($-H_2$) of the latter.[8] A similar mechanism presumably leads to the formation of *p*-terphenyl starting from **3** in this work, see Scheme 4.2.

Interestingly, the self-reaction of 1- and 3-PPR[9] (C_9H_7, m/z 115) also leads to a predominant formation of *p*-terphenyl. Both radicals, **2** and PPR, efficiently form m/z 228, but different carriers of the mass signal have been identified in the two studies. **2** results in the formation of triphenylene (Figure 4.4a), while for both PPR isomers the m/z 228 product was assigned to 1-phenylethynyl naphthalene (1-PEN).[9,66] The selectivity of the self-reaction was traced back to a resonance stabilization of the radical positions.[9] In contrast to **2**, no decomposition of PPR to phenyl radicals has been observed. This might partly be traced to the greater stability of 1-PPR by 34.1 kJ·mol^{-1} and of 3-PPR by 24.6 kJ·mol^{-1} relative to **2**.[10]

Furthermore, indene has been detected as a reaction product of PPR and is also observed here. Its formation from both radicals requires an initial isomerization. In PPR isomerization to indenyl is followed by addition of an H atom,[9] while loss of an H atom follows isomerization in **2**, as computed.[12] The formation of indene in both cases demonstrates the high stability of the molecules.

4.6 Conclusions

The chemistry of the resonance-stabilized 2-phenylallyl radical (2-PA) in a high-temperature microreactor was investigated by IR/UV ion dip spectroscopy in a free jet using free electron laser radiation. 2-PA is considered as a potential intermediate in the formation of polycyclic aromatic hydrocarbons (PAHs) at high temperature in combustion processes but might also be relevant in interstellar space. The radical was generated from a nitrite precursor and identified by its gas-phase IR spectrum in the fingerprint region. Several reaction products were also identified from their IR spectra with the aid of DFT computations, showing that uni- and bimolecular reactions of 2-PA contribute to molecular growth. In particular, three competing reactions of 2-PA were found to contribute to PAH formation. First, the radical self-reaction directly forms *p*-terphenyl. Such self-reactions often proceed barrierless and are thus promising pathways also for molecular growth in interstellar space. Second, unimolecular decomposition of 2-PA to allene and a phenyl radical produces the building blocks for PAH formation *via* the PAC mechanism (phenyl addition (dehydro-)cyclization) at high temperature. This pathway is evident from the identification of the reaction products biphenyl, terphenyl and triphenylene. Third, isomerization followed by H abstraction was computed to form indene.[13] In all pathways, the thermodynamically favored isomer is formed. Furthermore, the high temperature chemistry was compared with the one of the 2-methylallyl and phenylpropargyl radicals, highlighting the similarities and differences in the high-temperature chemistry of the chemically related radicals.

References

[1] T. Preitschopf, F. Sturm, I. Stroganova, A. K. Lemmens, A. M. Rijs, I. Fischer, *Chem. Euro. J.* **2023**, *29*, e202202943.

[2] A. M. Mastral, M. S. Callén, *Environ. Sci. Technol.* **2000**, *34*, 3051–3057.

[3] H. Richter, V. Risoul, A. L. Lafleur, E. F. Plummer, J. B. Howard, W. A. Peters, *Environ. Health Persp.* **2000**, *108*, 709–717.

[4] A. M. Ricks, G. E. Douberly, M. A. Duncan, *Astrophys. J.* **2009**, *702*, 301–306.

[5] R. I. Kaiser, N. Hansen, *J. Phys. Chem. A* **2021**, *125*, 3826–3840.

[6] K. O. Johansson, M. P. Head-Gordon, P. E. Schrader, K. R. Wilson, H. A. Michelsen, *Science* **2018**, *361*, 997–1000.

[7] T. Schmidt, *Int. Rev. Phys. Chem.* **2016**, *35*, 209–242.

[8] T. Preitschopf, F. Hirsch, A. K. Lemmens, A. M. Rijs, I. Fischer, *Phys. Chem. Chem. Phys.* **2022**, *24*, 7682–7690.

[9] K. H. Fischer, J. Herterich, I. Fischer, S. Jaeqx, A. M. Rijs, *J. Phys. Chem. A* **2012**, *116*, 8515–8522.

[10] T. P. Troy, N. Chalyavi, A. S. Menon, G. D. O'Connor, B. Fückel, K. Nauta, L. Radom, T. W. Schmidt, *Chem. Sci.* **2011**, *2*, 1755–1765.

[11] J. A. Sebree, N. M. Kidwell, E. G. Buchanan, M. Z. Zgierski, T. S. Zwier, *Chem. Sci.* **2011**, *2*, 1746–1754.

[12] L. Vereecken, J. Peeters, H. F. Bettinger, R. I. Kaiser, P. v. R. Schleyer, H. F. Schaefer, *J. Am. Chem. Soc.* **2002**, *124*, 2781–2789.

[13] L. Vereecken, J. Peeters, *Phys. Chem. Chem. Phys.* **2003**, *5*, 2807–2817.

[14] D. W. Kohn, H. Clauberg, P. Chen, *Rev. Sci. Instrum.* **1992**, *63*, 4003–4005.

[15] Q. Guan, K. N. Urness, T. K. Ormond, D. E. David, G. Barney Ellison, J. W. Daily, *Int. Rev. Phys. Chem.* **2014**, *33*, 447–487.

[16] A. Vasiliou, M. R. Nimlos, J. W. Daily, G. B. Ellison, *J. Phys. Chem. A* **2009**, *113*, 8540–8547.

[17] A. M. Scheer, C. Mukarakate, D. J. Robichaud, G. B. Ellison, M. R. Nimlos, *J. Phys. Chem. A* **2010**, *114*, 9043–9056.

[18] F. Zhang, R. I. Kaiser, A. Golan, M. Ahmed, N. Hansen, *J. Phys. Chem. A* **2012**, *116*, 3541–3546.

[19] D. S. N. Parker, R. I. Kaiser, B. Bandyopadhyay, O. Kostko, T. P. Troy, M. Ahmed, *Angew. Chem. Int. Ed.* **2015**, *54*, 5421–5424.

[20] D. S. N. Parker, R. I. Kaiser, T. P. Troy, M. Ahmed, *Angew. Chem. Int. Ed.* **2014**, *53*, 7740–7744.

[21] P. Hemberger, A. Bodi, *Chimia* **2018**, *72*, 227–227.

[22] I. Fischer, S. T. Pratt, *Phys. Chem. Chem. Phys.* **2022**, *24*, 1944–1959.

[23] A. M. Rijs, J. Oomens, *Top. Curr. Chem.* **2014**, *364*, 1–42.

[24] F. Hirsch, P. Constantinidis, I. Fischer, S. Bakels, A. M. Rijs, *Chem. Eur. J.* **2018**, *24*, 7647–7652.

[25] F. Hirsch, E. Reusch, P. Constantinidis, I. Fischer, S. Bakels, A. M. Rijs, P. Hemberger, *J. Phys. Chem. A* **2018**, *122*, 9563–9571.

[26] A. K. Lemmens, D. B. Rap, J. M. M. Thunnissen, B. Willemsen, A. M. Rijs, *Nat. Commun.* **2020**, *11*, 269.

[27] D. Oepts, A. F. G. van der Meer, P. W. van Amersfoort, *Infrared Phys. Technol.* **1995**, *36*, 297–308.

[28] C. Shu, R. S. Mega, B. J. Andreassen, A. Noble, V. K. Aggarwal, *Angew. Chem. Int. Ed.* **2018**, *57*, 15430–15434.

[29] M. Gasser, J. A. Frey, J. M. Hostettler, A. Bach, *Chem. Commun.* **2010**, *47*, 301–303.

[30] R. Krishnan, J. S. Binkley, R. Seeger, J. A. Pople, *J. Chem. Phys.* **1980**, *72*, 650–654.

[31] M. J. Frisch, G. W. Trucks, H. B. Schlegel, G. E. Scuseria, M. A. Robb, J. R. Cheeseman, G. Scalmani, V. Barone, G. A. Petersson, H. Nakatsuji, X. Li, M. Caricato, A. V. Marenich, J. Bloino, B. G. Janesko, R. Gomperts, B. Mennucci, H. P. Hratchian, J. V. Ortiz, A. F. Izmaylov, J. L. Sonnenberg, D. Williams-Young, F. Ding, F. Lipparini, F. Egidi, J. Goings, B. Peng, A. Petrone, T. Henderson, D. Ranasinghe, V. G. Zakrzewski, J. Gao, N. Rega, G. Zheng, W. Liang, M. Hada, M. Ehara, K. Toyota, R. Fukuda, J. Hasegawa, M. Ishida, T. Nakajima, Y. Honda, O. Kitao, H. Nakai, T. Vreven, K. Throssell, J. A. Montgomery, Jr., J. E. Peralta, F. Ogliaro, M. J. Bearpark, J. J. Heyd, E. N. Brothers, K. N. Kudin, V. N. Staroverov, T. A. Keith, R. Kobayashi, J. Normand, K. Raghavachari, A. P. Rendell, J. C. Burant, S. S. Iyengar, J. Tomasi, M. Cossi, J. M. Millam, M. Klene, C. Adamo, R. Cammi, J. W. Ochterski, R. L. Martin, K. Morokuma, O.

Farkas, J. B. Foresman, D. J. Fox, Gaussian 16 Revision C.01, Gaussian Inc., Wallingford CT, **2016**.

[32] M. L. Laury, M. J. Carlson, A. K. Wilson, *J. Comput. Chem.* **2012**, *33*, 2380–2387.

[33] F. Neese, *WIREs Comput. Mol. Sci.* **2012**, *2*, 73–78.

[34] T. A. Cool, J. Wang, K. Nakajima, C. A. Taatjes, A. Mcllroy, *Int. J. Mass Spectrom.* **2005**, *247*, 18–27.

[35] B. Yang, J. Wang, T. A. Cool, N. Hansen, S. Skeen, D. L. Osborn, *Int. J. Mass Spectrom.* **2012**, *309*, 118–128.

[36] A. D. Baker, C. Baker, C. R. Brundle, D. W. Turner, *Intern. J. Mass. Spectrom. Ion Phys.* **1968**, *1*, 285–301.

[37] O. P. Haefliger, R. Zenobi, *Anal. Chem.* **1998**, *70*, 2660–2665.

[38] J. E. Rink, U. Boesl, *Eur. J. Mass Spectrom.* **2003**, *9*, 23–32.

[39] A. M. Rijs, M. Kabeláč, A. Abo-Riziq, P. Hobza, M. S. de Vries, *ChemPhysChem* **2011**, *12*, 1816–1821.

[40] A. M. Rijs, N. Sändig, M. N. Blom, J. Oomens, J. S. Hannam, D. A. Leigh, F. Zerbetto, W. J. Buma, *Angew. Chem. Int. Ed.* **2010**, *49*, 3896–3900.

[41] A. M. Rijs, G. Ohanessian, J. Oomens, G. Meijer, G. von Helden, I. Compagnon, *Angew. Chem. Int. Ed.* **2010**, *49*, 2332–2335.

[42] M. Schmitt, F. Spiering, V. Zhaunerchyk, R. T. Jongma, S. Jaeqx, A. M. Rijs, W. J. v. d. Zande, *Phys. Chem. Chem. Phys.* **2016**, *18*, 32116–32124.

[43] B. Shukla, M. Koshi, *Phys. Chem. Chem. Phys.* **2010**, *12*, 2427–2437.

[44] D. A. Hrovat, J. Chen, K. N. Houk, W. T. Borden, *J. Am. Chem. Soc.* **2000**, *122*, 7456–7460.

[45] S. Sakai, *J. Mol. Struct. (Theochem)* **2002**, *583*, 181–188.

[46] R. Stockbauer, K. E. McCulloh, A. C. Parr, *Int. J. Mass Spectrom. Ion Phys.* **1979**, *31*, 187–189.

[47] F. Zhang, R. I. Kaiser, V. V. Kislov, A. M. Mebel, A. Golan, M. Ahmed, *J. Phys. Chem. Lett.* **2011**, *2*, 1731–1735.

[48] A. M. Burkhardt, K. L. K. Lee, P. B. Changala, C. N. Shingledecker, I. R. Cooke, R. A. Loomis, H. Wei, S. B. Charnley, E. Herbst, M. C. McCarthy, B. A. McGuire, *Ap. J. Lett.* **2021**, *913*, L18.

[49] B. Shukla, A. Susa, A. Miyoshi, M. Koshi, *J. Phys. Chem. A* **2008**, *112*, 2362–2369.

[50] P. Constantinidis, F. Hirsch, I. Fischer, A. Dey, A. M. Rijs, *J. Phys. Chem. A* **2017**, *121*, 181–191.

[51] R. S. Tranter, S. J. Klippenstein, L. B. Harding, B. R. Giri, X. Yang, J. H. Kiefer, *J. Phys. Chem. A* **2010**, *114*, 8240–8261.

[52] A. Comandini, K. Brezinsky, *J. Phys. Chem. A* **2011**, *115*, 5547–5559.

[53] L. Zhao, M. B. Prendergast, R. I. Kaiser, B. Xu, U. Ablikim, M. Ahmed, B.-J. Sun, Y.-L. Chen, A. H. H. Chang, R. K. Mohamed, F. R. Fischer, *Angew. Chem. Int. Ed.* **2019**, *58*, 17442–17450.

[54] A. C. Brown, J. Gibson, *J. Chem. Soc. Trans.* **1892**, *61*, 367–369.

[55] P. Constantinidis, H.-C. Schmitt, I. Fischer, B. Yan, A. M. Rijs, *Phys. Chem. Chem. Phys.* **2015**, *17*, 29064–29071.

[56] W. Yuan, Y. Li, P. Dagaut, J. Yang, F. Qi, *Combust. Flame* **2015**, *162*, 3–21.

[57] G. Blanquart, P. Pepiot-Desjardins, H. Pitsch, *Combust. Flame* **2009**, *156*, 588–607.

[58] T. Yang, R. I. Kaiser, T. P. Troy, B. Xu, O. Kostko, M. Ahmed, A. M. Mebel, M. V. Zagidullin, V. N. Azyazov, *Angew. Chem. Int. Ed.* **2017**, *56*, 4515–4519.

[59] L. Zhao, R. I. Kaiser, B. Xu, U. Ablikim, M. Ahmed, D. Joshi, G. Veber, F. R. Fischer, A. M. Mebel, *Nat. Astron.* **2018**, *2*, 413–419.

[60] J. Aguilera-Iparraguirre, W. Klopper, *J. Chem. Theory Comput.* **2007**, *3*, 139–145.

[61] Z. Li, P. Liu, P. Zhang, H. He, S. H. Chung, W. L. Roberts, *J. Phys. Chem. A* **2019**, *123*, 10323–10332.

[62] L. B. Tuli, A. M. Mebel, *Int. J. Chem. Kinet.* **2020**, *52*, 875–883.

[63] J. A. Miller, S. J. Klippenstein, *J. Phys. Chem. A* **2003**, *107*, 7783–7799.

[64] M. Lang, PhD thesis, University of Wuerzburg, Wuerzburg, **2015**.

[65] R. S. Tranter, A. W. Jasper, J. B. Randazzo, J. P. A. Lockhart, J. P. Porterfield, *Proc. Combust. Inst.* **2017**, *36*, 211–218.

[66] M.-L. Hebestreit, C. Henrichs, J. Schäfer, J. Martini, J. Auerswald, I. Fischer, A. Krueger, M. Schmitt, *J. Mol. Struct.* **2022**, *1250*, 131910.

CHAPTER 5

STACKING IS FAVORED OVER HYDROGEN BONDING IN AZAPHENANTHRENE DIMERS

This chapter is reproduced and partly adapted from

X. Miao, T. Preitschopf, F. Sturm, I. Fischer, A. K. Lemmens, M. Limbacher, R. Mitric, *J. Phys. Chem. Lett.* **2022**, *13*, 8939–8944.

5.1 Abstract

N-Doped polycyclic aromatic hydrocarbons have recently emerged as potential organic electronic materials. The function of such materials is determined not only by the intrinsic electronic properties of individual molecules but also by their supramolecular interactions in the solid state. Therefore, a proper characterization of the interactions between the individual units is of interest to materials science since they ultimately govern properties such as excitons and charge transfer. Here, we report a joint experimental and computational study of two azaphenanthrene dimers to determine the structure and the nature of supramolecular interactions in the aggregates. IR/UV double-resonance experiments were carried out using FIR and MIR free-electron laser radiation. The experimental spectra are compared with quantum chemical calculations for the lowest-energy π-stacked and hydrogen-bonded structures. The data reveal a preference of the π-stacked structure for the benzo[f]quinoline and the phenanthridine dimer.

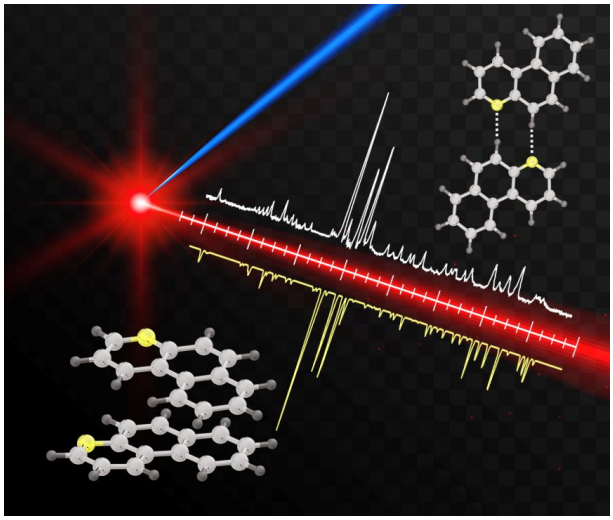

Figure 5.1. ToC graphic of published work on the structure of azaphenanthrene dimers. Reprinted with permission from Ref. [1]. Copyright 2022 American Chemical Society.

5.2 Introduction

Both inter- and intramolecular IR modes in PAH aggregates have been extensively studied and compared to those of monomers by both experimentalists and theoreticians.[2–5] Their aza-analogs, nitrogen-containing polycyclic aromatic hy-

drocarbons (PANH), have recently attracted considerable attention because the substitution of carbon by nitrogen allows to modify the optoelectronic properties of PAHs.[6,7] While acenes are known to be excellent hole conductors, the introduction of nitrogen atoms could lead to novel electron-conducting materials.[8] However, in order to design the functionality of such materials, it is necessary to understand the basic intra- and intermolecular photophysical processes as well as the supramolecular interactions determining the structure and packing in the solid state. In aggregate structures, the electronic properties of PANHs will be determined by the intermolecular interactions, which can lead to the emergence of light-induced phenomena such as singlet fission[9,10] and excimer formation.[11,12] Recently, quantum chemical calculations have been performed to address the tuning of the UV spectrum in pyrene by N-doping.[13] Furthermore, recent studies on the dinitrogen-doped *N*,*N*-dihydroanthracenes and phenanthrenes have addressed the possibility of singlet fission in these systems.[14] Indeed, several fully aromatic PANH were identified as promising candidates in these studies.[13,14] Recently, PANH also received increasing attention in astrochemistry due to their abundance in the interstellar medium and the atmosphere of Titan.[15,16] Protonated PANH are, for example, considered to be carriers for the unidentified infrared bands (UIB).[17] Here, we address the structure of the dimers of two azaphenanthrenes, benzo[f]quinoline and phenanthridine, to understand the intermolecular interactions in this type of system.

To elucidate intermolecular interactions, gas-phase experiments offer several advantages. They permit to study the intrinsic properties of the system without interference from the environment, give information on interactions between individual molecules, and allow a direct comparison with theoretical simulations and thus provide benchmarks for larger systems, as shown for several aromatic systems such as benzene,[18] pyrene,[19] and tetracene.[20] While pure hydrocarbons form only stacked structures, the possible structural diversity of PANH is much higher and H-bonded structures are possible besides stacked ones. The interplay among these different structural types has not yet been addressed experimentally for PANH dimers. Here, we use IR/UV ion dip spectroscopy[21] in combination with high-level quantum chemical calculations to characterize the geometry of dimers of benzo[f]quinoline and phenanthridine. IR/UV spectroscopy has been previously successfully applied to characterize biomolecules,[21–23] rotaxanes,[24] and reactive intermediates.[25–29] More recently, stacked acenaphthene and naphthalene dimers and their solvated clusters were studied,[30–32] but the IR/UV approach has not yet been employed to study the competition between stacked and hydrogen-bonded structures in molecular clusters.

5.3 Experimental

In the experiments, the dimers are ionized in a [1 + 1] and [1 + 1'] multiphoton process via an intermediate vibronic transition in the UV. The ground-state IR spectra of the dimers are then obtained by monitoring the depletion of the ion signal upon IR absorption of a selected m/z peak, resulting in a conformer-selected IR spectrum. The lack of characteristic functional groups requires experiments in the FIR and MIR fingerprint regions. Since an intense IR source is required to excite dilute samples, the experiments employed radiation from a free-electron laser (FEL).[33] Computations were carried out by density functional theory (DFT) employing a double hybrid functional with a long-range correction (ωB2GP-PLYP) as implemented within the ORCA 5.0.2 software package,[34] combined with the def2-TZVP basis set[35] and D4 dispersion correction.[36,37] The choice of double-hybrid functionals is substantiated by their higher accuracy compared to that of hybrid functionals when treating noncovalent interactions.[38] Although ωB2GP-PLYP performs a bit worse in the ground state than its global counterpart,[37] it treats π-stacked structures particularly well in excited states,[39] which will be the subject of our future studies on these systems. Initial H-bridged structures were constructed with Etter's rules,[40] while the initial structures of π-stacks were generated by running longtime molecular dynamics simulations (MD) using the ANI-1ccx neural network potential[41] as implemented in the TorchANI package[42] starting from optimized parallel displaced π-stacks at the DFT level. The obtained structures were then refined using DFT. The IR spectra were simulated by performing standard harmonic frequency analysis at the ωB2GP-PLYP-D4/def2-TZVP level of theory. The resulting stick spectra were scaled by a factor of 0.96[43] and broadened using a Gaussian-shaped function with $\sigma = 2$ cm^{-1} for visualization purposes. Additional experimental and computational details are given in Appendix C.

5.4 Results

In Scheme 5.1, the four lowest-energy isomers for the molecular dimers of both compounds are depicted. Two stacked dimers (labeled **pi** and **pi2**) are almost degenerate and constitute the lowest-energy structure. In the structures termed **pi**, the two molecules are slightly rotated with respect to each other, while in the structure named **pi2**, one of the units is flipped by 180°. Two hydrogen-bonded isomers (labeled **h6** and **h8**) are slightly higher in energy. While in **h6** the C-H bond of the same ring is involved in the H-bond, in **h8** it is the C-H bond of the

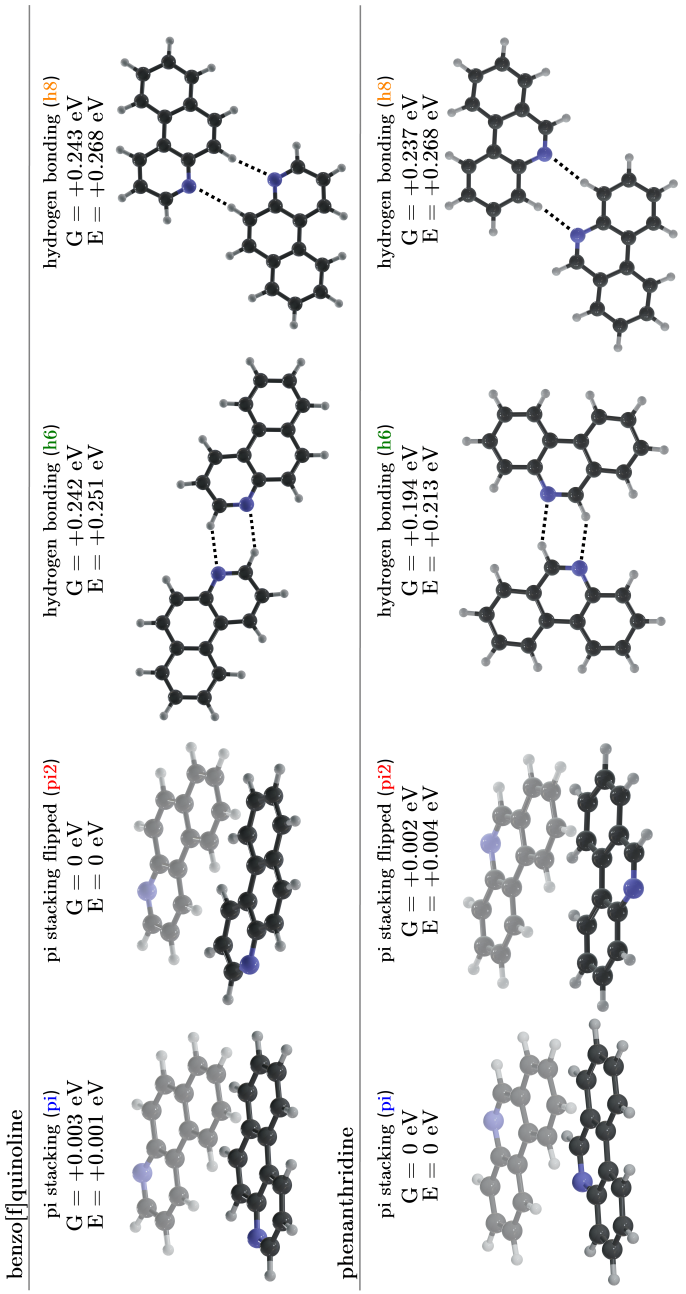

Scheme 5.1. Four lowest-energy dimer structures for benzo[f]quinoline (upper trace) and phenanthridine (lower race) and their relative electronic energy E and Gibbs energy G at 10 K, computed at the ωB2GP-PLYP-D4/def2TZVP level of theory. The vibrational contribution to the Gibbs energy has been included at the harmonic level. Intermolecular hydrogen-bonding interactions are indicated as dotted lines. Adapted with permission from Ref. [1]. Copyright 2022 American Chemical Society.

adjacent ring. In both molecules, the stacked structures are lower in energy than the hydrogen-bonded ones. However, within the accuracy of the calculations, the two stacked structures **pi** and **pi2** are equal in energy for both molecules. The same is true for the two hydrogen-bonded structures **h6** and **h8** of benzo[f]quinoline, whereas for phenanthridine **h6** is lower in energy than **h8**. While the π-π distances $d_{\pi\pi}$ and the twist angles $\Phi_{\pi\pi}$ between the monomer units are given for the stacked isomers, the hydrogen bond lengths d_{NH} are shown for the hydrogen-bridged isomers in Table 5.1. For **pi2**, a twist angle of zero is defined at the superimposition of phenanthrene. The complete sets of the Cartesian coordinates of all of the dimers is presented in the Supporting Information of Ref. [1].

Experimental and computed IR spectra for the benzo[f]quinoline dimer are compared in Figure 5.2. The dimer was excited at 342.33 nm, corresponding to the origin transition, and at 280.7 nm to check for the possible presence of another structure. The REMPI spectrum given in Appendix C (Figure S21) shows that the dimer transition at 342.33 nm is red-shifted with respect to the $S_1 \leftarrow S_0$ transition of the monomer, thus excitation of the monomer is avoided. To facilitate comparison, in all spectra (including simulations) of Figure 5.2 the most intense band at 746 cm^{-1} is deliberately plotted with equal intensity, and band intensities within each spectrum are scaled relative to this band. In trace a, the experimental IR/UV spectra, recorded at both excitation wavelengths, are given. As can be seen, the two spectra are almost indistinguishable, which indicates that the same dimer structure is excited at both wavelengths. Note that all bands are assigned to *intra*molecular monomer vibrations because the *inter*molecular modes are computed to appear below 200 cm^{-1}. Nevertheless, the shift of the vibrational bands of the dimer relative to the monomer is small but detectable, as can be seen in Figure S22 in Appendix C. In trace b of Figure 5.2, the calculated IR spectra of

Table 5.1. Geometric parameters of isomers shown in Scheme 5.1. Adapted with permission from Ref. [1]. Copyright 2022 American Chemical Society.

		$d_{\pi\pi}$ /Å	$\Phi_{\pi\pi}$ /deg	d_{NH} /Å
benzo[f]quinoline	**pi**	3.26	61.0	–
	pi2	3.34	8.30	–
	h6	–	–	2.40
	h8	–	–	2.43
phenanthridine	**pi**	3.34	45.1	–
	pi2	3.37	44.3	–
	h6	–	–	2.38
	h8	–	–	2.44

the four conformers depicted in the upper trace of Scheme 5.1 are presented for comparison. At first glance, all spectra are rather similar. However, closer inspection reveals a number of distinct differences. The three bands that appear between 800 and 880 cm^{-1} and are assigned to the C-H wagging modes constitute a first example. The wavenumbers of the bands are well represented by the **pi** and **pi2**

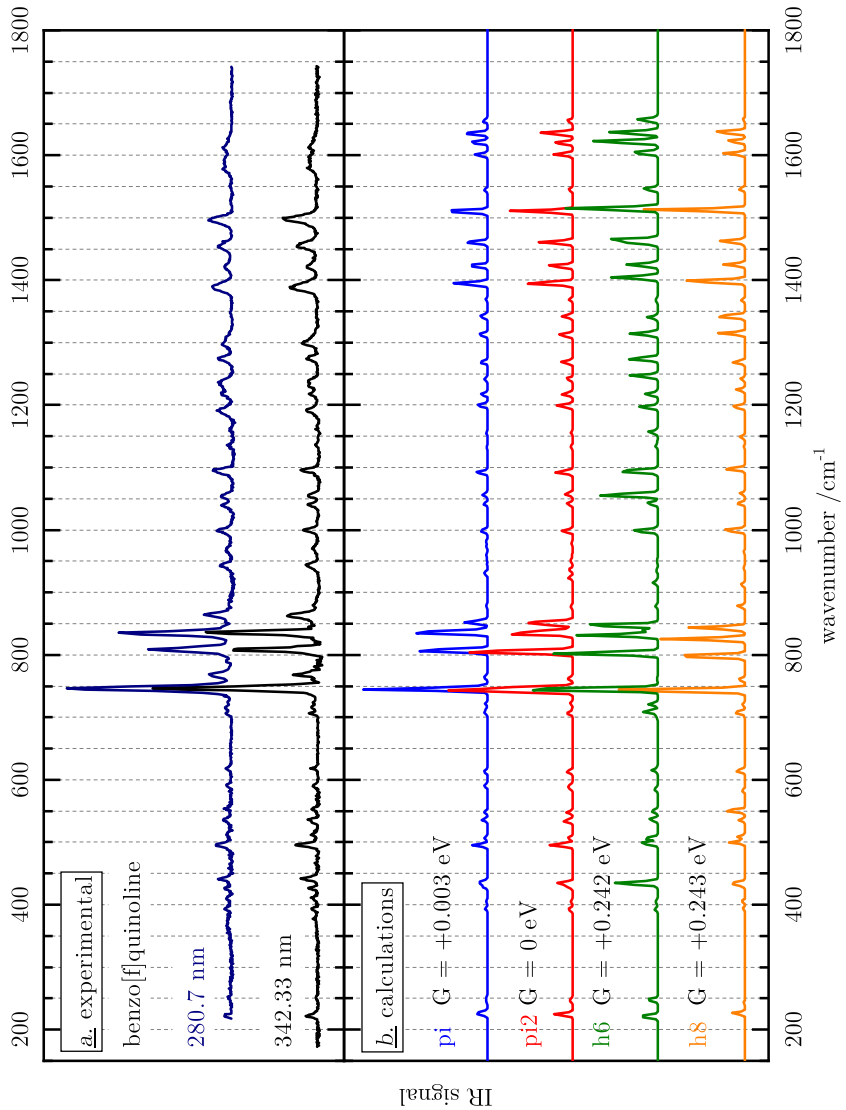

Figure 5.2. Trace a: IR/UV spectra of the benzo[f]quinoline dimer, recorded at two different excitation wavelengths. Trace b: Experimental data are compared to computed IR spectra of the four lowest energy dimer structures. Adapted with permission from Ref. [1]. Copyright 2022 American Chemical Society.

structures, while **h6** and **h8** deviate slightly more from the experiment. Interestingly, the intensity ratio is better represented by **pi** in comparison with **pi2**. In particular, the relative intensity of the band at 863 cm^{-1} is best simulated by the **pi** isomer.

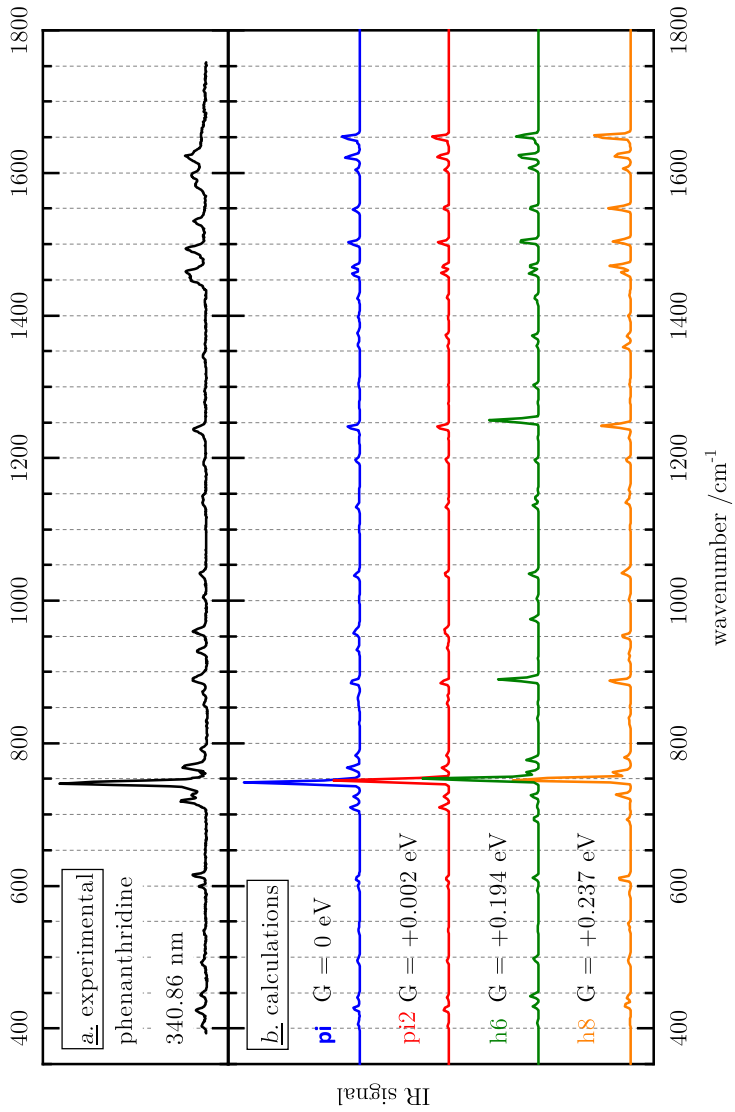

Figure 5.3. Trace a: IR/UV spectrum of the phenanthridine dimer, recorded at the $S_1 \leftarrow S_0$ origin transition. Trace b: Experimental data are compared to computed IR spectra of the four lowest energy dimer structures. Adapted with permission from Ref. [1]. Copyright 2022 American Chemical Society.

Further differences are apparent between 1360 and 1660 cm^{-1}. Here, calculations for both H-bonded structures yield intensities that are much higher than those observed in the experiment. The intensities computed for **pi** and **pi2** match the experiment much better. A similar situation is evident between 1000 and 1350 cm^{-1}. Here, the relative band intensities of **h6** do not match the experimental spectrum. Likewise, the relative intensity ratio of the bands between 490 and 560 cm^{-1} computed for **h8** is not observed in the experimental spectrum. Thus, after careful inspections, both H-bonded isomers can be ruled out. In contrast, for the two π-stacked structures rather similar spectra are predicted. Nevertheless, small differences are observed, where the relative band intensities between 800 and 880 and between 1360 and 1520 cm^{-1} are better represented by the theoretical spectrum of **pi**. However, due to the negligible energy difference, both π-stacked dimers are expected to be present in the molecular jet.

Figure 5.3 displays a comparison of the IR/UV spectrum of the phenanthridine dimer (trace a) with computed IR spectra of the four structures shown in the lower trace of Figure 5.3. The dimer was excited at a band red-shifted to the $S_1 \leftarrow S_0$ transition of the monomer[44] (see Figure S23 in Appendix C). Again, the region around the most dominant band at 744 cm^{-1} is in better agreement with the π-stacked structures. In particular, the small signal predicted at 759 cm^{-1} for **h6** and **h8** is not observed in the experimental spectrum. Similarly, the bands at 890 and 1240 cm^{-1}, which are due to in-plane ring and C-H deformation modes, appear in all computations. However, the H-bonded structures overestimate the intensity of both bands significantly. Smaller differences are observed in the low-wavenumber region between 400 and 450 cm^{-1}. Here the experimental spectrum is best represented by **pi** and **pi2**. Overall, the differences between the experiment and the computed spectra of the various dimer structures are smaller than in the case of benzo[f]quinoline, partly because the spectrum of the phenanthridine dimer is dominated by a single intense band.

5.5 Discussion

Due to the small differences among the computed spectra of the four isomers, we carried out a similarity analysis based on a statistical approach. For a quantitative comparison of the experimental spectra S^{exp} with the computed spectra S^{calc}, we employed the Pearson correlation coefficient r_p (eq. 5.1),[45–47] which has been widely used as a statistical measure for comparing IR and Raman spectra before:[48–51]

$$r_p = \frac{\sum_i (S_i^{calc} - \overline{S^{calc}}) \cdot (S_i^{exp} - \overline{S^{exp}})}{\sqrt{\sum_i (S_i^{calc} - \overline{S^{calc}})^2} \cdot \sqrt{\sum_i (S_i^{exp} - \overline{S^{exp}})^2}} \tag{5.1}$$

Here, S_i^x denotes the elements of the intensity vectors representing the spectra and $\overline{S^x}$ are the mean values of S_i^x, respectively. The computed spectra were broadened (σ = 2 cm^{-1}) and scaled with a factor slightly different from 0.96 to maximize r_p for all isomers. The optimized scaling factors and Pearson coefficients for both azaphenanthrene dimers are given in Table 5.2.

For benzo[f]quinoline, the spectrum measured using 342.33 nm for excitation was used as a reference. As can be seen, the **pi** stacks yield r_p values close to 0.8, significantly higher than those for the H-bonded structures, with values of 0.533 and 0.393, which confirms our assignment to a stacked conformation. The similar r_p values for **pi** and **pi2** also confirm that both isomers fit the experimental spectrum almost equally well.

For phenanthridine, the highest score was obtained for **pi2** with r_p = 0.865 (*cf.* Table 5.2). Interestingly, relatively high scores of between 0.6 and 0.7 were obtained for the hydrogen-bonded structures, while a slightly inferior r_p was obtained for **pi**. Thus, the correlation analysis confirms a stacked structure, but differences are less distinct than for benzo[f]quinoline. We point out that the single intense band in the spectrum dominates the similarity analysis and enters with a high weight into the determination of r_p, as observed before.[47] Also note that the correlation coefficients do not exceed 0.87, mainly due to the frequency mismatch in the higher-frequency region. This could be improved by including temperature-dependent anharmonic effects.

Table 5.2. Correlation (r_p) between experimental and computed spectra of the azaphenanthrene dimers and obtained scaling factors to maximize r_p. Adapted with permission from Ref. [1]. Copyright 2022 American Chemical Society.

	benzo[f]quinoline dimer	phenanthridine dimer
scaling factor	0.9624	0.9548
r_p(**pi**)	**0.783**	0.603
r_p(**pi2**)	0.763	**0.865**
r_p(**h6**)	0.533	0.691
r_p(**h8**)	0.393	0.773

5.6 Conclusions

To summarize, despite the small differences in the computed spectra, IR/UV spectroscopy is able to discriminate between π-stacked and H-bonded structures in PANH dimers. This requires a very good signal/noise ratio in the experiments and at the same time high-quality quantum chemical calculations that predict not only band positions properly but also band intensities. The IR/UV spectra of the dimers of benzo[f]quinoline and phenanthridine show that π-stacked dimers are preferentially formed in a jet rather than H-bonded structures. The experimental results confirm the computationally predicted lower energy of the π-stacked dimers and serve as a basis for further studies of the photophysical properties of these molecular aggregates.

References

[1] X. Miao, T. Preitschopf, F. Sturm, I. Fischer, A. K. Lemmens, M. Limbacher, R. Mitric, *J. Phys. Chem. Lett.* **2022**, 8939–8944.

[2] M. Rapacioli, F. Calvo, C. Joblin, P. Parneix, F. Spiegelman, *J. Phys. Chem. A* **2007**, *111*, 2999–3009.

[3] A. Ricca, C. W. Bauschlicher, L. J. Allamandola, *Astrophys. J.* **2013**, *776*, 31.

[4] J. E. Roser, A. Ricca, *Astrophys. J.* **2015**, *801*, 108.

[5] L. Dontot, F. Spiegelman, S. Zamith, M. Rapacioli, *Eur. Phys. J. D* **2020**, *74*, 216.

[6] U. H. F. Bunz, *Acc. Chem. Res.* **2015**, *48*, 1676–1686.

[7] U. H. F. Bunz, J. Freudenberg, *Acc. Chem. Res.* **2019**, *52*, 1575–1587.

[8] L. Ahrens, J. Butscher, V. Brosius, F. Rominger, J. Freudenberg, Y. Vaynzof, U. H. F. Bunz, *Chem. Eur. J.* **2020**, *26*, 412–418.

[9] J. Herz, T. Buckup, F. Paulus, J. Engelhart, U. H. F. Bunz, M. Motzkus, *J. Phys. Chem. Lett.* **2014**, *5*, 2425–2430.

[10] M. B. Smith, J. Michl, *Annu. Rev. Phys. Chem.* **2013**, *64*, 361–386.

[11] J. B. Birks, *Rep. Prog. Phys.* **1975**, *38*, 903–974.

[12] J. Vollbrecht, *New J. Chem.* **2018**, *42*, 11249–11254.

[13] X. Shao, A. J. A. Aquino, M. Otyepka, D. Nachtigallová, H. Lischka, *Phys. Chem. Chem. Phys.* **2020**, *22*, 22003–22015.

[14] E. Pradhan, S. Lee, C. H. Choi, T. Zeng, *J. Phys. Chem. A* **2020**, *124*, 8159–8172.

[15] J. Bouwman, A. Bodi, P. Hemberger, *Phys. Chem. Chem. Phys.* **2018**, *20*, 29910–29917.

[16] D. S. N. Parker, T. Yang, B. B. Dangi, R. I. Kaiser, P. P. Bera, T. J. Lee, *Astrophys. J.* **2015**, *815*, 115.

[17] H. A. Galué, O. Pirali, J. Oomens, *Astron. Astrophys.* **2010**, *517*, A15.

[18] M. Miyazaki, M. Fujii, *Phys. Chem. Chem. Phys.* **2015**, *17*, 25989–25997.

[19] J. Hoche, H.-C. Schmitt, A. Humeniuk, I. Fischer, R. Mitrić, M. I. S. Röhr, *Phys. Chem. Chem. Phys.* **2017**, *19*, 25002–25015.

[20] J. Hoche, M. Flock, X. Miao, L. N. Philipp, M. Wenzel, I. Fischer, R. Mitric, *Chem. Sci.* **2021**, *12*, 11965–11975.

[21] A. M. Rijs, J. Oomens, *Top. Curr. Chem.* **2014**, *364*, 1–42.

[22] S. Bakels, M.-P. Gaigeot, A. M. Rijs, *Chem. Rev.* **2020**, *120*, 3233–3260.

[23] S. Jaeqx, J. Oomens, A. Cimas, M.-P. Gaigeot, A. M. Rijs, *Angew. Chem. Int. Ed.* **2014**, *53*, 3663–3666.

[24] A. M. Rijs, I. Compagnon, J. Oomens, J. S. Hannam, D. A. Leigh, W. J. Buma, *J. Am. Chem. Soc.* **2009**, *131*, 2428–2429.

[25] R. G. Satink, G. Meijer, G. von Helden, *J. Am. Chem. Soc.* **2003**, *125*, 15714–15715.

[26] K. H. Fischer, J. Herterich, I. Fischer, S. Jaeqx, A. M. Rijs, *J. Phys. Chem. A* **2012**, *116*, 8515–8522.

[27] F. Hirsch, I. Fischer, S. Bakels, A. M. Rijs, *J. Phys. Chem. A* **2022**, *126*, 2532–2540.

[28] F. Hirsch, K. Pachner, I. Fischer, K. Issler, J. Petersen, R. Mitric, S. Bakels, A. M. Rijs, *ChemPhysChem* **2020**, *21*, 1515–1518.

[29] T. Preitschopf, F. Hirsch, A. K. Lemmens, A. M. Rijs, I. Fischer, *Phys. Chem. Chem. Phys.* **2022**, *24*, 7682–7690.

[30] A. K. Lemmens, S. Gruet, A. L. Steber, J. Antony, S. Grimme, M. Schnell, A. M. Rijs, *Phys. Chem. Chem. Phys.* **2019**, *21*, 3414–3422.

[31] A. K. Lemmens, P. Chopra, D. Garg, A. L. Steber, M. Schnell, W. J. Buma, A. M. Rijs, *Mol. Phys.* **2021**, *119*, e1811908.

[32] A. L. Steber, C. Pérez, B. Temelso, G. C. Shields, A. M. Rijs, B. H. Pate, Z. Kisiel, M. Schnell, *J. Phys. Chem. Lett.* **2017**, *8*, 5744–5750.

[33] D. Oepts, A. F. G. van der Meer, P. W. van Amersfoort, *Infrared Phys. Technol.* **1995**, *36*, 297–308.

[34] F. Neese, *WIREs Comput. Mol. Sci.* **2012**, *2*, 73–78.

[35] F. Weigend, R. Ahlrichs, *Phys. Chem. Chem. Phys.* **2005**, *7*, 3297–3305.

[36] E. Caldeweyher, C. Bannwarth, S. Grimme, *J. Chem. Phys.* **2017**, *147*, 034112.

[37] A. Najibi, M. Casanova-Páez, L. Goerigk, *J. Phys. Chem. A* **2021**, *125*, 4026–4035.

[38] L. Goerigk, S. Grimme, *Phys. Chem. Chem. Phys.* **2011**, *13*, 6670–6688.

[39] A. C. Hancock, L. Goerigk, *Rsc. Adv.* **2022**, *12*, 13014–13034.

[40] M. C. Etter, *Acc. Chem. Res.* **1990**, *23*, 120–126.

[41] J. S. Smith, O. Isayev, A. E. Roitberg, *Chem. Sci.* **2017**, *8*, 3192–3203.

[42] X. Gao, F. Ramezanghorbani, O. Isayev, J. S. Smith, A. E. Roitberg, *J. Chem. Inf. Model.* **2020**, *60*, 3408–3415.

[43] M. A. Palafox, *J. Phys. Chem. A* **1999**, *103*, 11366–11377.

[44] J. Prochorow, I. Deperasińska, Y. Stepanenko, *Chem. Phys. Lett.* **2004**, *399*, 239–246.

[45] K. Pearson, F. Galton, *Proc. R. Soc. London* **1895**, *58*, 240–242.

[46] H. Henschel, D. van der Spoel, *J. Phys. Chem. Lett.* **2020**, *11*, 5471–5475.

[47] H. Henschel, A. T. Andersson, W. Jespers, M. Mehdi Ghahremanpour, D. van der Spoel, *J. Chem. Theory Comput.* **2020**, *16*, 3307–3315.

[48] K. Baumann, J. T. Clerc, *Anal. Chim. Acta* **1997**, *348*, 327–343.

[49] C. Vrančić, W. Petrich, *J. Phys. Chem. A* **2011**, *115*, 12373–12379.

[50] X. Tan, X. Chen, S. Song, *J. Raman Spectrosc.* **2017**, *48*, 113–118.

[51] F. Zapata, C. García-Ruiz, *Spectrochim. Acta Part A* **2018**, *189*, 535–542.

CHAPTER 6

SUMMARY

6.1 Summary

Since polycyclic aromatic hydrocarbons (PAHs) have been proposed to play a significant role in the formation of carbon clusters and carbonaceous particles several decades ago, astronomy and combustion research communities have striven for a fundamental understanding of their underlying formation mechanisms and intermolecular interactions.[1] In space, these compounds have been shown to make up for 10−15 % of the total cosmic carbon and are considered as the carriers of the Unidentified Infrared Bands (UIB).[2] These IR emission features have been detected in a wide variety of astrophysical environments such as planetary nebulae and extragalactic sources, showing that PAHs are ubiquitously present in the wide universe.[3] In our immediate surroundings, PAHs are formed naturally (*e.g.,* in volcanoes) and by anthropogenic processes, mainly as a byproduct in the combustion of fossil fuels (*e.g.,* in motor vehicles). They are considered as detrimental environmental contaminants due to their toxic and carcinogenic potential as well as key building blocks for soot particles.[4]

Currently, astrochemical models propose major contributions to PAH formation from inner envelopes of carbon-rich asymptotic giant branch (AGB) stars, in which temperatures of a few 1000 K are commonly reached.[5] The so far suggested astrochemical mechanisms have been proposed on the basis of pathways that are observed in combustion processes.[6] Among them are the widely known hydrogen abstraction - acetylene addition (HACA) and phenyl addition - (dehydro-)cyclization (PAC) mechanisms.[7] Additionally, sequential reactions of resonance-stabilized radicals (RSR) are considered as key steps in the formation of PAHs, since they can accumulate in reacting environments due to their high stability.[8] However, the currently discussed formation pathways fail to account for the large abundances of PAHs observed in space, indicating the presence of additional mechanisms such as potential low-temperature pathways in the interstellar medium (ISM).[6]

To uncover alternative reaction pathways, advanced laboratory experiments in combination with (high-level) quantum-mechanical calculations are required. Since a large array of potentially entangled reactions might contribute to PAH formation, clean and well-defined experimental conditions are crucial to disentangle the complex reaction network.[9] In the research conducted in this thesis, we used high-temperature (pyrolysis) microreactors to generate the two resonantly stabilized radicals *2-methylallyl* (2-MA, C_4H_7) and *2-phenylallyl* (2-PA, C_9H_9) cleanly and at a high number density to conduct gas-phase experiments.[10] Substituted allyl radicals have been detected in the combustion of unsaturated fatty acid esters,

which are considered as potential biofuels.[11] In addition, C_4H_7 radicals might be formed in the ISM *via* the reaction of methylidyne (CH) with propene (C_3H_6),[12] which have both been detected in space.[13,14] On the other hand, no spectroscopic information on 2-PA have been reported so far. It is formally derived from 2-MA by replacing a methyl group (CH_3) by phenyl (C_6H_5), suggesting its potential relevance in astrochemical and combustion processes.

Furthermore, we investigated the structures of the azaphenanthrene dimers of *benzo[f]quinoline* and *phenanthridine*. N-doped PAHs, called nitrogenated polycyclic aromatic hydrocarbons (PANHs), are potentially important intermediates in the formation of biorelevant molecules such as nucleobases, the key building blocks for long-chain helical structures such as DNA and RNA.[15] Extraterrestrial nucleobases have been detected on stony meteorites,[16] making N-containing aromatic molecules potential tracers of the prebiotic chemical evolution of our Solar System.[17] The shape of the 11.2 μm UIB indicates PA(N)H clusters as potential carriers because it commonly exhibits an asymmetric tailing towards lower energies.[18] This spectral pattern might be due to red-shifted CH out-of-plane wagging modes, which is often observed in PA(N)H cluster configurations.[19] While pure PAHs only form stacked clusters, hydrogen-bonded geometries are also possible for PANHs, resulting in a wide variety of potentially formed structures.

To investigate the intrinsic spectral properties, the molecules of interest were studied at low temperatures under isolated conditions by using the molecular beam technique.[20] Coupled to a time-of-flight (TOF) mass spectrometer in combination with narrowband nanosecond pulsed laser systems, this allowed to record well-resolved spectra of isolated molecules in their electronic ground state. Mass-selectivity was obtained by resonance-enhanced multiphoton ionization (REMPI), which facilitates to selectively ionize a specific isomer *via* an intermediate excited electronic state.[21] Therefore, the molecules of interest require an UV chromophore in the range of 193−350 nm with, ideally, long excited state lifetimes in the nanosecond range.[22] This condition is commonly met by many PA(N)Hs with excited singlet state lifetimes between 10−1000 ns.[23] The combination of UV and IR spectroscopic methods facilitated an elegant way to distinguish between different isomers. Species-selective IR spectra were obtained by using action spectroscopy *via* an IR/UV ion dip scheme. In this approach, the change of the vibrational population in the electronic ground state after resonant IR absorption is probed by REMPI.[22] This technique relies on several parameters such as the IR photon energy, IR laser power, (an)harmonic character of the excited vibrational mode, and UV probe frequency, resulting in various processes that

might be involved in the depletion of the ion signal.[24] Yet, absorption of the first IR photon remains the bottleneck for this process, resulting in ground-state IR spectra. The assignment of the recorded IR/UV spectra was based on quantum chemical calculations, which were performed in the harmonic approximation.[25] As the error in this model has been identified as fairly systematic, multiplicative scaling factors for the calculated frequencies were used to account for anharmonic effects.[26] This approach accurately predicted vibrational spectra at reasonable computational costs.[25]

As the molecules of interest were investigated at very low concentrations in a molecular beam, high intense IR light sources were required. Table-top laser like an OPO/OPA system provide pulsed IR radiation at sufficient power between 2200 and 4500 cm^{-1}.[22,27] However, the spectral region around 3000 cm^{-1} of smaller PAHs is not molecule specific and dominated by Fermi resonances and anharmonic shifts.[28] Therefore, the experiments were performed in the fingerprint region between 500 and 1750 cm^{-1} using the free electron laser FELIX in Nijmegen, The Netherlands.[29] FELIX generates tunable and very intense IR radiation in the full FIR and MIR region (up to 200 mJ/pulse), making it an ideal light source to investigate the ground state properties of dilute samples in the gas-phase. While the experiments on the high-temperature chemistry of 2-MA and 2-PA were performed in collaboration with the group of *Prof. Dr. Anouk M. Rijs*, the measurements on the azaphenanthrene dimers were conducted with *Dr. Alexander K. Lemmens*.

In the first study presented in this thesis (Chapter 3), we recorded the gas-phase IR spectrum of 2-MA in the fingerprint region and identified several high-temperature reaction products, which were formed by secondary reactions in a pyrolysis microreactor. Among them were (aromatic) hydrocarbons such as fulvene, and benzene, as well as polycyclic molecules like (methylated) naphthalene. 2-MA was generated from 3-bromo-2-methylpropene at around 1000 K and resonantly ionized *via* the $(\nu_{28})^1(\nu_{25})^1$ combination band of the B $^2A_1$ (3s) state at 255.3 nm.[30] Small reaction products without sufficient UV absorption at this wavelength have been characterized by threshold photoelectron spectroscopy (TPES), *e.g.,* propargyl, allene, and 2-methyl-1-butene.[31] This complementary approach allowed to gain a deeper insight into the complex high-temperature reaction network of 2-MA. Three competing reactions have been identified that are involved in the formation of higher aromatics. First, the self-recombination reaction of 2-MA to 2,5-dimethyl-1,5-hexadiene facilitates direct access to aromatic hydrocarbons in a single bimolecular step as suggested by the presence of *p*-xylene. The latter is most likely generated *via* a very efficient conversion of 2,5-dimethyl-1,5-hexadiene

at high temperature, driven by aromatization with an entropically favourable loss of two H_2 molecules. Second, the unimolecular decomposition reaction of 2-MA to allene and a methyl radical, which serves as a viable source for the third reaction: the recombination of 2-MA with CH_3. Additionally, increasing amounts of methyl in the microreactor potentially accelerate molecular growth *via* methylation reactions, as suggested by the detection of methylated styrene isomers, *p*-ethyltoluene, and 2-methylnaphthalene. The identification of (methylated) naphthalene substantiates the importance of 2-MA as a considerable contributor to PAH formation in high-temperature environments.[32]

In the second study (Chapter 4), we extended the work conducted in Chapter 3, and investigated the high-temperature chemistry of 2-PA, which is formally derived from 2-MA by substituting a methyl group by phenyl. Its formation *via* the pyrolysis of 3-phenylbut-3-en-1-yl nitrite along with the generation of several reaction products was confirmed based on their gas-phase IR spectra with the aid of *ab initio* DFT calculations. Again three competing reactions were identified that are involved in molecular growth of 2-PA, two of which are highly similar to the ones already observed for 2-MA. The radical self-reaction leads to the formation of 2,5-diphenyl-1,5-hexadiene, which efficiently undergoes a Cope rearrangement followed by aromatization to form *p*-terphenyl. While the recombination product is apparent from the mass signal at m/z 234 in the SPI TOF-MS, it has not been observed in the work on 2-MA, but has been identified in the literature.[33] Furthermore, unimolecular decomposition of 2-PA at high temperature results in the generation of phenyl and allene. This reaction has already been predicted theoretically on reactions of chemically activated C_9H_9 isomers,[34] and is evident in the work conducted in this thesis as several identified reaction products exhibit phenyl groups (*e.g.,* biphenyl, 2-phenylnaphthalene, and *p*-terphenyl). The large amounts of phenyl present in the reactor facilitate an efficient formation of higher aromatic hydrocarbons *via* the aforementioned PAC mechanism. A prime example for mass growth by PAC is the detection of biphenyl, terphenyl, and triphenylene. Unimolecular decomposition of 2-MA parallels this highly efficient growth mechanism *via* mass growth due to methylation reactions. Finally, isomerization of 2-PA followed by loss of a hydrogen atom directly leads to the formation of the prototype PAH indene. The detection of the latter is of considerable interest as it has been recently identified in space.[35,36]

In the last study of this thesis (Chapter 5), we investigated the intermolecular interactions between the monomer units in dimers of benzo[f]quinoline and phenan-

thridine in a joint experimental and theoretical collaboration with the group of *Prof. Dr. Roland Mitric*. So far, the structures of PANHs dimers have not been investigated experimentally. Four lowest energy structures each were identified theoretically for the two molecular dimers, whereby the two stacked configurations are almost degenerate and constitute the lowest-energy structures for each molecule. Slightly higher in energy are two hydrogen-bonded isomers, which again were computed to be almost degenerate for benzo[f]quinoline and slightly different in energy for phenanthridine. The corresponding computed IR spectra were compared to the experimental IR/UV spectra of the azaphenanthrene dimers. For benzo[f]quinoline, the dimer was excited at 342.33 nm, which is red-shifted with respect to the $S_1 \longleftarrow S_0$ transition of the monomer to avoid excitation of the latter. Additionally, it was excited at 280.7 nm to potentially probe another configuration. The two recorded IR/UV spectra are almost identical, showing that the same structure was excited at both wavelengths. The phenanthridine dimer was excited at 340.86 nm, which again is red-shifted to the $S_1 \longleftarrow S_0$ transition of the monomer. For both dimers, differences in the computed IR spectra of the four lowest energy structures are small and mainly visible in differences in the computed relative intensities of the vibrational modes. However, a detailed comparison with the experimental IR/UV spectra allowed to identify various characteristic features, in particular in the spectral region of the C−H out-of-plane wagging modes. Here, the experimental spectra are best represented by the computed spectra of the π-stacked structures for both azaphenanthrene dimers. Furthermore, we employed the Pearson correlation coefficient to substantiate the previous assignments. This method has been commonly used as a statistical measure for comparing IR and Raman spectra before,[37,38] confirming that π-stacked dimer structures of benzo[f]quinoline and phenanthridine are preferentially formed in a jet expansion.[39]

6.2 Zusammenfassung

Seitdem angenommen wird, dass polyzyklische aromatische Kohlenwasserstoffe (PAHs) eine wesentliche Rolle in der Bildung von Kohlenstoffclustern und kohlenstoffhaltigen Partikeln spielen, streben Astronomie und Verbrennungsforschung ein grundlegendes Verständnis ihrer Bildungsmechanismen und intermolekularen Wechselwirkungen an.[1] In der Astronomie sind PAHs von großem Interesse, da einerseits ca. 10−15 % des Kohlenstoffs im Weltall in diesen komplexen Verbindungen gebunden ist und sie andererseits als Träger der sogenannten *Unidentified Infrared Bands* (UIBs) vermutet werden. Dabei handelt es sich um Emissionsbanden im infraroten Wellenlängenbereich, welche in einer Vielzahl astrophysikalischer Umgebungen wie planetarischen Nebeln oder extragalaktischen Objekten detektiert wurden.[3] In unserer unmittelbaren Umgebung werden PAHs auf natürliche Weise (etwa in Vulkanen) gebildet oder sind wichtige Nebenprodukte anthropogener Prozesse, wobei sie insbesondere bei der Verbrennung fossiler Brennstoffe (beispielsweise in Motoren) entstehen. Hier sind PAHs von besonderem Interesse, da sie aufgrund ihres toxischen und kanzerogenen Potentials als Umweltschadstoffe gelten. Zudem bilden sie die Grundbausteine in der Bildung von Rußpartikeln.[4]

Derzeit gehen astronomische Modelle davon aus, dass PAHs überwiegend in den inneren Strukturen von kohlenstoffreichen AGB-Sternen (*asymptotic giant branch*) gebildet werden.[5] In diesen Umgebungen herrschen Temperaturen von mehreren 1000 K, weshalb die aktuellen astrochemischen Bildungsmechanismen auf Reaktionswegen beruhen, die in Verbrennungsprozessen beobachtet wurden.[6] Bekannte Beispiele sind der HACA (*hydrogen abstraction - acetylene addition*) und der PAC (*phenyl addition - (dehydro)-cyclization*) Mechanismus.[7] Zudem gelten sequentielle Reaktionen von resonanzstabilisierten Radikalen (RSR) als entscheidende Schritte der Bildung von PAHs, da sich diese Radikale aufgrund ihrer Stabilität anreichern und somit mit hohen Konzentrationen in reaktiven Umgebungen auftreten können.[8] Allerdings sind die bisherigen Modelle nicht in der Lage, die große Menge an PAH Molekülen im All zu erklären. Daher wird davon ausgegangen, dass eine Vielzahl weiterer Bildungsmechanismen auftreten, die beispielsweise auch unter sehr niedrigen Temperaturen im interstellaren Raum (ISM) ablaufen.[6]

Um weitere Reaktionswege zu untersuchen, werden fortschrittliche Experimente in Verbindung mit quantenmechanischen Rechnungen auf hohem theoretischen Level benötigt. Die Wahl wohldefinierter experimenteller Bedingungen ist dabei von großer Bedeutung, da eine Vielzahl von möglicherweise miteinander verwobenen Reaktionen zur Bildung von PAHs beitragen kann.[9] In dieser Arbeit wurden Pyrolyse-Mikroreaktoren verwendet, um die zwei resonanzstabi-

lisierten Radikale *2-Methylallyl* (2-MA, C_4H_7) und *2-Phenylallyl* (2-PA, C_9H_9) mit hohem Reinheitsgrad und mit hoher Teilchendichte zu erzeugen.[10] Substituierte Allylradikale konnten in der Verbrennung von ungesättigten Fettsäureestern beobachtet werden, welche als potentielle Biokraftstoffe in Betracht gezogen werden.[11] Zudem könnten C_4H_7-Radikale durch die Reaktion von Methylidin (CH) mit Propen (C_3H_6), zwei Spezies, welche jeweils im All identifiziert wurden,[13,14] im ISM gebildet werden.[12] 2-PA wird formal durch Substitution einer Methylgruppe (CH_3) mit Phenyl (C_6H_5) aus 2-MA erhalten. Diese Verwandtschaft legt eine mögliche Relevanz von 2-PA in astrochemischen und verbrennungsrelevanten Prozessen nahe, obwohl es bisher noch keine spektroskopischen Informationen zu diesem Radikal in der Literatur gibt.

Im dritten Projekt dieser Arbeit wurden die Strukturen der Azaphenanthren-Dimere von *Benzo[f]quinolin* und *Phenanthridin* untersucht. N-dotierte PAHs, sogenannte PANHs, gelten als potentiell wichtige Intermediate der Bildung von biorelevanten Molekülen wie Nukleinbasen, die wesentliche Bausteine der DNA und RNA darstellen.[15] Extraterrestrische Nukleinbasen konnten bereits auf Meteoriten detektiert werden,[16] weshalb stickstoffhaltige aromatische Verbindungen Indikatoren für die chemische Entwicklung präbiotischen Lebens in unserem Sonnensystem darstellen könnten.[17] Die asymmetrische und rotverschobene Form der 11.2 μm UIB könnte auf PA(N)H-Cluster als mögliche Träger zurückzuführen sein.[18] Ursache für das spektrale Muster könnten rotverschobene CH Wippschwingungen (aus der Ebene) sein, da deren Verschiebung zu niedrigeren Energien häufig in PA(N)H-Clusterkonfigurationen beobachtet wurde.[19] Während reine PAHs lediglich gestapelte Clusterstrukturen bilden, sind im Falle von PANHs Wasserstoffbrücken-gebundene Konfigurationen ebenfalls denkbar, was eine große Anzahl an möglichen Clusterstrukturen zur Folge hat.

In dieser Arbeit wurden die Moleküle unter isolierten Bedingungen und bei niedrigen Temperaturen mit Hilfe der Molekularstrahltechnik untersucht.[20] In Kombination mit einem Flugzeit-Massenspektrometer (TOF) und schmalbandigen gepulsten Nanosekundenlasern ermöglichte dies die Aufnahme von hinreichend gut aufgelösten Spektren in der Gasphase. Massenselektivität wurde mittels der resonanzverstärkten Mehrphotonenionisation (REMPI) erzielt, die zusätzlich eine selektive Ionisation eines spezifischen Isomers über ausgewählte elektronische Zwischenzustände ermöglichte.[21] Ein effizienter REMPI-Prozess setzt zunächst ein UV-Chromophor im Bereich von 193−350 nm voraus, sowie, idealerweise, Lebenszeiten angeregter Zustände im Nanosekundenbereich.[22] Diese Bedingungen werden typischerweise von vielen PA(N)Hs erfüllt, welche angeregte Singulett-Zustän-

de mit Lebenszeiten zwischen 10−1000 ns aufweisen.[23] Die Verbindung von UV- und IR-spektroskopischen Techniken ermöglichte anschließend einen eleganten Weg, um zwischen unterschiedlichen Isomeren eindeutig zu unterscheiden. Dabei wurden mit Hilfe der *IR/UV Ion Dip Spektroskopie* isomerenselektive IR-Spektren aufgenommen. Diese Methode beruht auf einer Änderung der Schwingungspopulation im elektronischen Grundzustand nach resonanter IR-Absorption.[22] Da die Technik von mehreren Parametern wie der IR-Photonenenergie, IR-Laserleistung, (An-)Harmonizität der angeregten Schwingungsmode, oder der verwendeten UV-Wellenlänge abhängt, können verschiedene Prozesse zu einer Abnahme des Ionensignals führen.[24] Dennoch bildet die Absorption des ersten IR-Photons die Basis der IR/UV-Spektroskopie, sodass IR-Spektren des Grundzustands aufgenommen werden. Die Zuordnung der IR/UV-Spektren erfolgte anschließend mit Hilfe von quantenchemischen Rechnungen, die in harmonischer Näherung durchgeführt wurden.[25] Der Fehler dieser Methode ist als überwiegend systematisch identifiziert worden, weshalb multiplikative Faktoren für die Skalierung der berechneten Frequenzen verwendet wurden, um anharmonischen Effekten Rechnung zu tragen.[26] Dieser Ansatz führte zu akkurat berechneten Schwingungsspektren bei einem vertretbaren computerbasierten, rechnerischen Aufwand.[25]

Aufgrund der niedrigen Probenkonzentration in einem Molekularstrahl werden intensive IR Lichtquellen benötigt, um erfolgreich IR/UV-Spektren zu messen. Beispielsweise liefern Table-Top Laser wie OPA/OPA Systeme gepulste IR-Strahlung mit hinreichend hoher Leistung im Bereich von 2200−4500 cm^{-1}.[22,27] Allerdings ist der spektrale Bereich um 3000 cm^{-1} kleinerer PAHs nicht molekülspezifisch und wird zusätzlich von Fermi-Resonanzen und anharmonischen Verschiebungen dominiert.[28] Aus diesem Grund wurden die Experimente im Fingerprintbereich zwischen 500 und 1750 cm^{-1} am Freien-Elektronen-Laser FELIX in Nimwegen (NL) durchgeführt.[29] FELIX erzeugt durchstimmbare IR Strahlung hoher Intensität (bis zu 200 mJ/Puls) über das gesamte Spektrum des FIR und MIR Bereichs und stellt somit eine ideale Lichtquelle dar, um die Grundzustandseigenschaften verdünnter Proben in der Gasphase zu untersuchen. Während die Experimente der ersten zwei Strahlzeiten am FELIX Laboratorium noch in Zusammenarbeit mit der Gruppe von *Prof. Dr. Anouk M. Rijs* durchgeführt wurden, fand die dritte Strahlzeit in Kooperation mit *Dr. Alexander K. Lemmens* statt.

In der ersten Studie dieser Arbeit (Kapitel 3) wurden das IR Spektrum von 2-MA im Fingerprintbereich aufgenommen und mehrere Hochtemperatur-Reaktionsprodukte identifiziert, die durch sekundäre Reaktionen im Pyrolysereaktor gebildet wurden. Darunter befanden sich (aromatische) Kohlenwasserstoffe wie Fulven und

Benzol, sowie polyzyklische Moleküle wie (methyliertes) Naphthalin. 2-MA wurde dabei aus dem Vorläufer 3-Brom-2-methylpropen bei ca. 1000 K erzeugt und resonant über die $(\nu_{28})^1(\nu_{25})^1$ Kombinationsbande des B $^2A_1$ (3s) Zustands mit 255.3 nm ionisiert.[30] Kleine Pyrolyseprodukte ohne hinreichender UV Absorption wurden durch Schwellenphotoelektronenspektroskopie (TPES) charakterisiert. Ausgewählte Beispiele hiervon sind Propargyl, Allen und 2-Methyl-1-buten.[31] Diese ergänzende Methode ermöglichte einen vertiefteren Einblick in die komplexe Hochtemperatur-Chemie von 2-MA. Dabei konnten drei konkurrierende Reaktionen identifiziert werden, die maßgeblich an der Bildung aromatischer Verbindungen beteiligt sind. Zunächst ermöglicht die Rekombinationsreaktion von 2-MA zu 2,5-Dimethyl-1,5-hexadien die Bildung eines aromatischen Kohlenwasserstoffs, *p*-Xylol, in einem einzigen bimolekularen Schritt. Letzteres Molekül entsteht vermutlich durch eine sehr effiziente Umwandlung von 2,5-Dimethyl-1,5-hexadien bei hohen Temperaturen, welche durch die Bildung eines aromatischen Systems und dem entropisch günstigen Verlust zweier H_2-Moleküle begünstigt wird. Weiterhin dient die unimolekulare Zerfallsreaktion von 2-MA in Allen und Methyl als wichtige Quelle für die dritte Reaktion, die Rekombination von 2-MA mit CH_3. Die Zerfallsreaktion führt außerdem zu wachsenden Mengen an Methyl im Reaktor, was möglicherweise in einem schnelleren molekularen Wachstum durch Methylierungsreaktionen resultiert. Das effiziente Wachstum durch Methyladditionen konnte durch den Nachweis von methylierten Styrolisomeren, *p*-Ethyltoluol and 2-Methylnaphthalin belegt werden. Letztlich konnte durch die Detektion von (methyliertem) Naphthalin die mögliche Rolle von 2-MA in der Bildung von PAHs in Hochtemperatur-Umgebungen untermautert werden.[32]

In der zweiten Studie dieser Thesis (Kapitel 4) wurde die Arbeit aus Kapitel 3 erweitert und die Hochtemperatur-Chemie von 2-PA, das formal aus 2-MA durch Substitution einer Methylgruppe mit Phenyl entsteht, untersucht. Die Bildung von 2-PA durch Pyrolyse des Vorläufers 3-Phenylbut-3-en-1-yl-nitrit sowie die Erzeugung von mehreren Reaktionsprodukten wurde anhand der zugehörigen Gasphasen-IR-Spektren in Kombination mit *ab initio* DFT Rechnungen nachgewiesen. Erneut konnten drei konkurrierende Reaktionen identifiziert werden, die zu molekularem Wachstum führen, wobei zwei dieser Reaktionen sehr ähnlich zu den Hochtemperatur-Reaktionen von 2-MA ablaufen. Die Radikal-Rekombinationsreaktion führt zur Bildung von 2,5-Diphenyl-1,5-hexadien, das sehr effizient in einer Cope-Umlagerung und anschließender Aromatisierung *p*-Terphenyl bildet. Dabei konnte die Bildung des Rekombinationsprodukts durch das Massensignal bei m/z 234 im Einphotonen-Massenspektrum (SPI TOF-MS) beobachtet werden, während das Massensignal

m/z 110 in der Arbeit des 2-MA nicht detektiert wurde, aber in der Literatur bekannt ist.[33] Weiterhin führt der unimolekulare Zerfall von 2-PA bei hohen Temperaturen zur Bildung von Phenyl und Allen. Diese Reaktion ist bereits durch eine theoretische Arbeit an chemisch aktivierten C_9H_9-Isomeren bekannt,[34] und konnte in der Studie dieser Thesis anhand von mehreren Reaktionsprodukten bestätigt werden, die Phenylgruppen aufweisen (z.B. Biphenyl, 2-Phenylnaphthalin und *p*-Terphenyl). Hohe Konzentrationen an Phenyl im Reaktor ermöglichen eine effiziente Bildung höherer aromatischer Kohlenwasserstoffe durch den bereits erwähnten PAC-Mechanismus. Ein Musterbeispiel für diesen Reaktionsweg stellt die Detektion von Biphenyl, Terphenyl und Triphenylen dar. Im Fall von 2-MA ist dieser Mechanismus nebenläufig zu zahlreichen Methylierungsreaktionen. Zuletzt ermöglicht die Isomerisierung von 2-PA mit anschließendem H-Verlust direkt die Bildung des Prototyp-PAH Inden. Der Nachweis des Letzteren ist von besonderem Interesse, da es kürzlich im All identifiziert wurde.[35,36]

In der letzten Studie dieser Arbeit (Kapitel 5) wurden die intermolekularen Wechselwirkungen zwischen den Monomereinheiten der Dimere von Benzo[f]quinolin und Phenanthridin in einer Kollaboration mit der Gruppe von *Prof. Dr. Roland Mitric* untersucht. Bis zu diesem Zeitpunkt sind die Strukturen von PANH-Dimeren in der Literatur noch nicht experimentell untersucht worden. Zunächst konnten für beide Dimere die vier energetisch günstigste Strukturen theoretisch ermittelt werden, wobei jeweils die gestapelten Konfigurationen nahezu entartet sind und die energetisch niedrigsten Strukturen bilden. Etwas energetisch höher liegen die Wasserstoffbrücken-gebundenen Isomere, die für das Benzo[f]quinolin-Dimer erneut nahezu entartet sind und sich für das Phenanthridin-Dimer energetisch leicht unterscheiden. Die zugehörigen berechneten IR-Spektren wurden mit den experimentellen IR/UV-Spektren der Azaphenanthren Dimere verglichen. Im Fall von Benzo[f]quinolin wurde das Dimer mit einer Wellenlänge von 342.33 nm angeregt, die rotverschoben gegenüber dem $S_1 \longleftarrow S_0$-Übergang des Monomers ist. Zudem wurde das Dimer bei 280.7 nm untersucht, um möglicherweise eine weitere Struktur im Jet zu detektieren. Die zwei aufgenommenen IR/UV-Spektren sind allerdings nahezu identisch, sodass in beiden Fällen die gleiche Struktur angeregt wurde. Das Phenanthidin-Dimer wurde bei 340.86 nm untersucht, einer Wellenlänge, die erneut rotverschoben gegenüber dem $S_1 \longleftarrow S_0$-Übergangs des Monomers ist. Für beide Dimere zeigten sich lediglich geringe Unterschiede in den berechneten IR-Spektren der vier energetisch günstigsten Isomere, die sich überwiegend in Unterschieden der relativen Intensitäten der berechneten Schwingungsbanden zeigten. Allerdings ermöglichte ein vertiefter Vergleich mit den experimentellen IR/UV-

Spektren dennoch die Identifizierung verschiedener spektraler Charakteristiken, insbesondere im Bereich der C−H Wippschwingungen (aus der Ebene). Dort werden die experimentellen Spektren beider Dimere jeweils am besten von den berechneten Spektren der gestapelten Dimerstrukturen dargestellt. Um diese Zuordnung zu untermauern, wurde zusätzlich eine statistische Analyse unter Anwendung des Pearson Korrelationskoeffizienten durchgeführt. Diese Methode wurde schon häufig für die statistische Analyse von IR- und Ramanspektren verwendet[37,38] und konnte die vorherige Zuordnung der Bildung von gestapelten Dimerstrukturen für Benzo[f]quinolin und Phenanthridin im Jet bestätigen.[39]

References

[1] R. I. Kaiser, N. Hansen, *J. Phys. Chem. A* **2021**, *125*, 3826–3840.

[2] A. G. G. M. Tielens, *EAS Publ. Ser.* **2011**, *46*, 3–10.

[3] E. Peeters, *Proc. Int. Astron. Union* **2011**, *7*, 149–161.

[4] A. T. Lawal, *Cogent Environ. Sci.* **2017**, *3*, 1339841.

[5] N. Prantzos in *Encyclopedia of Astrobiology*, Springer, Berlin, Heidelberg, **2011**, pp. 117–118.

[6] R. I. Kaiser, D. S. Parker, A. M. Mebel, *Annu. Rev. Phys. Chem.* **2015**, *66*, 43–67.

[7] H. Wang, M. Frenklach, *Combust. Flame* **1997**, *110*, 173–221.

[8] D. S. N. Parker, R. I. Kaiser, *Chem. Soc. Rev.* **2017**, *46*, 452–463.

[9] H. Richter, J. B. Howard, *Prog. Energy Combust. Sci.* **2000**, *26*, 565–608.

[10] D. W. Kohn, H. Clauberg, P. Chen, *Rev. Sci. Instrum.* **1992**, *63*, 4003–4005.

[11] C. K. Westbrook, *Annu. Rev. Phys. Chem.* **2013**, *64*, 201–219.

[12] J. M. Ribeiro, A. M. Mebel, *J. Phys. Chem. A* **2016**, *120*, 1800–1812.

[13] W. S. Adams, *Astrophys. J.* **1941**, *93*, 11.

[14] N. Marcelino, J. Cernicharo, M. Agúndez, E. Roueff, M. Gerin, J. Martín-Pintado, R. Mauersberger, C. Thum, *Astrophys. J.* **2007**, *665*, L127.

[15] Z. Peeters, O. Botta, S. B. Charnley, R. Ruiterkamp, P. Ehrenfreund, *Astrophys. J.* **2003**, *593*, L129.

[16] M. P. Callahan, K. E. Smith, H. J. Cleaves, J. Ruzicka, J. C. Stern, D. P. Glavin, C. H. House, J. P. Dworkin, *Proc. Natl. Acad. Sci. U. S. A.* **2011**, *108*, 13995–13998.

[17] A. C. Andersen, H. Haack, *Int. J. Astrobiol.* **2005**, *4*, 13–17.

[18] J. E. Roser, A. Ricca, *Astrophys. J.* **2015**, *801*, 108.

[19] J. E. Roser, A. Ricca, *Proc. Int. Astron. Union* **2019**, *2019*, 1–3.

[20] R. E. Smalley, L. Wharton, D. H. Levy, *Acc. Chem. Res.* **1977**, *10*, 139–145.

[21] U. Boesl, *J. Phys. Chem.* **1991**, *95*, 2949–2962.

[22] A. M. Rijs, J. Oomens, *Top. Curr. Chem.* **2014**, *364*, 1–42.

[23] O. P. Haefliger, R. Zenobi, *Anal. Chem.* **1998**, *70*, 2660–2665.

[24] A. K. Lemmens, D. B. Rap, J. M. M. Thunnissen, S. Gruet, A. L. Steber, S. Panchagnula, A. G. G. M. Tielens, M. Schnell, W. J. Buma, A. M. Rijs, *J. Phys. Chem. Lett.* **2020**, *11*, 8997–9002.

[25] R. L. Jacobsen, R. D. I. Johnson, K. K. Irikura, R. N. Kacker, *J. Chem. Theory Comput.* **2013**, *9*, 951–954.

[26] M. W. D. Hanson-Heine, M. W. George, N. A. Besley, *J. Phys. Chem. A* **2012**, *116*, 4417–4425.

[27] M. Vainio, L. Halonen, *Phys. Chem. Chem. Phys.* **2016**, *18*, 4266–4294.

[28] E. Maltseva, A. Petrignani, A. Candian, C. J. Mackie, X. Huang, T. J. Lee, A. G. G. M. Tielens, J. Oomens, W. J. Buma, *Astrophys. J.* **2015**, *814*, 23.

[29] D. Oepts, A. F. G. van der Meer, P. W. van Amersfoort, *Infrared Phys. Technol.* **1995**, *36*, 297–308.

[30] M. Gasser, J. A. Frey, J. M. Hostettler, A. Bach, *J. Mol. Spectrosc.* **2010**, *263*, 93–100.

[31] M. Lang, PhD thesis, University of Wuerzburg, Wuerzburg, **2015**.

[32] T. Preitschopf, F. Hirsch, A. K. Lemmens, A. M. Rijs, I. Fischer, *Phys. Chem. Chem. Phys.* **2022**, *24*, 7682–7690.

[33] R. S. Tranter, A. W. Jasper, J. B. Randazzo, J. P. A. Lockhart, J. P. Porterfield, *Proc. Combust. Inst.* **2017**, *36*, 211–218.

[34] L. Vereecken, J. Peeters, *Phys. Chem. Chem. Phys.* **2003**, *5*, 2807–2817.

[35] A. M. Burkhardt, K. L. K. Lee, P. B. Changala, C. N. Shingledecker, I. R. Cooke, R. A. Loomis, H. Wei, S. B. Charnley, E. Herbst, M. C. McCarthy, B. A. McGuire, *Ap. J. Lett.* **2021**, *913*, L18.

[36] T. Preitschopf, F. Sturm, I. Stroganova, A. K. Lemmens, A. M. Rijs, I. Fischer, *Chem. Euro. J.* **2023**, *29*, e202202943.

[37] K. Baumann, J. T. Clerc, *Anal. Chim. Acta* **1997**, *348*, 327–343.

[38] X. Tan, X. Chen, S. Song, *J. Raman Spectrosc.* **2017**, *48*, 113–118.

[39] X. Miao, T. Preitschopf, F. Sturm, I. Fischer, A. K. Lemmens, M. Limbacher, R. Mitric, *J. Phys. Chem. Lett.* **2022**, 8939–8944.

APPENDIX

A Supplementary Information for Published Work on 2-Methylallyl Radicals

This section is adapted from

T. Preitschopf, F. Hirsch, A. K. Lemmens, A. M. Rijs, I. Fischer, *Phys. Chem. Chem. Phys.* **2022**, *24*, 7682–7690

with permission from the PCCP Owner Societies.

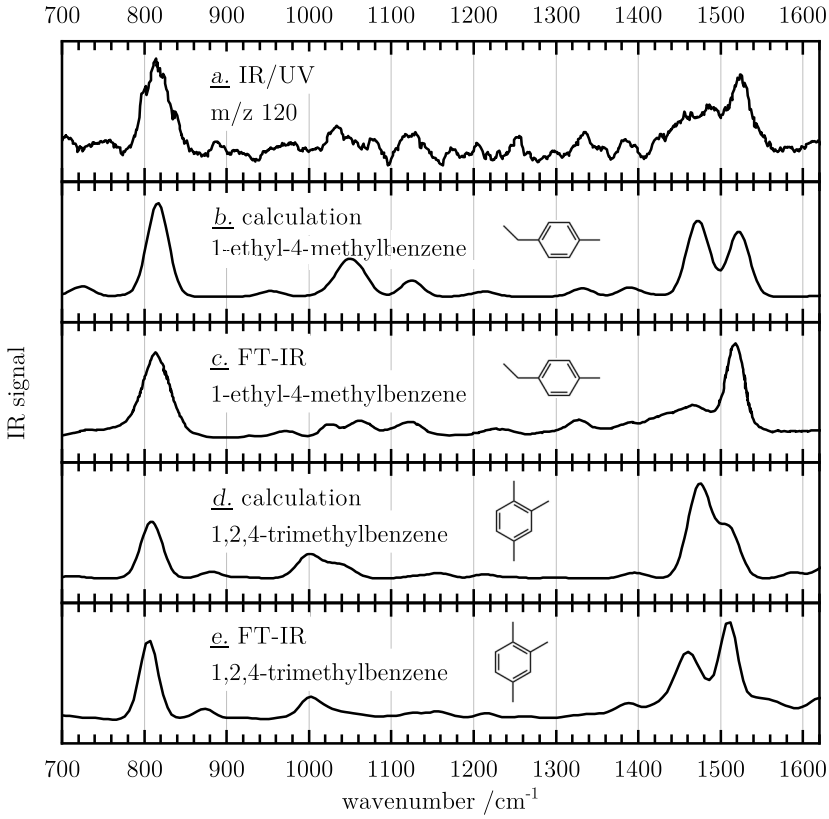

Figure S1. IR/UV spectrum of m/z 120 (trace a) in comparison with computed IR spectra of 1-ethyl-4-methylbenzene (b) and 1,2,4-trimethylbenzene (d). Both computations overestimate the intensities of the bands at around 1470 cm^{-1}. To substantiate the assignments, gas-phase FT-IR spectra were recorded, and excellent agreement is observed between the IR/UV data and the FT-IR spectrum of 1-ethyl-4-methylbenzene (c). Adapted from Ref. [1] with permission from the PCCP Owner Societies.

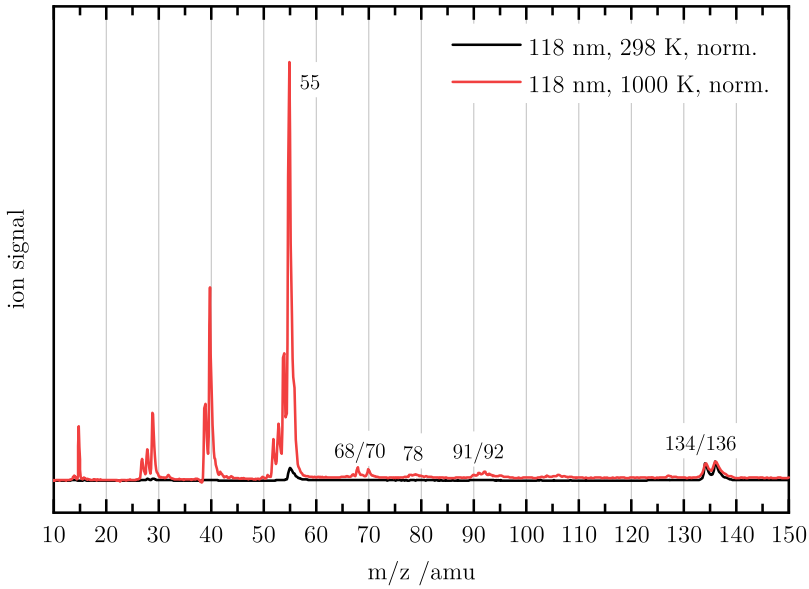

Figure S2. 118 nm TOF mass spectra recorded with (1000 K) and without (298 K) pyrolysis showing only small contributions of dissociative photoionization. Adapted from Ref. [1] with permission from the PCCP Owner Societies.

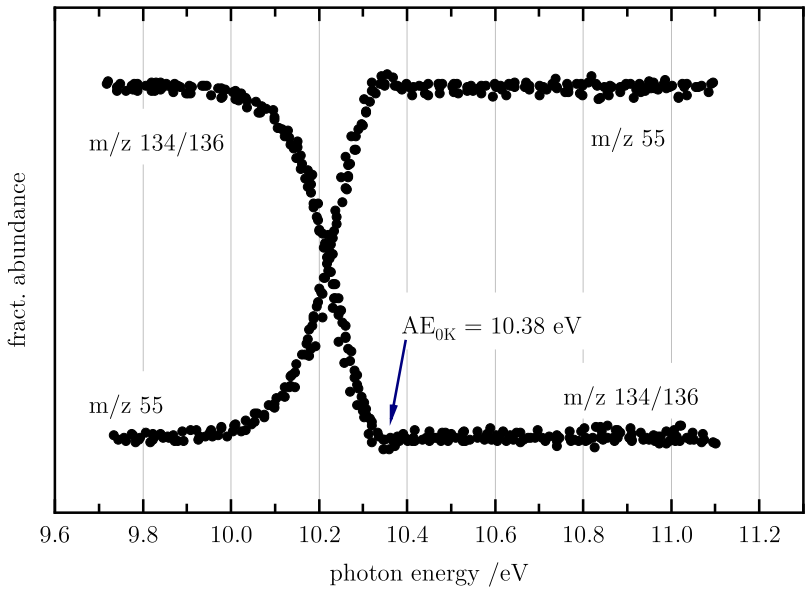

Figure S3. Breakdown diagram of 3-bromo-2-methylpropene, taken from Ref. [2] yielding an $AE_{0K}(C_4H_7Br, C_4H_7^+) = 10.38$ eV. Adapted from Ref. [1] with permission from the PCCP Owner Societies.

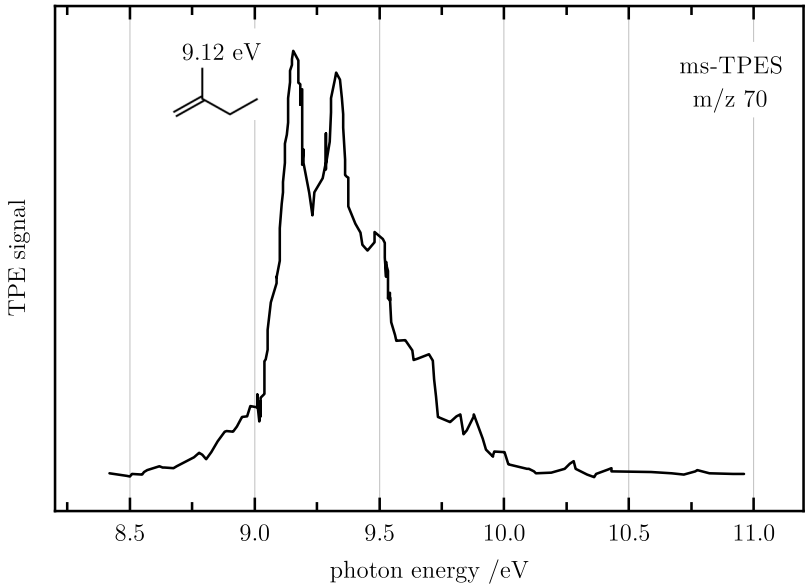

Figure S4. Mass-selected threshold photoelectron spectrum (TPES) of m/z 70 recorded under comparable experimental conditions in the pyrolysis of 3-bromo-2-methylpropene.[2] 2-Methyl-1-butene is identified based on a comparison with a literature spectrum.[3] Adapted from Ref. [1] with permission from the PCCP Owner Societies.

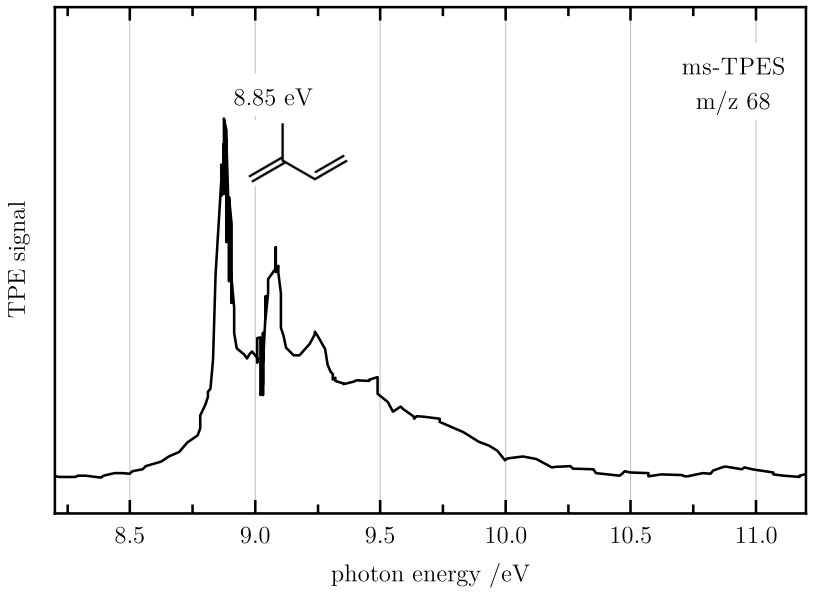

Figure S5. Mass-selected threshold photoelectron spectrum (TPES) of m/z 68 recorded under comparable experimental conditions in the pyrolysis of 3-bromo-2-methylpropene.[2] 2-Methyl-1,3-butadiene (isoprene) is identified by comparison with a published photoelectron spectrum.[4] Adapted from Ref. [1] with permission from the PCCP Owner Societies.

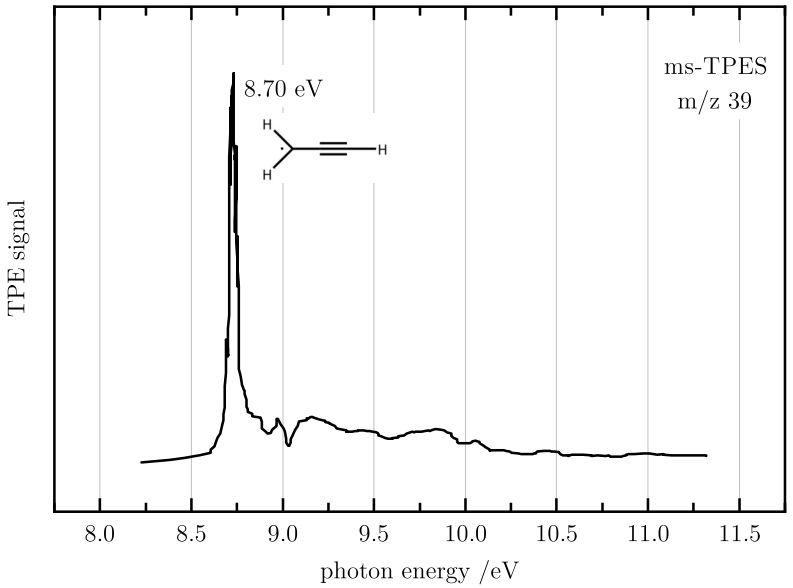

Figure S6. Mass-selected threshold photoelectron spectrum (TPES) of m/z 39 recorded under comparable experimental conditions of the pyrolysis of 3-bromo-2-methylpropene.[2] Propargyl is identified based on the comparison with a previous TPES.[5] Adapted from Ref. [1] with permission from the PCCP Owner Societies.

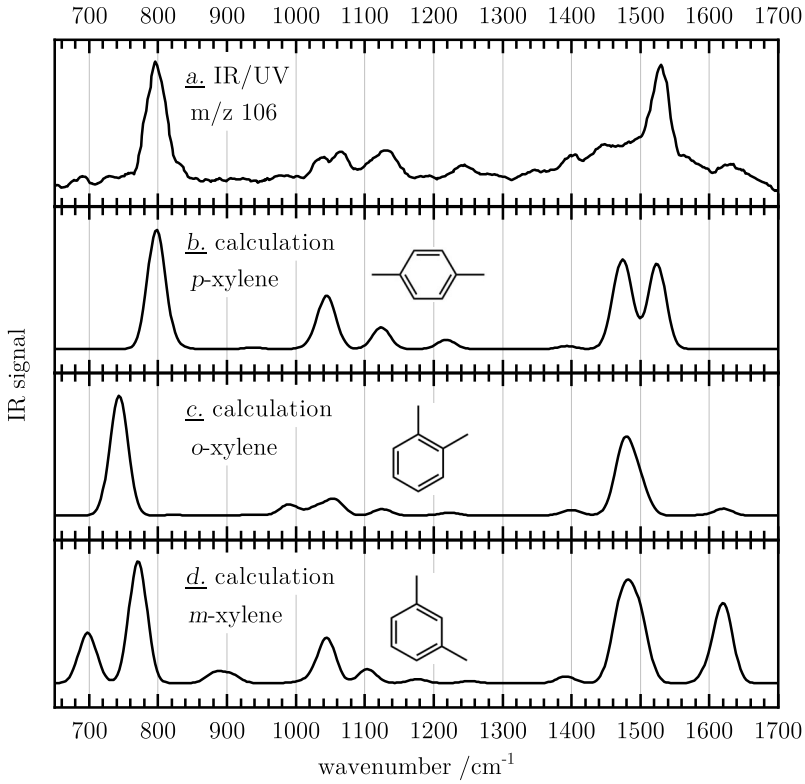

Figure S7. The IR/UV spectrum of m/z 106 (trace a) in comparison with computed IR spectra of *para*-, *ortho*- and *meta*-xylene (traces b-d). The carrier of the experimental spectrum is unambiguously identified as *para*-xylene. All computations predict the band positions well but overestimate the intensities of a few bands. To substantiate the assignment, a gas-phase FT-IR spectra was recorded (see Figure 3.4b), and excellent agreement is observed. Adapted from Ref. [1] with permission from the PCCP Owner Societies.

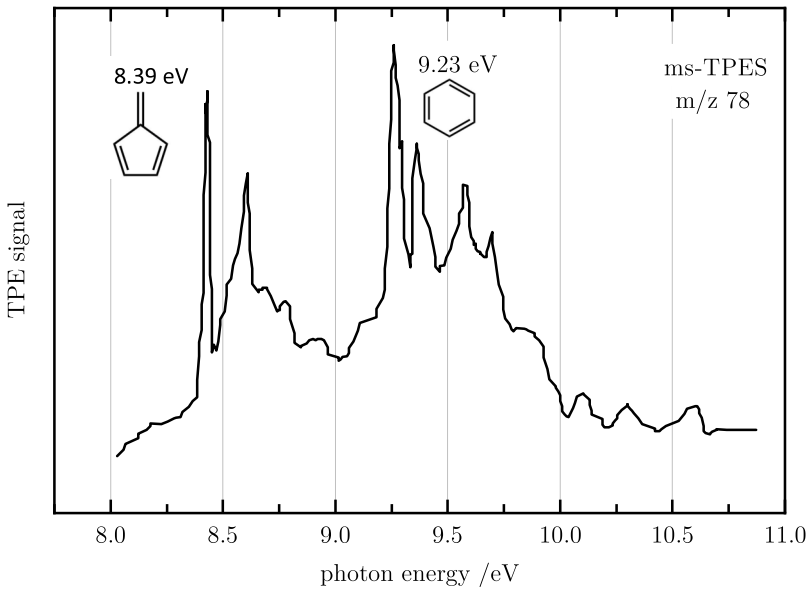

Figure S8. Mass-selected threshold photoelectron spectrum (TPES) of m/z 78 recorded under comparable experimental conditions in the pyrolysis of 3-bromo-2-methylpropene.[2] The two isomers fulvene and benzene are identified based on their ionization energies[6] as well as a previous TPES.[7] Adapted from Ref. [1] with permission from the PCCP Owner Societies.

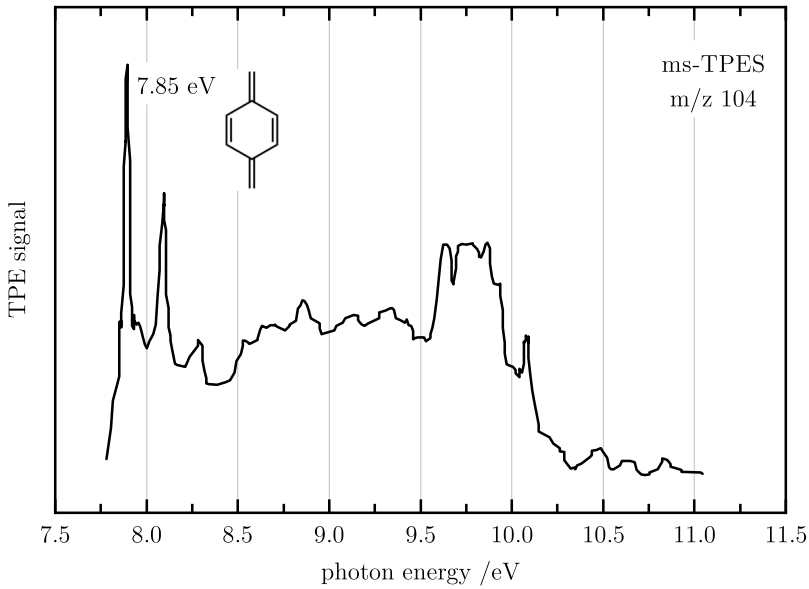

Figure S9. Mass-selected threshold photoelectron spectrum (TPES) of m/z 104 recorded under comparable experimental conditions in the pyrolysis of 3-bromo-2-methylpropene.[2] *Para*-xylylene is identified based on its ionization potential and a Franck-Condon simulation.[8] Adapted from Ref. [1] with permission from the PCCP Owner Societies.

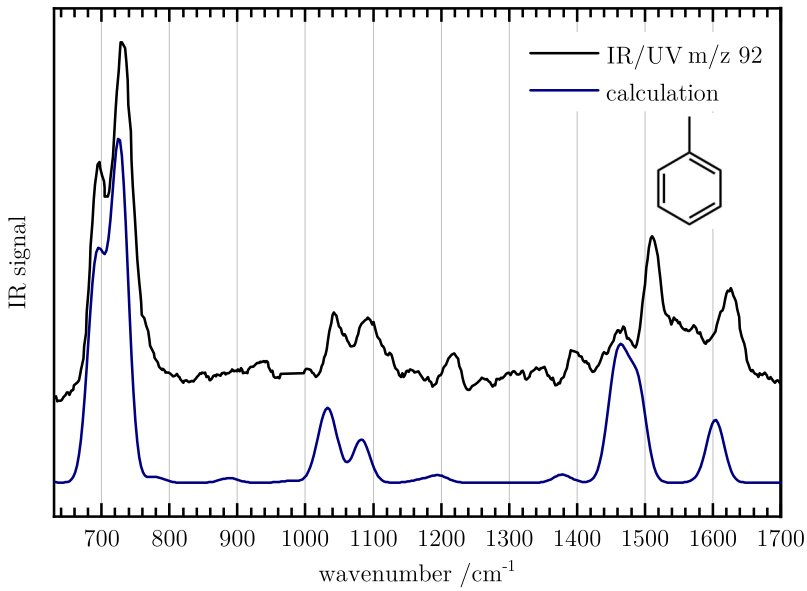

Figure S10. The carrier of the mass signal at m/z 92 is unambiguously identified as toluene by comparison with a computed IR spectrum. Adapted from Ref. [1] with permission from the PCCP Owner Societies.

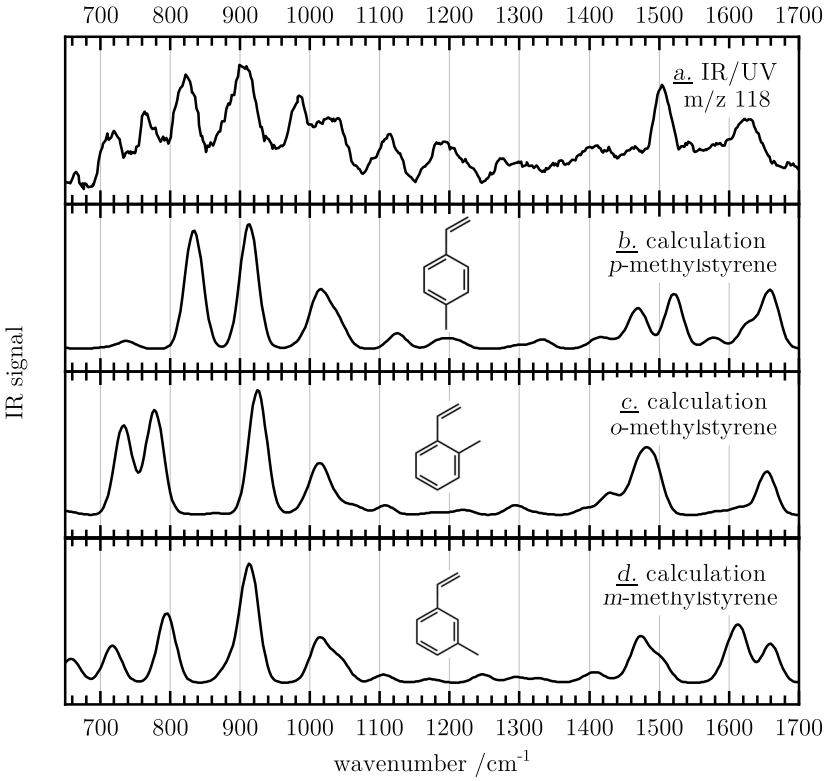

Figure S11. The IR/UV spectrum of m/z 118 (trace a) in comparison with computed IR spectra of methylated styrene isomers. The formation of *para*- and *ortho*-methylstyrene (traces b and c) is confirmed by the experimental data, while signals of the *meta* isomer cannot be identified (d). Adapted from Ref. [1] with permission from the PCCP Owner Societies.

B Supplementary Information for Published Work on 2-Phenylallyl Radicals

This section is adapted from

T. Preitschopf, F. Sturm, I. Stroganova, A. K. Lemmens, A. M. Rijs, I. Fischer, *Chem. Eur. J.* **2023**, *29*, e202202943

with permission from Wiley.

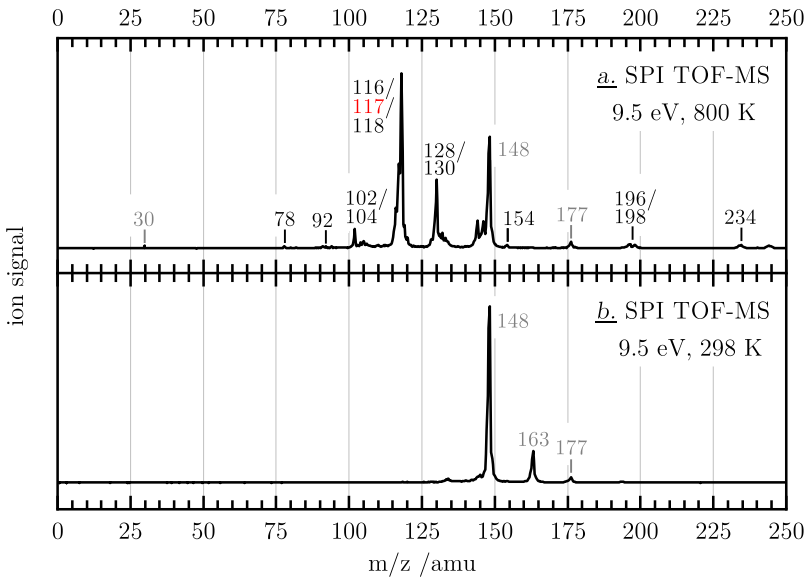

Figure S12. Time-of-flight mass spectra (TOF-MS) of **1** with (trace a) and without (b) pyrolysis recorded at 9.5 eV in a single-photon ionization process (SPI) at the Swiss Light Source (SLS). The signal at m/z 148 (traces a and b) is allocated to 3-phenylbut-3-en-1-ol, one of the reactants used in the synthesis of **1**, and m/z 163 (b) is traced back to another impurity in the precursor sample. An absent signal at m/z 117 in the lower spectrum emphasizes that **2** in trace a is not caused by dissociative photoionization (DPI). Adapted from Ref. [9] with permission from Wiley.

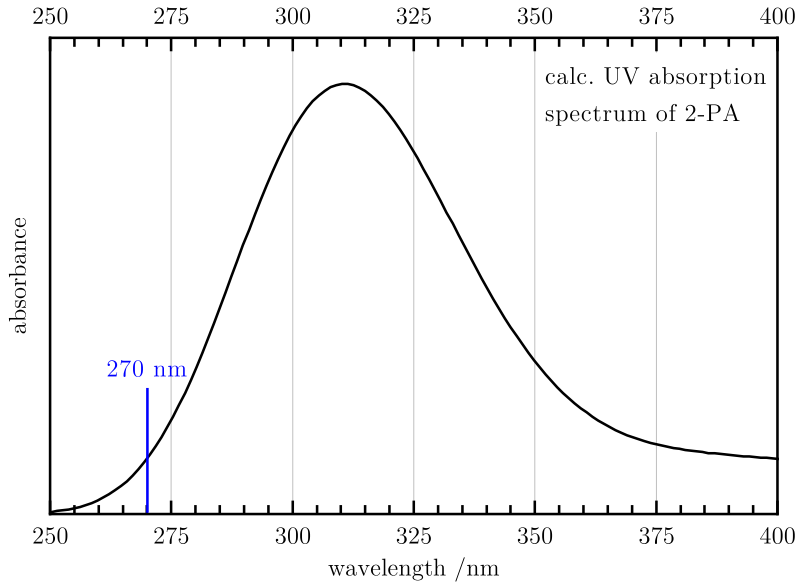

Figure S13. Computed TD-DFT UV absorption spectrum of **2** calculated at the B3LYP/6-311++G** level of theory. Adapted from Ref. [9] with permission from Wiley.

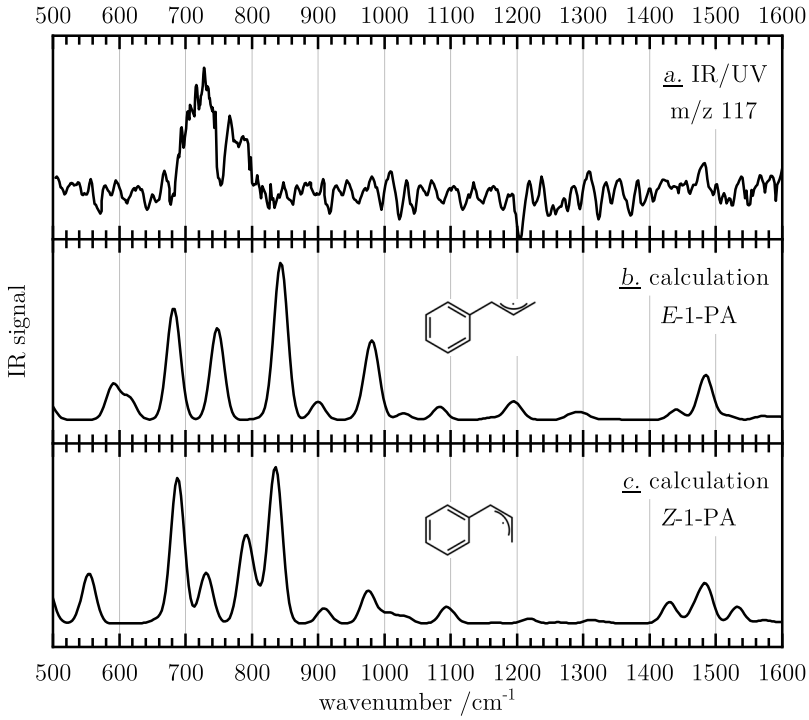

Figure S14. Comparison of the experimental IR/UV spectrum of m/z 117 (trace a) with computed IR spectra (b and c) shows that isomerization to the *E*- and *Z*-1-phenylallyl radical does not occur in the pyrolysis of **1** under the experimental conditions. Adapted from Ref. [9] with permission from Wiley.

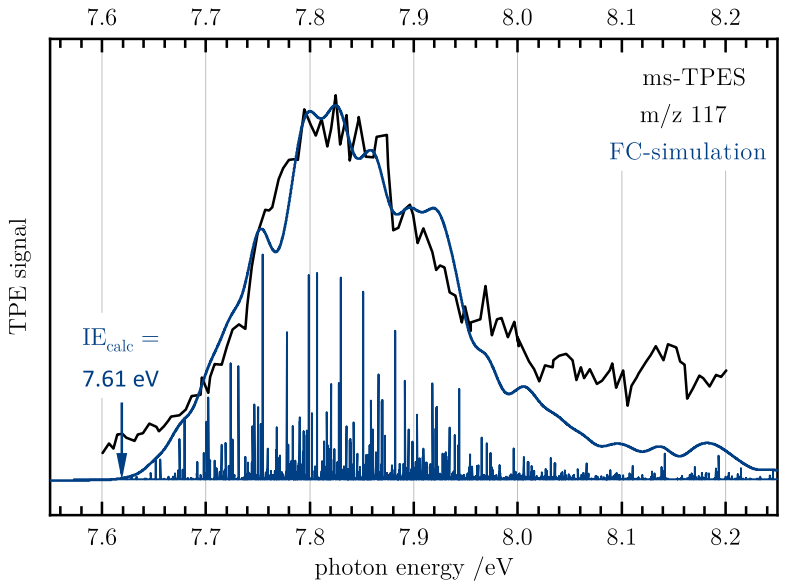

Figure S15. Threshold photoelectron spectrum (TPES) of **2** (black) in comparison with a Franck-Condon simulation (blue, based on DFT computations using the UωB97XD functional and a 6-311++G(d,p) basis set). The measurements were conducted at the VUV beamline of the Swiss Light Source (SLS), using the double imaging CRF-PEPICO spectrometer with a step size of 0.005 eV and an averaging time of 420 s.[10] Precursor **1** was heated to around 330 K in an in-vacuum sample container and cleaved by pyrolysis at around 800 K. Hardly any vibrational progression is identified, indicating a significant geometry change upon ionization. Therefore, only an approximate adiabatic IE of 7.6±0.1 eV is determined, in agreement with the computed IE of 7.61 eV. Adapted from Ref. [9] with permission from Wiley.

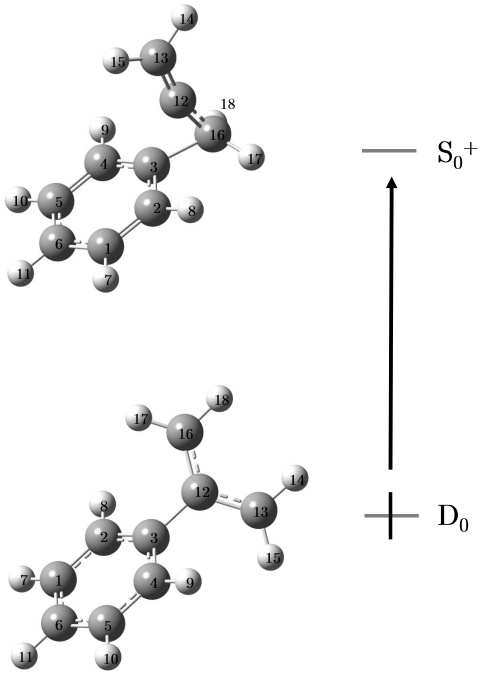

Figure S16. Geometry optimizations using DFT show, that a large geometry change is observed upon ionization for the cation of **2** in comparison with the neutral radical, resulting in a broad TPE spectrum (Figure S15). The geometries were optimized at the UωB97XD/6-311++G(d,p) level of theory. Selected bond lengths and angles are presented in Table S1. Adapted from Ref. [9] with permission from Wiley.

Table S1. Selected bond lengths and angles of **2** and the corresponding cation. Adapted from Ref. [9] with permission from Wiley.

Coordinate	Neutral radical	Cation
C13-C12	1.387 Å	1.304 Å
C12-C16	1.387 Å	1.395 Å
C3-C12	1.493 Å	1.641 Å
C3-C16	2.485 Å	1.608 Å
C3-C12-C16	119.24°	63.35°
C16-C12-C13	121.52°	163.26°
H18-C16-C13-H14 (dihedral)	2.16°	72.81°

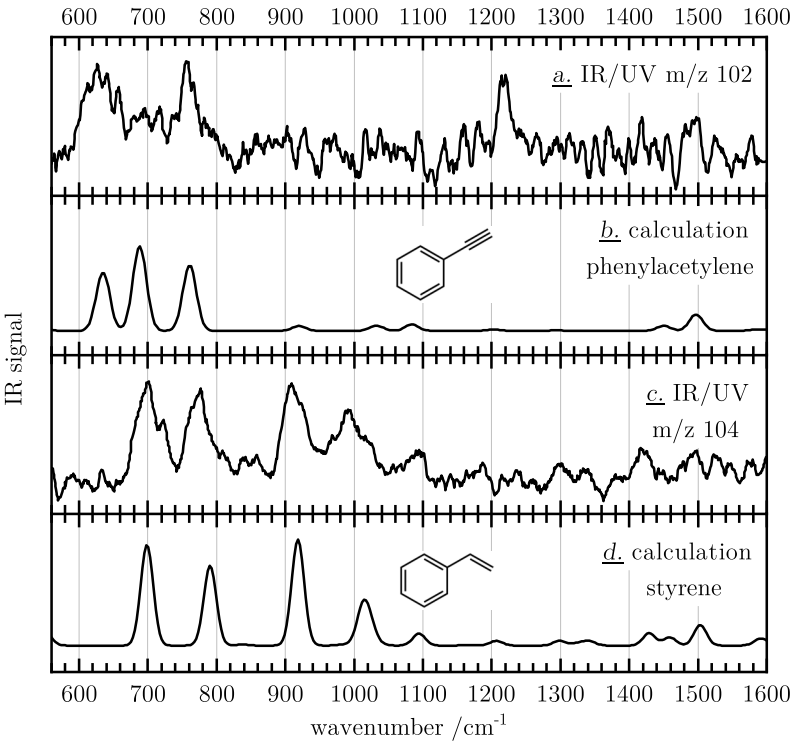

Figure S17. The IR/UV spectrum of m/z 102 (trace a) is assigned to phenylacetylene (b). The band at 1218 cm^{-1} is not predicted by the low-level harmonic frequency computation, but is characteristic for overtones and/or combination bands of the ≡CH bending mode.[11] The spectrum of m/z 104 (c) is identified as styrene (d). Adapted from Ref. [9] with permission from Wiley.

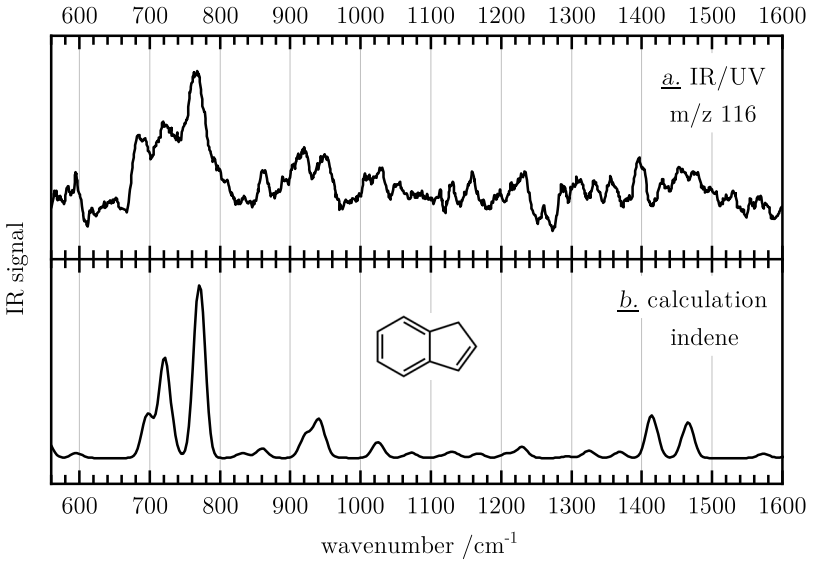

Figure S18. Based on comparison with computations (trace b), the IR/UV spectrum of m/z 116 (a) is assigned to indene. Adapted from Ref. [9] with permission from Wiley.

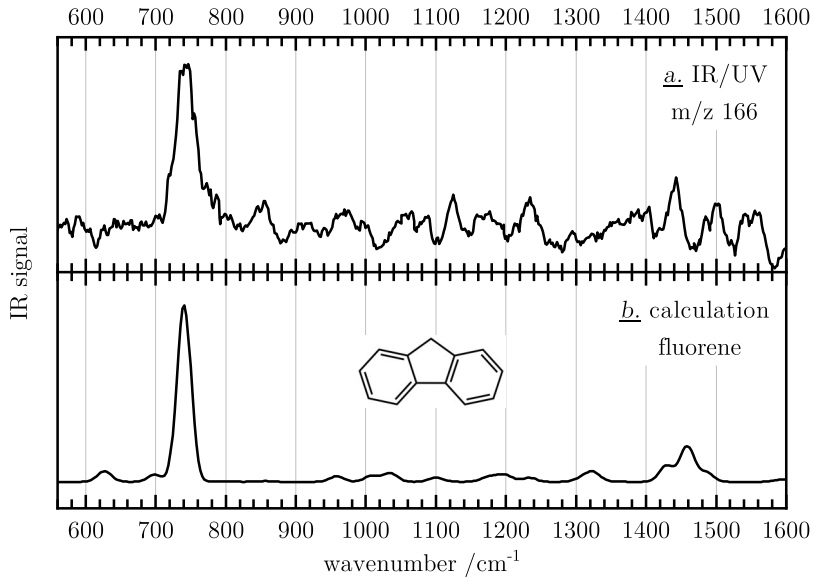

Figure S19. The carrier of the spectrum of m/z 166 (trace a) is identified as fluorene (b). Adapted from Ref. [9] with permission from Wiley.

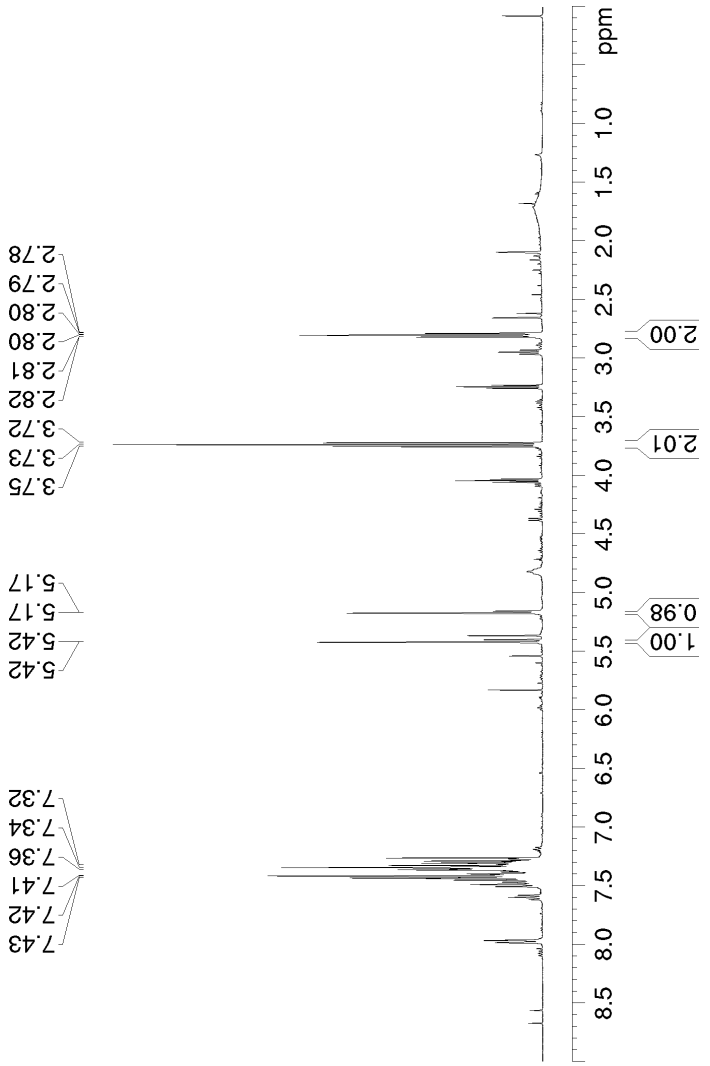

Figure S20. The ^{1}H-NMR spectrum (400 MHz) of **1** reveals some impurities in the sample. However, as shown in the SPI TOF-MS of the precursor sample (see Figure S12), only two impurities at m/z 148 and m/z 163 are transferred into the gas-phase and thus might interfere in the chemistry of the reactor. Yet, the identified reaction products are clearly connected to the chemistry of 2-PA resulting in a proposed reaction mechanism (Scheme 4.2) that is supported by theoretical work, see *e.g.*, Ref. [12]. Adapted from Ref. [9] with permission from Wiley.

C Supplementary Information for Published Work on the Structure of Azaphenanthrene Dimers

This section is adapted from

X. Miao, T. Preitschopf, F. Sturm, I. Fischer, A. K. Lemmens, M. Limbacher, R. Mitric, *J. Phys. Chem. Lett.* **2022**, *13*, 8939–8944.

Experimental

The experiments were performed at the FELIX free electron laser laboratory[13] at the Radboud University, Nijmegen, The Netherlands. Without further purification, benzo[f]quinoline (98 %, TCI Chemicals) and phenanthridine (98 %, Sigma-Aldrich), were resistively heated to 130 °C in an in-vacuum molecular beam source, seeded in argon (1.1 bar), and expanded into a differentially pumped vacuum apparatus[14] using a solenoid valve pulsed at 20 Hz (Series 9, Parker General Valve). The supersonically cooled jet was skimmed and delivered vibrationally and rotationally cold molecules to the interaction region of a reflectron time-of-flight mass spectrometer[14] (R. M. Jordan Co.). Here, the molecular jet interacted with two perpendicular UV laser beams and counterpropagating FEL-IR radiation. Excitation and ionization was provided by a Nd:YAG-laser pumped dye laser (∼3 mJ/pulse, Lioptec), and an 193 nm ArF excimer laser (∼100 μJ/pulse, Neweks), respectively, to perform two-colour [1+1']-REMPI. The excitation wavelength was set to 342.33 nm for benzo[f]quinoline and 340.86 nm for phenanthridine; both red-shifted with respect to the $S_1 \leftarrow S_0$ transitions of the corresponding monomers[15] (see Figure S21 and Figure S23). Additionally, a UV wavelength of 280.7 nm was used for benzo[f]quinoline and one-colour [1+1]-REMPI was performed. FEL-IR radiation between 180 and 1750 cm^{-1} was employed for benzo[f]quinoline and between 390 and 1760 cm^{-1} for phenanthridine. It was tuned in steps of 1 cm^{-1}. Typically, FELIX[13] has a bandwidth of 1 % of the central photon frequency with pulse energies (10 μs pulse) ranging from 25 mJ for the FIR- to 150 mJ for the MIR-region. To perform IR/UV ion dip spectroscopy, FELIX was set around 200 ns prior to the UV lasers and operated at half the repetition rate of the UV lasers (20 Hz) to gain alternating IR-ON/IR-OFF ion yields. The mass-selected IR spectra were obtained by dividing the IR-OFF signal by the IR-ON signal, taking the decadic logarithm and correcting for IR laser power.

Theory

All computations were carried out in the framework of density functional theory (DFT), using the hybrid ωB2GP-PLYP functional[16] as implemented in the ORCA software package[17] combined with the def2-TZVP basis set[18] and D4 dispersion correction.[19,20] The geometries for H-bridge connected dimers were optimized using DFT starting from structures constructed with Etter's rules.[21] The geometries for π-stacks were obtained by first optimizing the two parallel displaced π-stack structures at DFT-level. Then, both structures were propagated for 500 ps at 300 K with Langevin dynamics using TorchANI[22] along with ASE.[23] A total of 2000 geometries were selected equidistantly along each trajectory after reaching equilibrium and optimized with TorchANI to find the local minimum with the lowest energy. These computations were carried out using the ANI-1ccx model.[24] The obtained structures were further optimized using DFT. In this way, four different local minima were found for both azaphenanthrenes. The IR spectra were simulated by performing harmonic frequency analysis at DFT level using ωB2GP-PLYP-D4/def2-TZVP. The resulting stick spectra were convolved with a Gaussian-shaped function with σ=2 cm^{-1} and scaled with a factor of 0.96.[25]

Supporting Figures

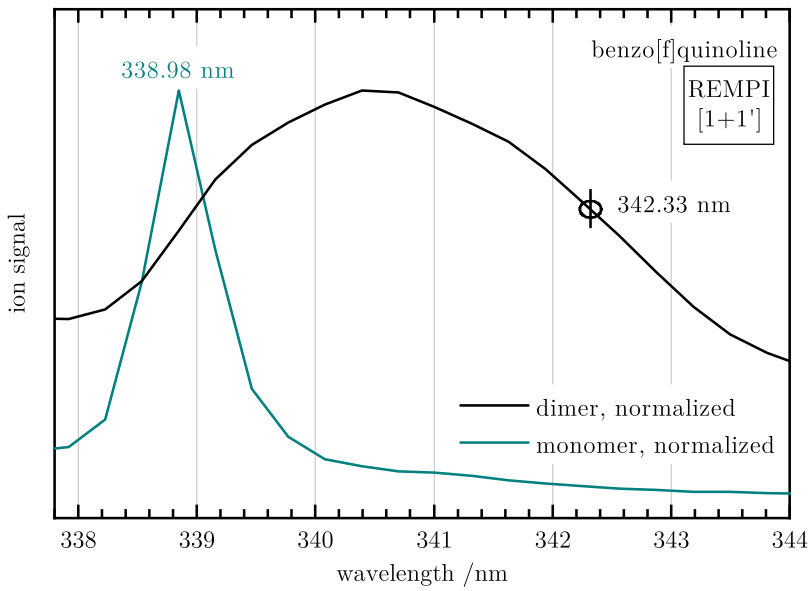

Figure S21. [1+1']-REMPI spectrum of the monomer and dimer of benzo[f]quinoline corresponding to the $S_1 \leftarrow S_0$ transition (normalized). At 342.33 nm, excitation of the monomer is avoided. Adapted with permission from Ref. [26]. Copyright 2022 American Chemical Society.

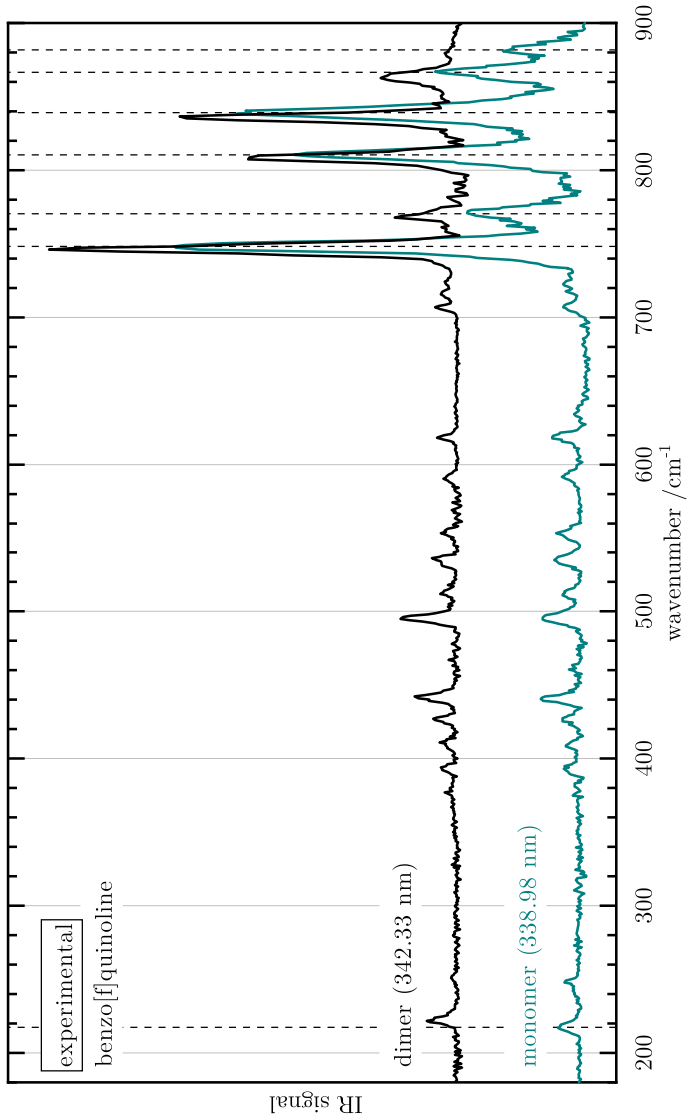

Figure S22. Comparison of the IR/UV spectrum of the monomer of benzo[f]quinoline excited at 338.98 nm with the IR/UV spectrum of the dimer excited at 342.33 nm (see Figure S21). Subtle differences are observed, in particular a red-shift of the dimer vibrational bands in the region between 700-900 cm^{-1}. The bands are mostly due to CH out-of-plane wagging vibrations. Adapted with permission from Ref. [26]. Copyright 2022 American Chemical Society.

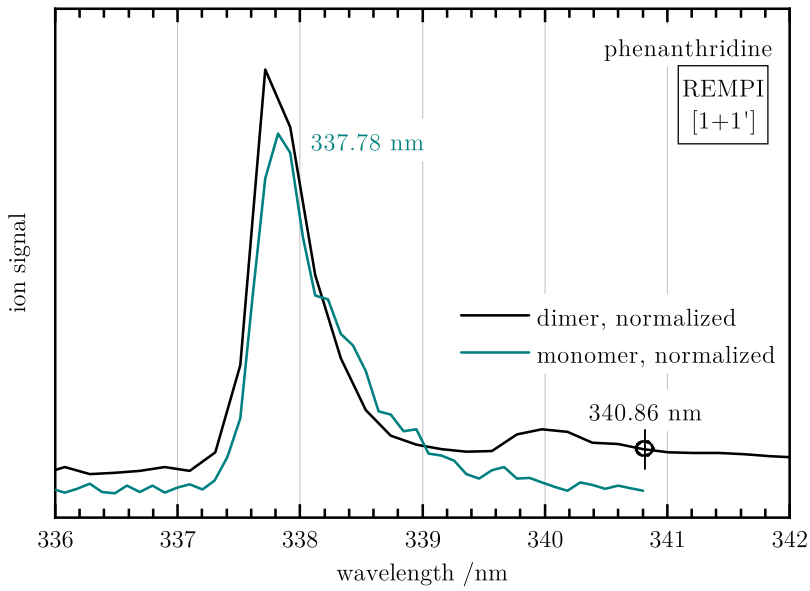

Figure S23. [1+1']-REMPI spectrum of the monomer and dimer of phenanthridine corresponding to the $S_1 \leftarrow S_0$ transition (normalized). At 340.86 nm, excitation of the monomer is avoided. Adapted with permission from Ref. [26]. Copyright 2022 American Chemical Society.

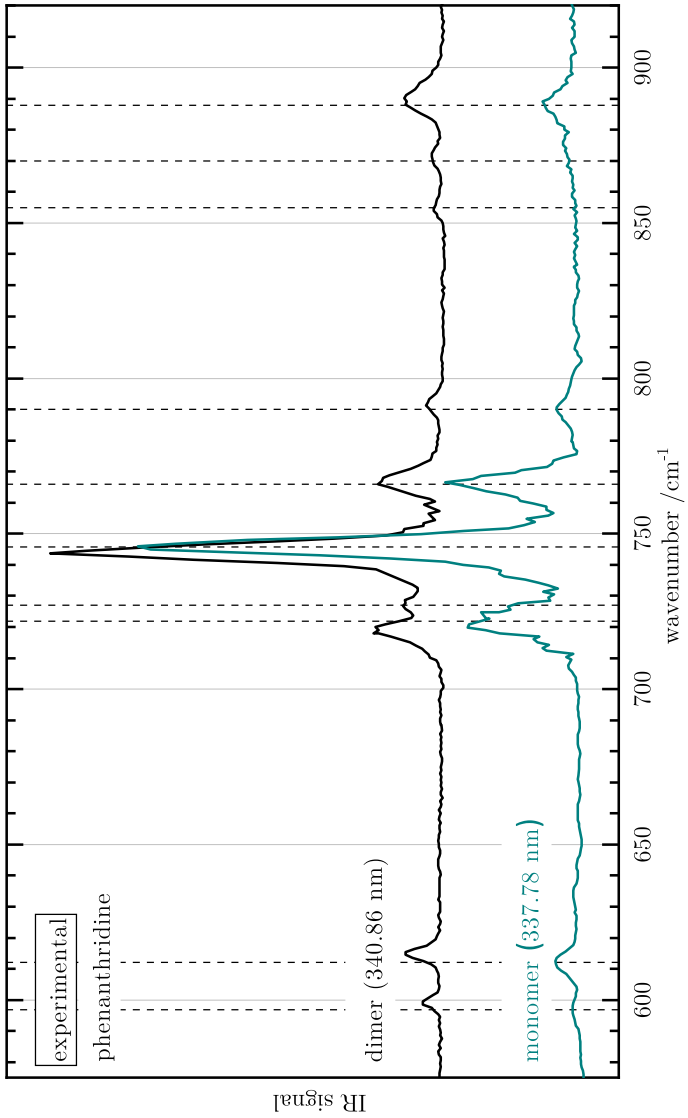

Figure S24. Comparison of the IR/UV spectrum of the monomer of phenanthridine excited at 337.78 nm with the IR/UV spectrum of the dimer excited at 340.86 nm (see Figure S23). Small red-shifts of the vibrational bands of the dimer are observed. Adapted with permission from Ref. [26]. Copyright 2022 American Chemical Society.

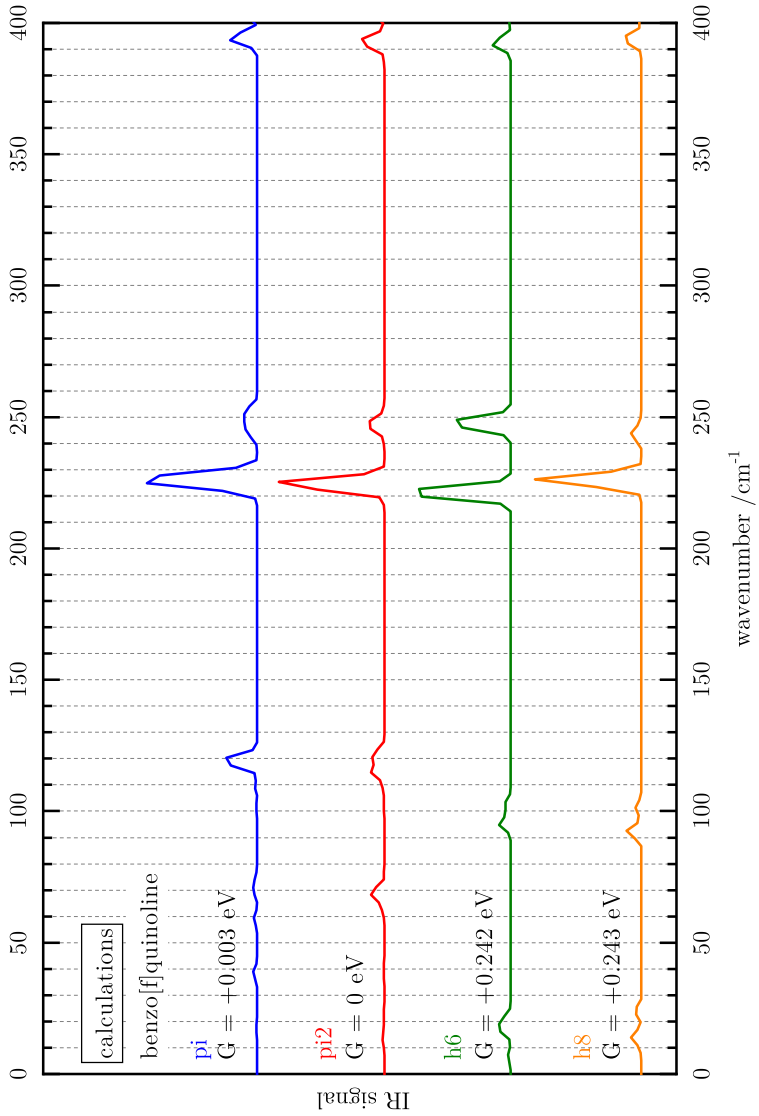

Figure S25. Computed IR spectra in the FIR region to highlight the intermolecular modes of the four lowest energy dimers of benzo[f]quinoline. Adapted with permission from Ref. [26]. Copyright 2022 American Chemical Society.

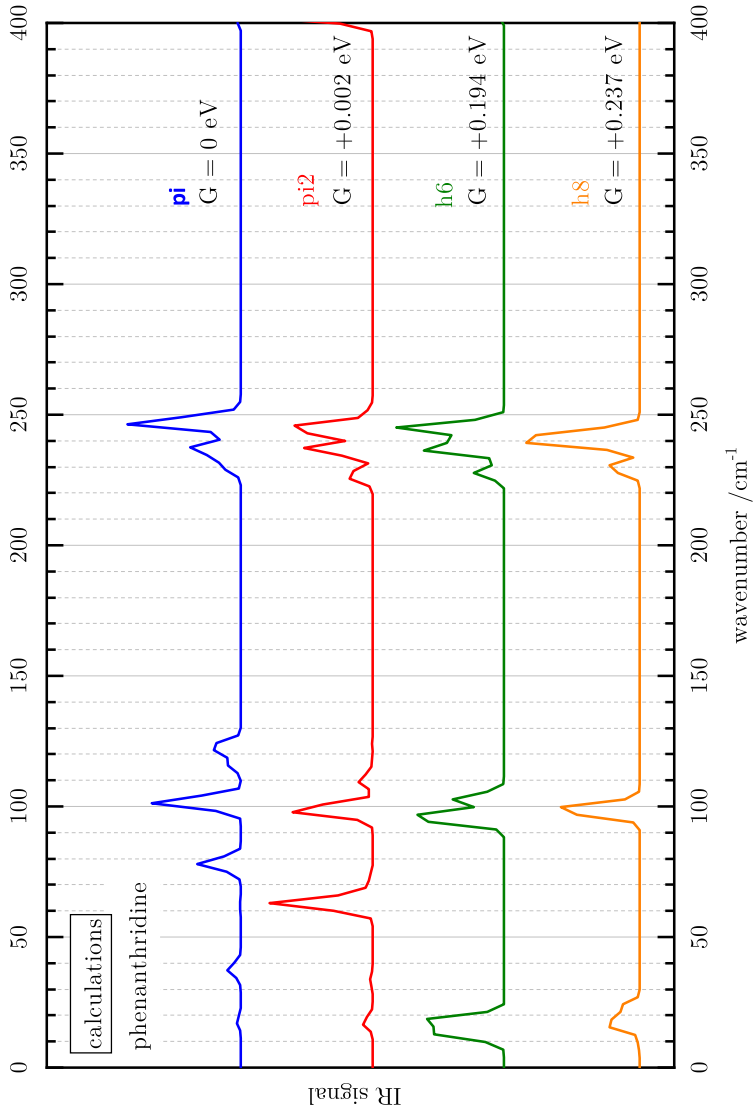

Figure S26. Computed IR spectra in the FIR region to highlight the intermolecular modes of the four lowest energy dimers of phenanthridine. Adapted with permission from Ref. [26]. Copyright 2022 American Chemical Society.

Supporting Tables

Table S2. Dimeric binding energy of π-stacks with and without counterpoise (CP) correction.[27] Adapted with permission from Ref. [26]. Copyright 2022 American Chemical Society.

Dimer	Structure	E_B /eV	E_B^{CP} /eV
benzo[f]quinoline	pi	-0.448	-0.362
	pi2	-0.449	-0.365
phenanthridine	pi	-0.439	-0.351
	pi2	-0.434	-0.352

References

[1] T. Preitschopf, F. Hirsch, A. K. Lemmens, A. M. Rijs, I. Fischer, *Phys. Chem. Chem. Phys.* **2022**, *24*, 7682–7690.

[2] M. Lang, PhD thesis, University of Wuerzburg, Wuerzburg, **2015**.

[3] J. Pieper, S. Schmitt, C. Hemken, E. Davies, J. Wullenkord, A. Brockhinke, J. Kruger, G. A. Garcia, L. Nahon, A. Lucassen, W. Eisfeld, K. Kohse-Höinghaus, *Z. Phys. Chem.* **2018**, *232*, 153–187.

[4] G. Martins, A. M. Ferreira-Rodrigues, F. N. Rodrigues, G. G. B. d. Souza, N. J. Mason, S. Eden, D. Duflot, J.-P. Flament, S. V. Hoffmann, J. Delwiche, M.-J. Hubin-Franskin, P. Limão-Vieira, *Phys. Chem. Chem. Phys.* **2009**, *11*, 11219–11231.

[5] P. Hemberger, M. Lang, B. Noller, I. Fischer, C. Alcaraz, B. K. Cunha de Miranda, G. A. Garcia, H. Soldi-Lose, *J. Phys. Chem. A* **2011**, *115*, 2225–2230.

[6] E. Heilbronner, R. Gleiter, H. Hopf, V. Hornung, A. de Meijere, *Helv. Chim. Acta* **1971**, *54*, 783–794.

[7] Z. Pan, A. Puente-Urbina, A. Bodi, J. A. v. Bokhoven, P. Hemberger, *Chem. Sci.* **2021**, *12*, 3161–3169.

[8] P. Hemberger, A. J. Trevitt, T. Gerber, E. Ross, G. da Silva, *J. Phys. Chem. A* **2014**, *118*, 3593–3604.

[9] T. Preitschopf, F. Sturm, I. Stroganova, A. K. Lemmens, A. M. Rijs, I. Fischer, *Chem. Euro. J.* **2023**, *29*, e202202943.

[10] B. Sztáray, K. Voronova, K. G. Torma, K. J. Covert, A. Bodi, P. Hemberger, T. Gerber, D. L. Osborn, *J. Chem. Phys.* **2017**, *147*, 013944.

[11] R. A. Nyquist, W. J. Potts, *Spectrochim. Acta* **1960**, *16*, 419–427.

[12] L. Vereecken, J. Peeters, *Phys. Chem. Chem. Phys.* **2003**, *5*, 2807–2817.

[13] D. Oepts, A. F. G. van der Meer, P. W. van Amersfoort, *Infrared Phys. Technol.* **1995**, *36*, 297–308.

[14] A. M. Rijs, J. Oomens, *Top. Curr. Chem.* **2014**, *364*, 1–42.

[15] J. Prochorow, I. Deperasińska, Y. Stepanenko, *Chem. Phys. Lett.* **2004**, *399*, 239–246.

[16] M. Casanova-Páez, M. B. Dardis, L. Goerigk, *J. Chem. Theory Comput.* **2019**, *15*, 4735–4744.

[17] F. Neese, *WIREs Comput. Mol. Sci.* **2012**, *2*, 73–78.

[18] F. Weigend, R. Ahlrichs, *Phys. Chem. Chem. Phys.* **2005**, *7*, 3297–3305.

[19] E. Caldeweyher, C. Bannwarth, S. Grimme, *J. Chem. Phys.* **2017**, *147*, 034112.

[20] A. Najibi, M. Casanova-Páez, L. Goerigk, *J. Phys. Chem. A* **2021**, *125*, 4026–4035.

[21] M. C. Etter, *Acc. Chem. Res.* **1990**, *23*, 120–126.

[22] X. Gao, F. Ramezanghorbani, O. Isayev, J. S. Smith, A. E. Roitberg, *J. Chem. Inf. Model.* **2020**, *60*, 3408–3415.

[23] A. H. Larsen, J. J. Mortensen, J. Blomqvist, I. E. Castelli, R. Christensen, M. Dulak, J. Friis, M. N. Groves, B. Hammer, C. Hargus, E. D. Hermes, P. C. Jennings, P. B. Jensen, J. Kermode, J. R. Kitchin, E. L. Kolsbjerg, J. Kubal, K. Kaasbjerg, S. Lysgaard, J. B. Maronsson, T. Maxson, T. Olsen, L. Pastewka, A. Peterson, C. Rostgaard, J. Schiøtz, O. Schütt, M. Strange, K. S. Thygesen, T. Vegge, L. Vilhelmsen, M. Walter, Z. Zeng, K. W. Jacobsen, *J. Phys: Condens. Matter* **2017**, *29*, 273002.

[24] J. S. Smith, B. T. Nebgen, R. Zubatyuk, N. Lubbers, C. Devereux, K. Barros, S. Tretiak, O. Isayev, A. E. Roitberg, *Nat. Commun.* **2019**, *10*, 2903.

[25] M. A. Palafox, *J. Phys. Chem. A* **1999**, *103*, 11366–11377.

[26] X. Miao, T. Preitschopf, F. Sturm, I. Fischer, A. K. Lemmens, M. Limbacher, R. Mitric, *J. Phys. Chem. Lett.* **2022**, 8939–8944.

[27] S. Boys, F. Bernardi, *Mol. Phys.* **1970**, *19*, 553–566.

LIST OF FIGURES

LIST OF SCHEMES

LIST OF TABLES

ERKLÄRUNGEN ZU AUTORENSCHAFTEN

Julius-Maximilians-
UNIVERSITÄT
WÜRZBURG

Fakultät für
CHEMIE UND
PHARMAZIE

Erklärung zur Autorenschaft

The gas-phase infrared spectra of the 2-methylallyl radical and its high-temperature pyrolysis products
T. Preitschopf, F. Hirsch, A. K. Lemmens, A. M. Rijs, and I. Fischer, *Phys. Chem. Chem. Phys.*, **2022**, *24*, 7682-7690.

Tobias Preitschopf (TP), Florian Hirsch (FH), Alexander K. Lemmens (AKL), Anouk M. Rijs (AMR), Ingo Fischer (IF)

Autor	TP	FH	AKL	AMR	IF	∑ in Prozent
Laser experiments (Würzburg)	70%	20%			10%	100%
FEL experiments (Nijmegen)	33%	33%	33%			100%
Analysis of data	90%	10%				100%
Discussion of results	40%			30%	30%	100%
Writing	60%				40%	100%
Summe	58%	13%	7%	6%	16%	100%

Figure 27. Erklärung zur Autorenschaft für das Paper T. Preitschopf, F. Hirsch, A. K. Lemmens, A. M. Rijs, I. Fischer, *Phys. Chem. Chem. Phys.* **2022**, *24*, 7682–7690.

Julius-Maximilians-
UNIVERSITÄT
WÜRZBURG

Fakultät für
CHEMIE UND
PHARMAZIE

Erklärung zur Autorenschaft

IR/UV Double Resonance Study of the 2-Phenylallyl Radical and its Pyrolysis Products
T. Preitschopf, F. Sturm, I. Stroganova, A. K. Lemmens, A. M. Rijs, and I. Fischer, *Chem. Eur. J.*, **2023**, *29*, e202202943.

Tobias Preitschopf (TP), Floriane Sturm (FS), Iuliia Stroganova (IS), Alexander K. Lemmens (AKL), Anouk M. Rijs (AMR), Ingo Fischer (IF)

Autor	TP	FS	IS	AKL	AMR	IF	∑ in Prozent
Laser experiments (Würzburg)	80%					20%	100%
Synthesis		100%					100%
FEL experiments (Nijmegen)	30%	30%	30%	10%			100%
Analysis of data	100%						100%
Discussion of results	40%				30%	30%	100%
Writing	60%					40%	100%
Summe	52%	21%	5%	2%	5%	15%	100%

Figure 28. Erklärung zur Autorenschaft für das Paper T. Preitschopf, F. Sturm, I. Stroganova, A. K. Lemmens, A. M. Rijs, I. Fischer, *Chem. Eur. J.* **2023**, *29*, e202202943.

Julius-Maximilians-
UNIVERSITÄT
WÜRZBURG

Fakultät für
CHEMIE UND
PHARMAZIE

Erklärung zur Autorenschaft

Stacking is Favored over Hydrogen Bonding in Azaphenanthrene Dimers
X. Miao, T. Preitschopf, F. Sturm, I. Fischer, A. K. Lemmens, M. Limbacher, and R. Mitric, *J. Chem. Phys. Lett.*, **2022**, *13*, 8939-8944.

Xincheng Miao (XM), Tobias Preitschopf (TP), Floriane Sturm (FS), Ingo Fischer (IF), Alexander K. Lemmens (AKL), Moritz Limbacher (ML), Roland Mitric (RM)

Autor	XM	TP	FS	IF	AKL	ML	RM	∑ in Prozent
Laser experiments (Würzburg)		20%	80%					100%
Theory	80%					10%	10%	100%
FEL experiments (Nijmegen)		33%	33%		33%			100%
Analysis of data	10%	90%						100%
Discussion of results	30%	30%	5%	15%	5%		15%	100%
Writing		30%		50%			20%	100%
Summe	20%	33%	20%	11%	6%	2%	8%	100%

Figure 29. Erklärung zur Autorenschaft für das Paper X. Miao, T. Preitschopf, F. Sturm, I. Fischer, A. K. Lemmens, M. Limbacher, R. Mitric, *J. Phys. Chem. Lett.* **2022**, *13*, 8939–8944.

DANKSAGUNG

Ohne die tatkräftige Unterstützung einiger Personen wäre diese Arbeit nicht möglich gewesen. Daher möchte ich mich zum Schluss bei allen herzlich bedanken, die mir innerhalb der letzten vier Jahre stets zur Seite gestanden und häufig genug den Rücken freigehalten haben.

An erster Stelle möchte ich mich bei *Prof. Dr. Ingo Fischer* dafür bedanken, dass Du mir ein sehr spannendes und abwechslungsreiches Thema anvertraut hast. Obwohl mein damaliger wissenschaftlicher Hintergrund aufgrund meines Lehramtsstudiums "überschaubar" war, hast Du mir von Anfang an sämtliche Möglichkeiten gegeben, mich wissenschaftlich frei entfalten und ausprobieren zu können. Ich konnte jederzeit sowohl meine besseren als auch nicht so guten Ideen mit Dir in einem vertrauensvollen Rahmen diskutieren - in einem Maße, das sicher nicht selbstverständlich ist. Während der letzten vier Jahre habe ich gelernt, dass man durch harte Arbeit und mit der richtigen Führung sämtliche *Herausforderungen* meistern kann. Ich hoffe, dass ich diese Erkenntnis eines Tages ebenfalls weitergeben kann. Darüber hinaus hast Du mir die Möglichkeit gegeben, an zahlreichen Strahlzeiten an internationalen Großforschungseinrichtungen teilzunehmen, sowie mich auf (inter-)nationalen Tagungen auszutauschen, um auch interessante Einblicke außerhalb meines Themas zu erhalten. Vielen herzlichen Dank!

Des Weiteren gilt unseren Kooperationspartnern in Nimwegen (NL) ein großer Dank. Die Zusammenarbeit mit *Prof. Dr. Anouk M. Rijs* am FELIX Laboratorium war stets freundschaftlich, unkompliziert und immer von Erfolg gekrönt. Dabei gilt auch ihrem damaligen Doktoranden (und später eigenständigem Postdoc) *Dr. Alexander Lemmens* ein besonderes Dankeschön. Ohne Deine wertvollen Tipps sowie Deiner großen Begeisterung für unsere Forschung wären die gemeinsamen Strahlzeiten nicht annähernd so erfolgreich gewesen. Ich bin sicher, dass sich hier ein Kontakt gefunden hat, der sich weit über die Promotion hinaus hal-

ten wird! Im Zuge dessen möchte ich mich auch bei allen Mitarbeiter*innen von FELIX für die herzliche Aufnahme während der Strahlzeiten bedanken.

Bei unseren indischen Freunden *Prof. Dr. Animesh Ojha* und *Dr. Deb Pratim Mukhopadhyay* möchte ich mich für die gute wissenschaftliche Zusammenarbeit und die Einführung in die indische Küche bedanken. Ich hoffe, dass wir uns eines Tages auf indischem Bodem wiedersehen!

Ganz besonderer Dank gilt auch meinem Kollegen *Marius Gerlach*. Obwohl Dein Humor zumindest meiner Ansicht nach nicht witzig sein kann, hast Du mich dennoch fast täglich zum Lachen gebracht und für gute Laune im Arbeitskreis gesorgt. Viel wichtiger ist aber, dass sich der gesamte AK stets auf Dich verlassen konnte, nicht nur im Rahmen der Wissenschaft, sondern auch bei sämtlichen Aufgaben, die neben der täglichen Arbeit anfielen. Dabei hat sich über die letzten vier Jahre eine Freundschaft entwickelt, die sicher ein Leben lang halten wird.

Meinem langjährigen Bürokollegen *Christian Matthaei* gilt ebenfalls großer Dank. Gerade zu Beginn meiner Promotion hattest Du stets ein geduldiges Ohr für sämtliche Fragestellungen, die sich rund um die Spektroskopie und das Programmieren drehten. Zudem konnte ich mich im letzten Jahr Deiner Promotion großzügig in unserem Büro ausbreiten, ohne Dich dabei in Deiner Arbeit zu stören.

Meinem Laufteam *#DiesmalWirklichLangsam* in Form von *Jonas Fackelmayer* und *Klaus Hofmann* danke ich ebenfalls ganz herzlich für die zahlreichen Runden im Weinberg. Zum Glück waren wir uns immer einig, mit welcher Pace wir den *Teufelskeller*-Berg bezwingen wollten. Während ich Euch anfangs noch davonlaufen konnte, habt ihr mich mittlerweile leider schon seit Längerem überholt. Ich hoffe, dass wir uns dennoch jedes Jahr am Schwanberglauf wiedersehen, um unsere aktuelle Form zu testen.

Bei unserem Bierkapitän der Herzen *Dr. Marco Flock* bedanke ich mich für die vielen Momente, die wir abseits der Wissenschaft miteinander erleben und teilen konnten. *Dr. Engelbert Reusch* danke ich für die vielen lustigen Geschichten über das Leben, die Grünen, und die Landwirtschaft. Die Besuche auf eurem Hof hatten stets die Atmosphäre eines Kurzurlaubs. *Dr. Domenik Schleier* danke ich für seine außergewöhnlichen Insiderinformationen in die Tiefen der Chemiefakultät, die auch Jahre nach seiner Promotion nicht an Qualität verloren haben. Ich freue mich, dass es allen drei genauso wichtig ist wie mir, den Kontakt aufrechtzu-

erhalten. Bei meinem Vorgänger *Dr. Florian Hirsch* bedanke ich mich für die Einführung in das Thema und die erste Strahlzeit in den Niederlanden.

Weiterhin möchte ich mich bei *Dr. Hans-Christian Schmitt* dafür bedanken, dass er damals den Kontakt zum Arbeitskreis herstellte und mir so dabei half, bei Prof. Dr. Ingo Fischer promovieren zu können. Zudem war er maßgeblich daran beteiligt, dass ich meine zukünftige Anstellung bei Prof. Dr. Maik Finze antreten kann. Hansi, Du darfst mir auch gerne in Zukunft weitere Jobs vermitteln!

Bei meinen Kolleg*innen *Lilith Wohlfahrt*, *Dorothee Schaffner* und *Emil Karaev* möchte ich mich für die tolle Atmosphäre im AK bedanken. Ich bin sicher, dass uns das Teambuilding auf Mallorca nachhaltig zusammengeschweißt hat. Ich wünsche euch, dass ihr eine genauso tolle Zeit im AK erleben dürft wie ich. *Floriane Sturm* danke ich für drei erfolgreiche Strahlzeiten am FELIX Laboratorium - anfangs in voller Quarantäne im Guesthouse, aber letztlich dann doch noch zum Glück mit zahlreichen Ausflügen, u. a. bis ans Wattenmeer und ins Ruygh.

Ganz herzlich möchte ich mich auch bei meinen Bachelorant*innen *Denise Koppenhöfer* und *Lukas Faschingbauer* bedanken. Ich hoffe, dass man euch in Zukunft wieder im AKF antreffen wird!

Zudem geht auch ein großer Dank an meine Kooperationspartner*innen aus der TC und AC. Die Zusammenarbeit mit *Prof. Dr. Roland Mitric* und *Xincheng Miao* sowie *Prof. Dr. Crispin Lichtenberg* und *Dr. Jaqueline Ramler* war stets unkompliziert und ausgesprochen erfolgreich.

Ein lieber Dank gilt ebenfalls unserer Werkstatt, hier namentlich *Wolfgang Liebler*, *Katharina Wittmann*, *Ralf Kohrmann* und *Markus Keller*. Zudem möchte ich unserem Elektroniker *Uwe Reuss* für sein großes Engagement bedanken. Weiterhin gilt ein lieber Dank *Ivonne Vollert*, die immer wieder einen hilfreichen Blick auf unseren AK geworfen hat.

Zuletzt gilt mein größter Dank meinen Eltern *Uschi* und *Klaus*. Ihr habt mir seit jeher den Rücken freigehalten, mich permanent unterstützt und sämtliche Freiheiten ermöglicht. Ohne Euch wäre all das nicht möglich gewesen. Vielen Dank!